UNIVERSITY OF OKLAHOMA

GRADUATE COLLEGE

A STUDY OF SOLAR PHOTOVOLTAIC GRID INTEGRATION IN RADIAL DISTRIBUTION SYSTEMS

A THESIS

SUBMITTED TO THE GRADUATE FACULTY

in partial fulfillment of the requirements for the

Degree of

MASTER OF SCIENCE

By

DANIEL GLOVER
Norman, Oklahoma
2021

A STUDY OF SOLAR PHOTOVOLTAIC GRID INTEGRATION IN RADIAL DISTRIBUTION SYSTEMS

A THESIS APPROVED FOR THE
SCHOOL OF ELECTRICAL AND COMPUTER ENGINEERING

BY THE COMMITTEE CONSISTING OF

Dr. Paul S. Moses, Chair

Dr. Binbin Weng, Member

Dr. Jie Cai, Outside Member

Acknowledgments

I would like to thank my friends, family, professors and classmates who I have worked with as an undergraduate and a graduate at the University of Oklahoma. Namely, I would like to thank Dr. Paul Moses for his continued guidance and support in my research and lab work in the department of electrical and computer engineering at the Laboratory for Electrical Energy and Power Systems (LEEPS). I would also like to thank my fellow LEEPS graduate students, Jonathan Devadason and Wanghao Fei, who have been encouraging and resourceful in our research group endeavours. Finally, I would like to thank my mother, Sheryl Glover, for inspiring me everyday to never give up and keep my sights on the stars. *Daniel Glover*

Table of Contents

List of Figures

List of Tables

Abstract

Recent years have shown an increase in penetration of solar photovoltaic (PV) and other renewable generation onto the distribution grid. Research has demonstrated several benefits of PV integration, both for supporting peak demand and reducing power losses. However, incorrect sizing and feeder location placement of such generation in a distribution grid contributes to a plethora of problems such as: bi-directional power flow, feeder protection system coordination issues and poor voltage regulation. Traditional PV sizing single objective optimization techniques have yielded positive results on distribution feeders, yet are not adequate in larger systems, and multi-objective methods are emerging to solve for a variety of integration issues. This work discusses both the positive and negative impacts of solar PV injection in radial distribution feeders, primarily in relation to coordinated protection schemes and solar PV optimization. This work also proposes several improvements to a recently proposed *Multi-Objective Index* to allow for *multiple* solar PV to be properly implemented in a radial distribution system. A new multi-selection sizing algorithm and placement adjustment is calculated and compared to previous results based on power loss reduction and line voltage deviation correction. Additionally, further research will show the importance of exploring solar PV time series profile modeling, and continued work involving deep learning techniques for power systems analysis due to the increase in size and complexity of growing networks.

CHAPTER 1

Introduction

The twenty-first century has seen a rapid rise in the diversification of the modern power grid. Increasing energy demand worldwide has been met with various forms of distributed generation to counter the growing load and provide clean energy solutions for many areas of the globe. Despite the everlasting dependency of many populated areas on fossil fuel power supply in the twentieth century, an increasing environmental awareness on climate changes and economic factors have spurred an influx of renewable energy deployment. The negative long-term environmental impacts of fossil fuel usage for power generation have shown to reduce the health of the planet and creates cause for concern due to global warming issues, leading many countries to re-evaluate methods of power generation and distribution and turn to alternatives.

The traditional power system model has shifted or been *forced* to shift to meet these new challenges by incorporation of distributed generation (DG) on a distribution and transmission level. Due to the increase in environmental awareness from various nations and regulatory parties, including economic and political agendas, many areas have migrated towards sustainable renewable or green energy solutions for power generation. And in doing so, adequate systems integration of these various resources with existing grid infrastructure has become of upmost importance.

Older grid networks have been forced to undergo a modernization process to meet security and reliability needs, while remaining flexible for the end consumer. Other important additions to the smart grid include smart appliances, PEV's (*Plug-In Electric Vehicle*) charging stations, and robust network communication protocol. Incorporation of these elements has added levels of increased sophistication within the present day smart grid which must be more carefully examined to further understand the

consequences of such meticulous additions.

In response, power systems are rapidly expanding on both the transmission and distribution sides to accommodate wind, solar, and other forms of DG. As these systems grow in scale and complexity, proper steps must be taken to ensure correct allocation of such resources for optimal performance. Systems planning by the utility and power market analysis strategies are vital in ensuring distributed power can accommodate forecasting estimation and provide the resiliency necessary to provide supply to a growing populous with increasing energy demand.

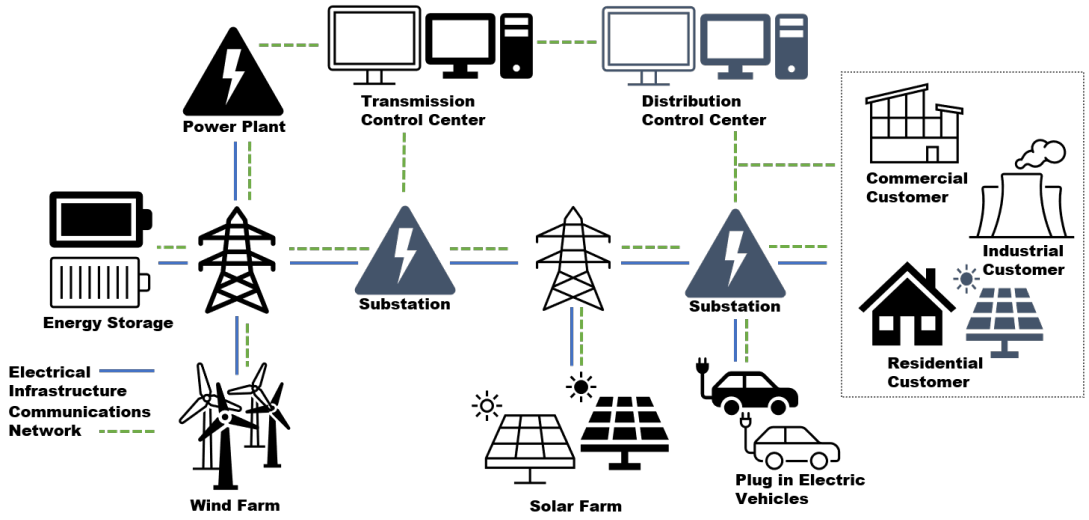

Fig. 1.1: Smart Grid Interconnection Overview

1.1 Objective

The objective of this thesis is to demonstrate the importance of proper optimization of integrated solar PV to provide benefits to the power grid. Observations of the grid behaviors and impacts of various solar penetration levels in a radial distribution feeder are tested under objective analysis. A fundamental study of various PV grid injections via iterative *power flow* computation using a recently proposed multivariate model, the *Multi-Objective Index*, will include improvements to previous studies which specifically solved for *limited* DG penetration. A mathematical model alternate is proposed to improve the optimization model during planning stages.

A series of simulations are carried out on a 6-bus radial network and a 33-bus network to validate the improved results of the adjusted mathematical model and newly proposed algorithm. In both cases, the benefits of PV implementation are highlighted, while carefully considering the negative impacts of improper solar PV sizing. The resulting experimental data will prove the effectiveness of the technique and expand on PV penetration usage in distribution feeders for power loss reduction and nodal voltage regulation improvement. A voltage deviation correction is also derived from the traditional power equations which proposes an alternative approach to solving the multi-objective approach to multi-solar DG allocation.

Additionally, this work will conduct a case study on power protection systems disruption due to solar PV integration, in which various solar penetration levels are simulated to gain a better understanding of how excessive solar PV may negatively impact network performance in a distribution system. Time graded relay systems have provided reliable protection against power systems faults and disturbances, but the introduction of PV can create problems between tripping schemes. Simulations carried out will verify this important issue on a 3-bus medium voltage radial distribution feeder.

The discussion on protection system disruption will include a description of a testbed

project build designed to replicate these protection issues in real time using practical hardware. All major components of the testbed are described from a design and test perspective in an attempt to recreate the protection relay issues caused by excessive solar PV. The physical components used will recreate a modifiable distribution feeder capable of mimicking a modern smart grid with renewable energy injections.

This work will also examine time series and solar PV pattern analysis data with variable load curves. Time-based profile analysis from variable generation and load modeling throughout a 24-hour period are simulated to show the relationship between generation and consumption in a 15-bus network. The importance of solar PV pattern forecasting for utility solar planning is described.

Finally, this work explores aspects of machine and deep learning in power systems. Power systems analysis using *Tensors* for deep learning model construction is discussed to show the possibility of dynamic power systems modeling for future research in distributed power using neural networks. Several theoretical applications for usage of tensor based analytics in power optimization are proposed along with continued research.

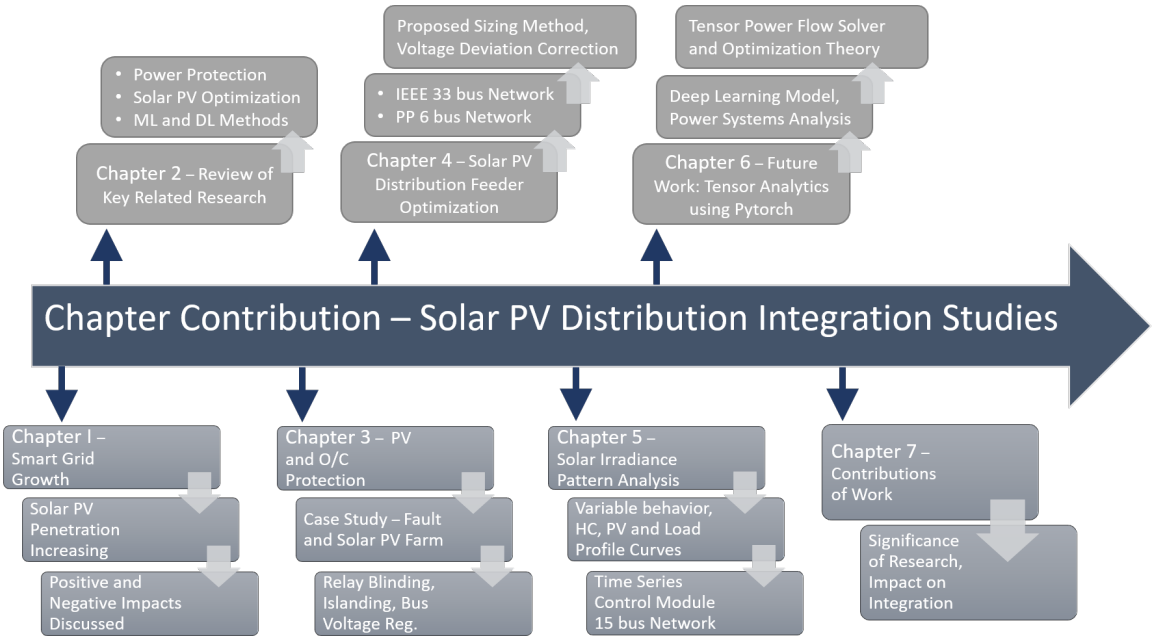

Fig. 1.2: Chapter Contribution Overview

1.2 Completed Research Papers

- D. Glover, J. Devadason, P. Moses, "Multi-Solar PV Allocation for Optimal Sizing and Placement on Distribution Feeders." *SGES 2020 International Conference on Smart Grids and Energy Systems*, Nov 2020, pp 1-6.

.

- H. Chipuio, D. Glover, P. Moses "Integration Issues of Solar PV in Distribution Feeder Protection Schemes." *2021 Photovoltaics Specialists Conference*, June 2021, pp. 1-3.

1.3 Continuing Research

Continued research in the areas of optimization of various DG in distribution systems is an ongoing effort as the dependency of clean energy rises. Grids are growing in complexity with more connected devices, smart appliances, renewable integration, etc. Therefore, simulation models used in solar PV integration planning and forecasting must move to adapt a deeper learning model to expand and accommodate multiple variables in power system calculations with dynamic capability. The adaptability of deep learning and neural network models in a variety of professional applications has proven effective. Future research using these models to make predictions and optimize system performance is becoming practical and more widely used in industry. Although there has not been much research in this area, there exists an untapped potential for artificial intelligence in power systems analysis.

CHAPTER 2

A Review of Relevant Research Studies on Distribution Level Solar PV Integration

2.1 System Fault Protection Issues

Since the beginning of the twenty-first century, power distribution systems have been evolving to adapt to the smart grid movement [1, 2, 3]. Demand side monitoring support and communication protocol advancements have created a refocus on consumer side participation in energy management. For instance, residential level smart devices are allowing individuals to use solar technology to conserve power and regain control of their power usage [4].

At the end of 2018, global solar PV installations exceeded 500 GW, an increase of nearly 400 GW from 2017, at 102 GW. The US and global PV consuming capacity is also expected to double by 2022 [5]. However, increasing levels of distributed energy resources (DERs) at the local distribution level are becoming problematic for traditional power protection systems. Many of these systems have been in place for long periods of time, making adjustments only as required with minimal cost. Larger numbers of solar photovoltaic (PV) systems are being deployed, creating complexities such as poor relay coordination, unintentional islanding, and bi-directional power flow within the traditional power protection system framework.

Modern electrical networks are still functioning with traditional relay based protection schemes to defend against faults and overload to the system [6]. Synchronous generators used to supply power contribute highly to fault current levels in distribution feeders, which are typically cleared using overcurrent (O/C) relays. However, heavy penetration of solar PV can alter voltage and current levels as seen by these protective

devices, creating weak fault current conditions and lowered line impedances during fault events [7].

In areas where a high capacity of PV exists, relay coordination faces extreme challenges. [8] conducts a study in which several time graded O/C relays are tested on the IEEE 9-bus system under fault conditions with locally injected PV. In several cases, the relays fail to clear the fault (or experience interruption) due to varying fault current levels - a condition referred to as *blinding*. Various fault current limiters (FCLs) are tested along with several directional schemes, however, the dynamic power injection profile of PV creates additional problems that cannot be overcome. A similar experiment from [9] confirms the severity of these results using degraded PV modules over long periods of time.

Grid-tied *islanding* conditions can occur when a portion of the network containing DERs is detached due to an open breaker or recloser opening, and continues injecting power in the isolated segment [10]. Upon re-connection with the grid, an immediate frequency match is required from this separated circuit, which is typically handled by the grid-tied inverter control. However, many systems do not posses this capability and a frequency mismatch upon joining can create issues for utility personnel on the ground dealing with live wires [11].

Anti-islanding controls using sequential relay pairs with digital logic microcontrollers have been proposed on the relay side to control multiple sets of breakers to divert fault currents and prevent specific sections containing DG from becoming separated. Varying fault location determination allowing protection systems to act quickly to avoid creating islanding scenarios in smart grids is also considered [12]. Connections at the point of common coupling (PCC) must also be considered to improve the distribution protection through active inverter side voltage regulation control [13].

Research shows inverter side DG control is effective during fault response and power control dominated networks can show overall improved protection on the PV side. PV

generators behave differently compared to synchronous and asynchronous generators [14]. As previously discussed, the PV can be disconnected during a fault at the PCC at matching grid frequency. However, this can be avoided through low voltage ride through (LVRT) and high voltage ride through (HVRT), enabling terminal voltage regulation capacity at certain voltages during specific time intervals [15]. Various LVRT and HVRT curve models enable generators to remain connected to the grid during disturbances, such as faults and power outages, reducing power losses [16]. Presently, the concept of voltage ride through is still being debated amongst professionals. The IEEE 1547 standard for DER interconnection underwent a revision in 2018 to address high penetration of PV systems, islanding, and LVRT/HVRT. Ultimately, the system should have the strength to recover on its own from these events using traditional protection schemes, but DERs create the need for additional grid monitoring and control on the inverter side.

2.2 Hosting Capacity Constraints

Major factors such as market demand, cost, energy conservation and thermal heating, power loss compensation and energy storage have created the need for improved methods of PV integration planning [17, 18, 19]. In order to meet the required nodal hosting capacity of the distribution feeder, optimization of these factors is critical in the integration process. Since 2005 when the US Congress passed the investment tax credit, the number of annually installed residential PV systems has grown by nearly 35% per year. According to the National Renewable Energy Laboratory, by the end of 2018, the number of operational residential PV systems in the US had surpassed 2 million units and is expected to continue increasing exponentially over the next decade [5].

To achieve a desired optimum PV system configuration, several optimization algorithms have been tested and implemented such as particle swarm (PSO) [20, 21, 22]

and genetic algorithms (GA) [19]. These techniques allow for not only single objective, but bi-objective and even multi-objective optimization analysis to minimize and/or maximize objective functions vital to successful PV integration in distribution systems such as hosting capacities, location of the DG, sizing solution sets, etc [23]. Other economical factors and environmental impacts from locally installed DER systems are also taken into consideration for proper planning purposes. Traditional optimization methods have operated on a single candidate solution, whereas GAs and other multi-objective functions provide a unique solution space dictated by dominance. Each objective met through optimization is held under a particular constraint or limit given for satisfying a particular condition within the solution set.

Evaluation of the grid Hosting Capacity (HC) is crucial in determining how a certain section of the network will respond to solar PV power injection(s). The fundamental methodology behind calculating the HC in low voltage and medium voltage networks is discussed thoroughly in [24, 25, 26]. A common practice of most major distribution utilities is the determination of network and nodal HCs defined as the maximum solar PV generation that can be integrated in the distribution system without causing any adverse effects (feeder congestion, voltage profile constraints, power quality,etc.) to normal system operation [27].

A study performed in [28] uses the GA with a Newton-Raphson power flow method to determine the maximum PV hosting capacity in a local distribution network. The proposed model measures PV penetration permeability based on current and voltage limits versus the local load due to excessive PV levels to determine PV output power thresholds (overloading condition constraints are included). A stochastic approach to solving the multiple objective PV optimization HC problem is used in [29] to create various PV size and location solution set scenarios. A load flow analysis is iteratively performed on the IEEE 123-bus system to determine the maximum PV output power allowed for each customer location using the steady state overvoltage threshold as

defined in the ANSI C84.1-2011 standard as 1.05 p.u.

Another method of satisfying multiple objectives using integrated solar PV is known as the multi-objective index (IMO), proposed in [30]. This GA also uses multiple derivative-based index ratios to quantify the size of each solar PV at every bus in a distribution network based on active and reactive power losses. Reference [31] conducts an extended study using multiple time domain profiles for both demand and PV irradiance levels. Although this method is proven effective, it is primarily designed to determine a singular optimal solar PV size only. In larger distribution networks where multiple DER installations may be considered, the IMO does not adequately perform without modification.

Additional optimization methods for DG include complex power matching from [32] using inverter-based control to regulate active and reactive power injection on the DC/AC converter side. In this regard, optimal steady-state power injection from inverters is proven to benefit the utilities and offset overload in high demand situations. In a distribution system, depending on the time of day and weather forecast, PV inverters are capable of delivering maximum active power using Maximum Power-Point Tracking (MPPT).

However, the optimal complex power problem requires the total power generation capacity to be shared between active and reactive powers using inverter pulse width modulation [33]. This process involves creating a phase shift on the AC side between voltage and current waveforms so that reactive power may be injected or absorbed by the inverter [34]. Hence, for a power factor of one, no reactive power is absorbed or generated, and visa versa, allowing the optimum complex power of each PV to be injected during each cycle such that the overall system demand as viewed from the substation is minimized. Of course, current limitations on the inverter side switches will dictate the amount of acceptable active power converted by the inverter and so an equalization process is proposed to offset higher currents while maintaining maximum

apparent power at the inverter side.

2.3 Machine Learning based Practices

New developments in modern day smart grids due to expanding DER distribution and smart devices are paving the way for new and improved analysis techniques in power systems. The growing amount of data collected from high quality sensors, phasor measurement units (PMUs), and smart meters are essential for smart grid analysis and operational control [35]. Research in power system data analytics suggests that conventional time domain approaches are computationally inefficient and may not meet the requirements of real-time applications [36].

The green energy transition towards integration of DERs, which deliver intermittent and variable patterns of generation such as solar PV and wind, add a new dimension to traditional power flow equations [37]. The addition of these local generators in distribution feeders require improved analysis methods to provide efficient, reliable, and economical solutions to multivariate system parameters. In this regard, it is feasible to estimate that machine learning (ML) based methods in power systems analysis could potentially produce very useful knowledge and even discover hidden patterns or meaningful trends which may have otherwise gone unnoticed.

Fundamental learning by the model in ML based training involves a test/train data set in a supervised or unsupervised environment. Classification and regression models are the most commonly used where target data or numerical predictions are desired. In power systems analysis, network stability assessments and fault/outage prediction fit a unique classification problem in [38]. Similarly, grid restoration, forecasting and optimization of DERs for planning may take a more regressive modeling approach.

Recent efforts using Support Vector Machine (SVM) in [39] to assist utilities in determining power outages proved successful. SVM involves a discriminative classifier

model which learns linear and non-linear decision boundaries in the attribute space to distinguish classes [40]. The hyperplane boundary (and attributes) can also be transformed into a different dimensional space to improve accuracy using various kernal functions. [41] also used SVM to detect single-phase line-to-line faults in distribution systems with high accuracy, although alternative models such as K-Nearest Neighbor (KNN) and a Decision Tree (DT) proved even more efficient as more fault system behavior data was considered.

Unlike ML models, Deep Learning models have made breakthroughs in a variety of applications due to learning representations and feature extraction [38]. Optimization of solar PV in distribution feeders involves estimation of time-varying load and solar models to determine sizing based on power and energy losses. Typical quasi-static time series models are computationally slow at solving optimization simulations involving PV for long-term simulations, and so faster methods are required to analyze energy loss data with integrated PV's in a multi-bus distribution system each day [42].

Recursive Neural Networks (RNN) and Artificial Neural Networks (ANN) are used in generating mapped predictive models for power systems. Relationships between unknown parameters may be discovered in training these models, allowing for quick response to dynamic conditions. In [43] a long-short term memory LSTM-RNN is used to train forecasting models to provide accurate irradiance predictions for hour-ahead solar PV power. [44] uses and ANN for solar PV contingency analysis in a 110 kV grid with accurate line loading predictions to place DG in critical weak bus locations. Short term prediction modeling using DL methods has shown promise regarding weather forecasting, demand, power loss, and DER power output. These models provide a quick, efficient means of making data-based decisions when dealing with time-varying elemental grid behavior.

DL models also use the fundamental relationship of mathematical derivatives to ascertain relationships between various factors in a large set of data. These relationships

are fundamental to global minimization of the loss function involved in optimizing parameters related to solar PV integration. A relatively new technique developed by [45] and [46] describe analysis of three phase power flow and maximum loadability using *Tensors*, multi-dimensional arrays used in data representation for ML and DL based learning. Tensors allow for extremely fast and convenient learning through *backpropagation*, a process of taking derivatives of the weighted model parameters with respect to the output of the model to determine the gradient of a loss or cost function.

However robust these models may be, they all do possess vulnerabilities to data attacks and cybersecurity breaches, even at the substation level. It is shown in [47] that attackers do not require access to the ML model itself, but rely only on data manipulation for brief instances of time to inject misinformation into the system on a power quality disturbances classifier. Using algorithms from [48], an RNN-based building load forecasting model is perturbed with falsely set temperature setpoints to detour the model's prediction accuracy.

The majority of these models are also simulation based and have not been practically tested using physical components in a testbed or realistic setting. Real world costs for implementation of these models is quite an investment in the migration towards artificially controlled power systems, a stern commitment on the part of the utility. For this reason, there exists room for improvement in model development for future adaptation to the evolving smart grid.

CHAPTER 3

An Analysis of Power System Protection Issues and Solar PV Integration

3.1 Solar PV and Overcurrent Protection

3.1.1 Introduction to PV Injection and Protection Systems

Power distribution systems over the past decade have been undergoing a transformation ever since the smart grid movement ignited over a decade ago [1, 2, 3, 6]. The increasing amount of renewable energy in transmission and distribution grids, particularly from volatile solar photovoltaic (PV) systems and wind farms, is another dimension in the reliability problem. Following the events of the 2003 North-East America blackout, the smart grid initiative has led to large investments by governments worldwide to improve resiliency considering multiple contingency failure modes, beyond the conventional N-1 reliability constraint.

From a protection system point of view, PV systems in some ways are more of a concern than other forms of distributed generation (DG). Aside from variable output behavior, wind farms tend to be concentrated in selected locations and at well-studied points of interconnection (POI) to a stiff transmission system backbone network. On the contrary, PVs, particularly in distribution grids, can appear at many different POIs and in low-stiffness networks that are more vulnerable to power quality disturbances and faults. As a consequence, utilities are wary and very conservative of limiting PV capacities at the distribution system level.

The increasing number of solar photovoltaic (PV) systems in distribution networks has presented new challenges to protection devices. Complications in coordination

between relays designed to detect faults arise from bidirectional power flow due to excessive PV penetration at the distribution level. This chapter highlights some of the more concerning operational scenarios of PV systems and their impacts on typical time-current overcurrent (O/C) grading Type 51 relays. The Inverse definite minimum time (IDMT) O/C relays operate by monitoring the load current via connection to a local current transformer (CT). Calibrated pickup settings determine the threshold at which the relay sends a control pulse to the respective breaker to open the circuit. If the load current exceeds the pickup setting, the relay will trip and clear the fault.

This chapter focuses on fundamental protection system principles at the distribution feeder level and includes a set of case studies carried out via the electromagnetic transient program (EMTP-RV) software considering DG from a solar PV Farm. First, a brief summary of common distribution feeder protection system challenges involving the integration of DG's is discussed. Next, a number of simulation case studies are carried out for a small radial-type distribution network considering a single solar PV Farm yielding various PV irradiance percentages at different sites. A single phase line-to-ground fault is also introduced to the network to observe the disturbance behavior of the system simultaneously with the PV. The test network and case studies are evaluated using EMTP-RV and the data is presented for each case. Finally, the impacts on overall protection coordination due to high solar PV penetration are discussed.

A typical distribution feeder has most of its primary protective devices installed at the substation, the demarcation point between (sub)transmission and distribution levels. Differential protection for transformers and bus zones exists within the substation, but are not the focus of this work. A typical distribution substation layout is shown in Fig. 3.1. Downstream of the substation there may only be reclosers, line sectionalizers and fuses installed on branch laterals.

If there is a solar PV farm connected to the feeder, some additional protection functions are offered by the inverter controls for fault current limiting, anti-islanding and

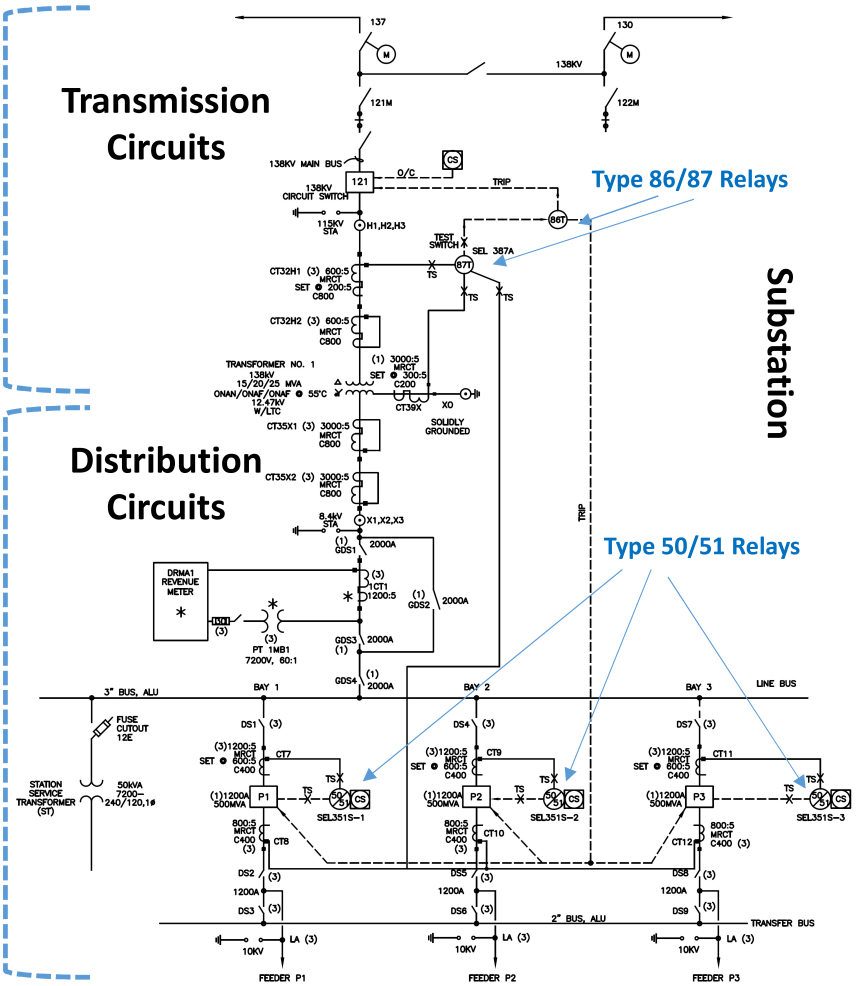

Fig. 3.1: Typical distribution substation with common protection devices

momentary cessation. There may also be additional relaying points, circuit breakers and fuses at these sites. While there are recommended standards for inverter controls and protection such as IEEE 1547, they are not uniformly adopted by inverter manufacturers and present significant challenges in future systems. A major issue that is under intense focus is grandfathering legacy and present types of inverter systems which employ different control architectures that cannot be easily updated, and are complying to different standards over the past few decades. This further complicates interoperability with primary distribution protection schemes which are still rooted in century old practices.

To simplify protection coordination issues with PV farms, many utilities employ a

direct transfer-trip scheme which is used to signal the PV farm(s) to cease operation for any feeder fault [49]. To avoid the islanding dangers of DGs energizing a faulted section, transfer tripping requires the DGs to disconnect after a short delay (e.g., within two seconds after islanding occurs) when the substation feeder breaker is tripped. This is the most conservative and secure approach when it comes to protecting a feeder with DGs as it clears the system of all possible supply points that may be feeding the fault. However, it trades off selectivity of isolating the fault and leads to blacking out the entire feeder. If reclosers are used, coordination suffers due to the possibility of reclosing a DG fed island onto an out-of-phase situation [50]. Active power imbalance will result in small changes in frequency of an *islanded* (isolated from the grid) DG system and may cause the reconnection of asynchronously operating systems, resulting in transients that could damage vital utility and customer equipment and lead to further protection tripping [51].

The other approach is to largely remain with the traditional protection time-grading coordination and make changes on the fly when new DGs such as PVs are installed. Some utilities which may currently be experiencing lower volume of integrated PVs are trying to not make extensive protection relay setting changes in order to maintain traditional protection relay selectivity. The argument is that if the penetration level is low, then setting up the protection system in the traditional time-current grading fashion may still work. But the question remains, to what degree? This chapter examines this latter scenario and examines how excessive PV penetration may impact traditional time-current relay grading of radial distribution feeders.

3.2 EMTP Distribution Feeder Test System

The transient simulation software used for this investigation is EMTPWorks v4.1 2020. The system used for this study is a three-bus radial distribution system composed of a 12.47 kV substation supply, and four consolidated load centers with a peak load of

7.2 MW and 1.35 MVAR. From Fig. 3.2, two protection overcurrent relays located between buses two and three are used to mimic a time graded protection scheme on the feeder. Meters are placed at each bus location for power flow monitoring during simulation.

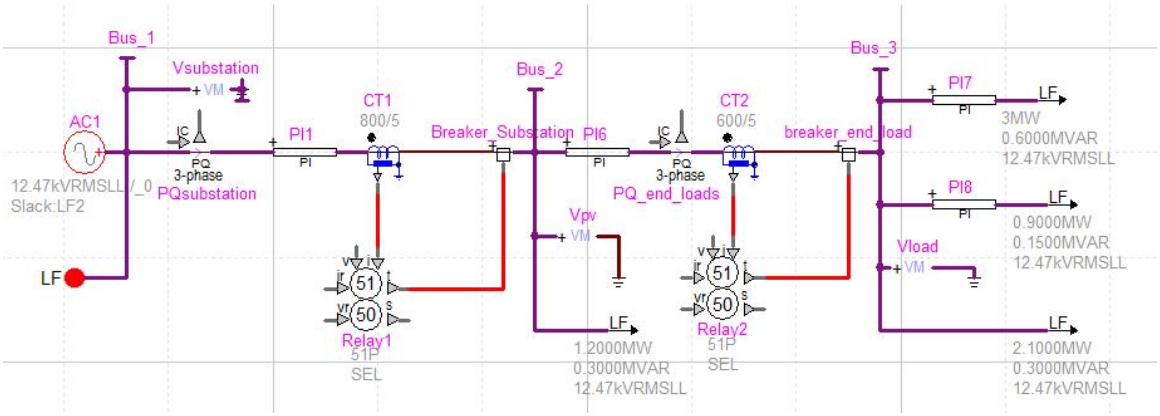

Fig. 3.2: EMTP test distribution system without the solar PV farm

3.2.1 Simulation of Protection Relays

EMTP includes a full library for several digital protection relay manufacturers that accurately mimics their signal processing functions and tripping logic as well as current transformer behavior. In this study, the Schweitzer Engineering Laboratory (SEL) model SEL 351S relays using Type 51 IDMT overcurrent settings were selected to provide time graded protection on the feeder at two relaying points as shown in Fig. 3.2. Additionally, two circuit breakers are connected to each respective relay alongside two appropriately specified current transformers (CTs).

The relays are calibrated using the *IEEE Moderately Inverse* curve type. The relay pair is setup to achieve typical time-current grading for a radial feeder where relay 1 provides back up protection for relay 2 in the event of a failure. It is important to note that typical digital protection relays only operate on the fundamental frequency phasor rms quantities for currents. This behavior is replicated in the EMTP relay

model where the signal processing chain shows that the harmonics are filtered out and a moving window of one power cycle is used for rms computation for the IDMT curve trip time calculation.

Current transformers are selected from the IEEE C57.13 specification and set accordingly based on the following calculations for a time graded protection scheme. From the IEEE C37.112-1996 specifications for *IEEE Moderately Inverse* curve type, the time of operation for a relay to energize T_{op} is given as follows with A = 0.0515, B = 0.114 and C = 0.02.

$$T_{op} = TMS \left[\frac{A}{PSM^C - 1} + B \right] \tag{3.1}$$

From equation 3.1, T_{op} is the relay operational time taken to energize and send a control signal to the connected breaker to open the circuit due to high line currents. The Plug Setting Multiplier (PSM) is a ratio of the connected current transformer secondary current versus the pickup current. The Time Dial or Time Multiplier Settings (TMS) acts as an incremental time dial for energizing the relay as these are not instantaneous devices. The values of constants A, B, and C are determined by the type of inverse curve. Initially, the system is set to accommodate peak load conditions and tested using a fault placed at buses 2 and 3 to verify backup protection by Relay 1 for Relay 2 in case of a failure to operate during a fault. Calculations are shown below.

At peak load, calibration begins with a CT ratio of 500:5 for Relay 2 with $I_L = 1.085$ p.u. yielding a primary side current of $542.4A_{RMS}$. The CT ratio is raised to 600:5 to allow for the pick-up settings to remain lower based on future load growth estimation. Next, a single-phase line-to-ground fault is initiated to observe the increased current levels. Relay 2, which sits at the end of the radial feeder, is not backing up any other relay in this network, so the TMS is set to its lowest value of 0.1. This produces a line current of $10.4A_{RMS}$ on the secondary side of the CT. Therefore, the time of operation

for this relay is determined as follows.

$$T_{op} = 0.1\left[\frac{0.0515}{PSM^{0.02}-1} + 0.114\right]$$

$$PSM = \frac{1252.2 * (5/600)}{1.2 * 5} = 1.739$$

$$T_{op} = 0.474sec$$

Relay 1 must now be calibrated to trip for a fault in the bus 3 zone if Relay 2 fails to engage. It must also be set to trip for any fault in bus 2 which Relay 2 will not see. A CT of size 800:5 is selected for Relay 1. Assume a 300 msec time delay addition for all relay back-ups. The desired time of operation is considered initially in the calculation.

$$PSM = \frac{1252.2 * 5/800}{1 * 5} = 1.565$$

Assuming a TMS of 1,

$$T_{op} = \left[\frac{0.0515}{1.565^{0.02}-1} + 0.114\right] = 5.838$$

This is much too slow to clear faults before serious damage occurs, but is only an estimation based on a higher TMS and does require some delay to give Relay 2 time to act. The time delay is added to the Relay 1 trip time to determine the correct TMS settings (values are always rounded up to the nearest tenth of a second). The final TMS value is determined to be 0.2. After setting the pick-ups, the same fault is re-positioned at bus 2 to determine the new time of operation for Relay 1. Repeating the same process for calibration, the primary CT side fault current is calculated to be $1.98kA_{RMS}$.

$$I_F = 2.4695p.u * 800 = 1975.6A_{RMS}$$

$$PSM = \frac{1975.6 * (5/800)}{1.2 * 5} = 2.058$$

$$T_{op} = 0.2 \left[\frac{0.0515}{2.058^{0.02} - 1} + 0.114 \right] = 0.731 sec$$

Thus, Relay 2 was set to trip 0.474 seconds after sensing a fault located at bus 3 and Relay 1 was set to trip 0.731 seconds after a fault is engaged in the system at bus 2. Again, Relay 1 was also calibrated to back up Relay 2 in the event that Relay 2 fails to clear the fault using time grading techniques with an added 300 msec delay to prevent accidental overlap between relays. Both relay IDMT curves in Fig. 3.3 and settings are shown below with typical test system line impedance values.

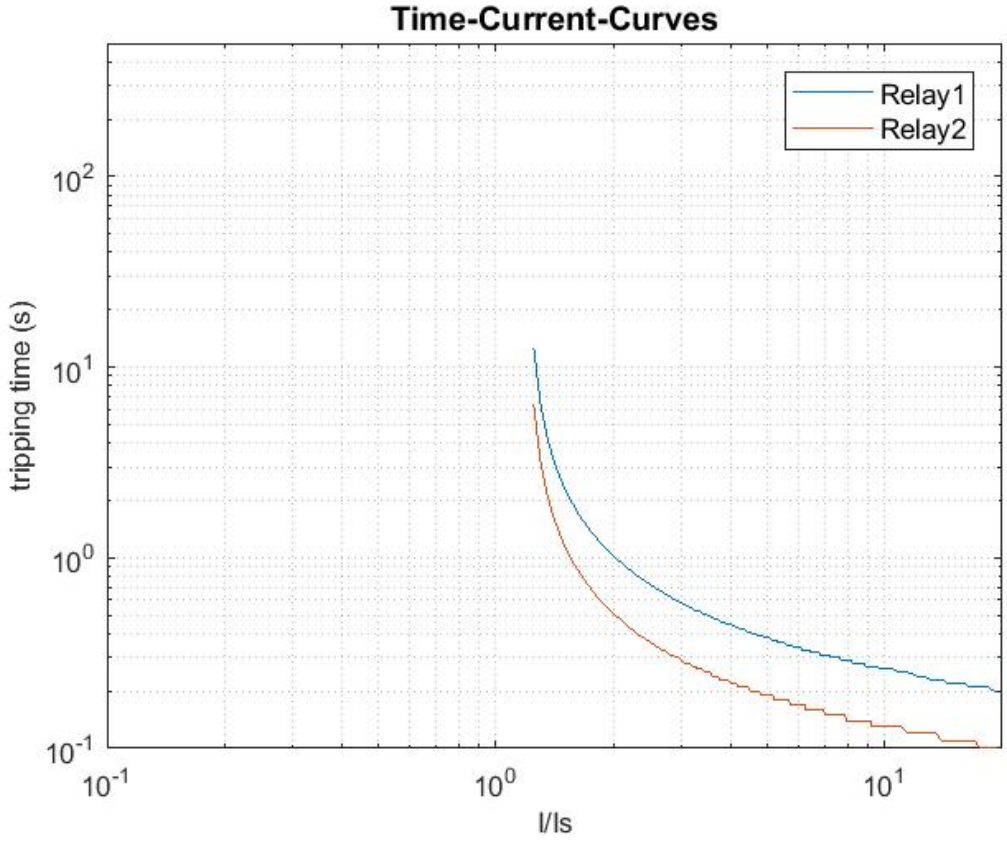

Fig. 3.3: IDMT Curves for Protection relays

Table 3.1: Protection Relay Settings for Relay 1 and 2

Settings	Relay 1	Relay 2
$I_{Pkp}(p.u.)$	1.2	1.2
Time Dial	0.2	0.1
CT ratio	800/5	600/5
CT burden		
Z burden (ohms)	2.0	2.0
Power Factor	0.5	0.5

Table 3.2: Line Impedance

Distribution Cable Impedance	
R (ohms)	1.0
L (mH)	1.0
C (μF)	0

3.2.2 Dynamic Modeling of Solar PV Farm

This version of EMTP includes various models for simulating solar PV farms. Each PV park model consists of a solar panel, PV array transformer (LV/MV), equivalent PI circuit of the collector grid and a PV park transformer (MV/HV). Settings for each model allow the user to modify general park parameters. This includes the number of PV arrays in the park versus the number in service, grid voltage and frequency matching, reactive power injection from the dc/ac inverter model at the POI, and solar irradiance levels.

An average-value-model (AVM) is implemented for simulating the grid-tied inverter on each PV park. The pulse-width-modulation (PWM) switching transitions of the inverter which mimic the ac-dc-ac two-level converter are not captured through the AVM, however, the dynamics of the output terminal filtered characteristics are captured as the duty ratio of the switches is dynamically changed. By using the AVM, the intensive mathematical operations and high frequency PWM signals which force small time step usage in simulations, can be avoided with accurate approximations. In other words, the important dynamics at the inverter terminals through PWM duty cycle variations by the control strategy, and its coupling into grid faults, will still be

retained. It is only the high frequency switching components that are neglected, which would not have any bearing on the protection relays anyway since those frequencies are filtered out in practice.

The maximum power point tracking is also considered in the control strategy and the PV source is modeled as a controlled current source. In this way, the active power injection and effective penetration level can be easily adjusted. For this study, the internal protection system of the inverter controls was intentionally bypassed in order to focus exclusively on the upstream feeder protection actions. This may be prescient since the community is debating the ride-through requirements and momentary cessation behaviors of inverters, which vary over different inverter implementations over the years.

3.3 Case Study Test Results and Analysis

In this section, a series of simulations are carried out to analyze the effects of injected PV in the distribution system. Four different cases were simulated considering different values of PV output power as well as fault and PV locations. The results show the values for voltage, peak waveform current and real power at the substation, PV park and end feeder loads labelled in Fig. 3.2 as buses 1, 2 and 3, respectively. Additional results from each case study verify relay tripping action in the respective zone based on PV an fault placement.

All simulations were performed with a solver time step of $10\mu s$ within a $1.5s$ window for each simulation run. EMTP permits the time-domain simulation to be initialized from a starting load flow snap shot, however, approximately $0.4s$ was required for the simulation to reach a steady state condition. This is most likely due to the PV inverter internal controllers' initial stabilization period on the grid-connected side.

3.3.1 Case 1: Baseline No Fault Scenario

For this case, the PV farm was connected at bus 2 of the network. To establish a baseline case for comparison, simulations in Case 1 were conducted without imposing a fault in the system. Only increasing levels of PV penetration are considered. The results are shown in Tables 3.3 - 3.5.

Table 3.3: Case 1: Substation, Slack Bus Results

PV (MW)	Voltages (p.u.)	Peak current(A)	Power (MW)
1.667	1.000	346	4.99
6.668	1.000	110	0.3
10.002	1.000	269	-2.8
13.336	1.000	422	-5.9
16.67	1.000	445	-6.2
23.338	1.000	1029	-15.5
26.672	1.000	1235	-18.7
30.006	1.000	1439	-21.1

Table 3.4: Case 1: PV Park, Bus 2 Results

PV (MW)	Voltages (p.u.)	Peak current (A)	Power (MW)
1.667	0.997	110	1.6
6.668	0.998	444	6.68
10.002	1.020	666	10.2
13.336	1.033	887	13.4
16.67	1.034	887.6	13.9
23.338	1.101	1533	25.7
26.672	1.113	1733	29.7
30.006	1.138	1959	34

Table 3.5: Case 1: Load Bank, Bus 3 Results

PV (MW)	Voltage (p.u.)	Peak current A	Power (MW)
1.667	0.961	365	5.09
6.668	0.959	377	5.44
10.002	0.976	386	5.7
13.336	0.993	393	5.85
16.67	1.001	393.8	5.94
23.338	1.058	412	6.61
26.672	1.070	419	6.85
30.006	1.090	424.6	7.08

The results of the base case simulation show that as the PV penetration level increases, both the voltage and current in the circuit increases from the added solar power injection. Initially from the perspective of the substation, the current is reduced since the PV is contributing more local injected power at bus 2. However, once the amount of PV output exceeds approximately 7 MW of injection, a potentially problematic condition of reverse power flow is observed at the substation. This phenomena can be seen in Table 3.3 as negative power magnitude which indicates a directional change in current, and coincides with similar studies from [52] in which the net injected power from the PV farm creates a nodal capacity breach. Additionally, as the PV penetration is increased, local bus voltages also increase to the point of excessive violation of the typical $1 \pm 5\%$ p.u. The following three case studies introduce a single feeder fault to the network, to focus on the protection relay behavior and how it changes as the PV penetration levels are increased.

3.3.2 Case 2: Single Phase Fault and PV Farm at Bus 2

For the second case study, a line-to-ground fault was introduced to the system at bus 2, while the PV park remains active at bus 2. The fault is set to engage in the system at 0.5 seconds. Fig. 3.4 shows the image of the test circuit for this case, followed by simulation results below.

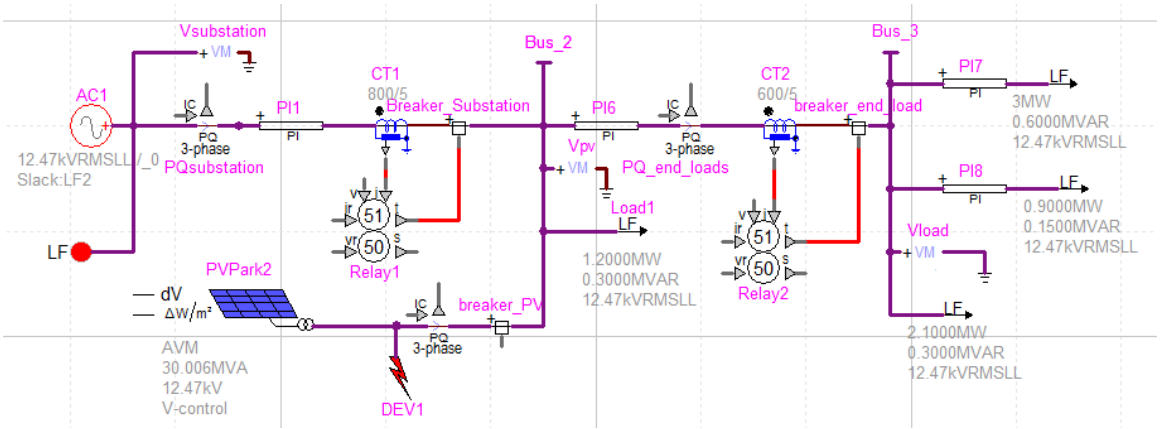

Fig. 3.4: EMTP distribution system with the fault and the PV connected at bus 2

Table 3.6: Case 2: Substation, Slack Bus Results

PV (MW)	Voltage (p.u.)		Peak current (A)	
	Pre-fault	L-G fault	Pre-fault	fault
1.667	1.000	1.000	334	3481
6.668	1.000	1.000	153	3264
10.002	1.000	1.000	197	3116
13.336	1.000	1.000	406	2974
16.67	1.000	1.000	614	2830
23.338	1.000	1.000	942	2566
26.672	1.000	1.000	1170	2447
30.006	1.000	1.000	1364	2336

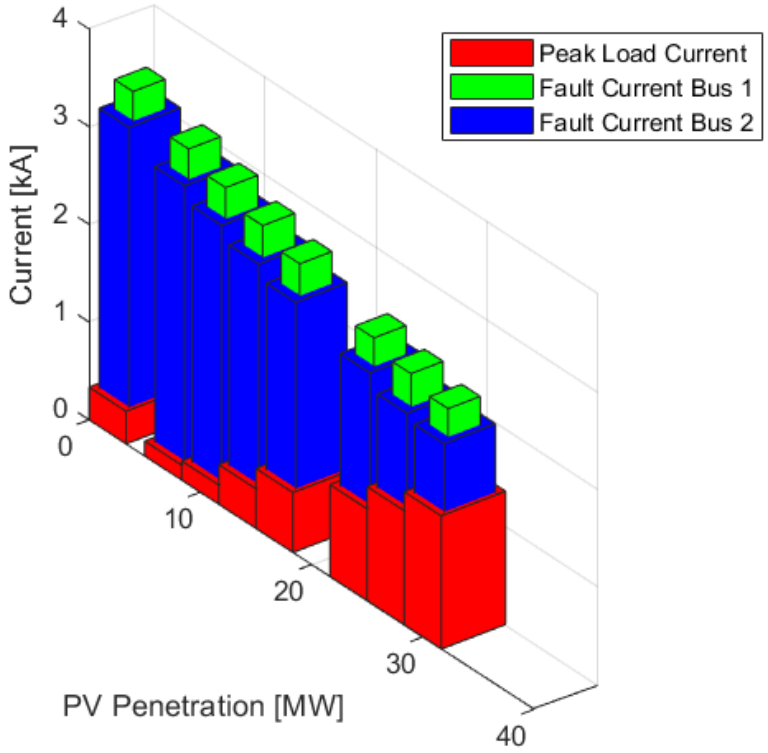

Fig. 3.5: Case 2 Fault Current Comparison Bus 1 and Bus 2

In Fig. 3.4, it can be seen that the PV and the fault are connected at bus 2 between Relays 1 and 2. Since the fault and sources are upstream of Relay 2, it is expected only Relay 1 will see the fault. From Fig. 3.5, the fault current seen by the relays at the substation and bus 2 decreases when PV output is at its highest. Table 3.6 confirms that the fault current fed from the PV farm is lowered as the solar PV penetration

Table 3.7: Case 2: Relay Tripping Time

Penetration levels (MW)	Tripping time (s)	
	Relay 1	Relay 2
1.667	0.507	no trip
6.668	0.619	no trip
10.002	0.65	no trip
13.336	0.69	no trip
16.67	0.73	no trip
23.338	0.84	no trip
26.672	0.92	no trip
30.006	no trip	no trip

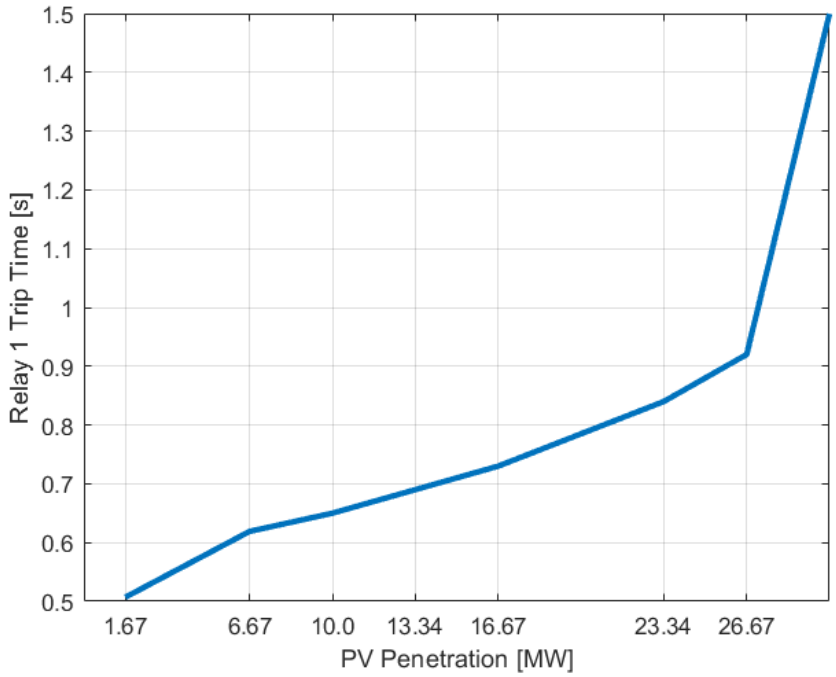

Fig. 3.6: Case 2: PV Farm and Fault at bus 2

increases.

It is observed in Table 3.7 that the tripping time of Relay 1 increases as more PV is injected into the network. When the penetration level reaches a maximum level of 30.006 MW, the relay fails to trip during the simulation. Therefore, as the solar penetration level increases, there is a higher likelihood of the occurrence of a blinded relay scenario in which the relay fails to send a control pulse to its respective circuit breaker, thereby damaging the system by not clearing the fault. Fig. 3.6 shows the

PV penetration versus Relay 1 trip time in which the curve becomes steeper as the PV penetration is increased. This is a direct consequence of the PV reaching high penetration percentages that offset the fault current to operate near the asymptotic part of the relay's IDMT curve.

3.3.3 Case 3: Single Phase Fault at Bus 3 and PV Farm at Bus 2

For the third case, the PV remained at bus 2 and the fault was relocated to bus 3. In this scenario, it is expected to observe Relay 2 trip due to a repositioned fault location (with Relay 1 not tripping, unless Relay 2 fails to energize). Results are shown below in Tables 3.8 - 3.11.

Table 3.8: Case 3: Slack Bus Results

PV (MW)	Voltage p.u		Peak current (A)	
	Pre-fault	L-G fault	Pre-fault	fault
1.667	1.000	1.000	336.87	2042
6.668	1.000	1.000	84.8	1793
10.002	1.000	1.000	196.8	1635
13.336	1.000	1.000	407	1468
16.67	1.000	1.000	617	1339
23.338	1.000	1.000	1035	1127
26.672	1.000	1.000	1252	1154
30.006	1.000	1.000	1444	1108

Table 3.9: Case 3: Bus 2 Results

PV (MW)	Voltage p.u		Peak current (A)	
	Pre-fault	L-G fault	Pre-fault	fault
1.667	0.965	0.788	111	110
6.668	0.998	0.813	444	441
10.002	1.020	0.830	666	661
13.336	1.042	0.851	887	884
16.67	1.061	0.864	1104	1106
23.338	1.100	0.891	1528	1585
26.672	1.121	0.901	1737	1757
30.006	1.137	0.914	1963	1867

Table 3.10: Case 3: Bus 3 Results

PV (MW)	Voltage p.u		Peak current (A)	
	Pre-fault	L-G fault	Pre-fault	fault
1.667	0.928	0.573	366	2088
6.668	0.959	0.591	378	2155
10.002	0.980	0.603	385	2200
13.336	1.002	0.616	394	2248
16.67	1.021	0.628	400	2294
23.338	1.057	0.644	408	2364
26.672	1.077	0.655	415	2393
30.006	1.094	0.665	419	2403

Table 3.11: Case 3: Relay Tripping Time

Tripping time (s)		
Penetration levels (MW)	Relay 1	Relay 2
1.667	no trip	0.3788
6.668	no trip	0.366
10.002	no trip	0.356
13.336	no trip	0.3475
16.67	no trip	0.339
23.338	no trip	0.326
26.672	no trip	0.321
30.006	no trip	0.313

From Table 3.8, it is observed that the pre-fault current measured from the slack bus eventually becomes greater in magnitude than the fault current due to excessive PV in the system. It should also be noted that the introduction of the fault in this case has lowered the bus voltage at bus 3 to an unacceptable operational level. This is because of the relationship between voltage and current in Ohm's Law in which a sudden rise in current will lower the immediate nodal voltage. In Table 3.11, the tripping times for Relay 2 decrease as the penetration level increases. This observation occurs partially because higher PV injection, notably located between the generation point and fault point, leads to a higher fault current at the end loads location, thus, Relay 2 is faster to react. Fig. 3.7 shows a linear and inverse relationship between PV penetration and Relay 2 trip time for this case, with no blinding conditions observed.

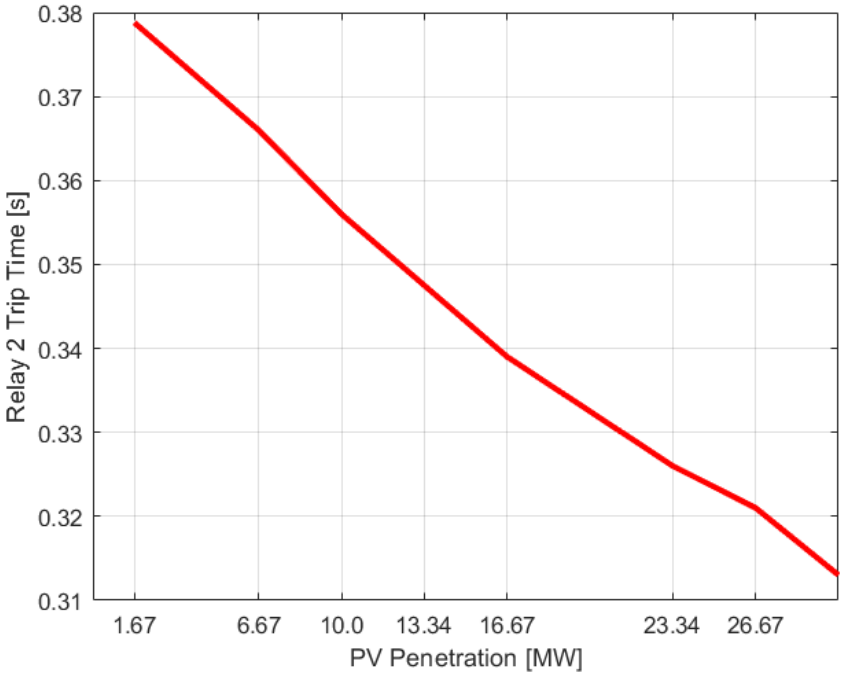

Fig. 3.7: Case 3: Relay 2 Tripping Time

3.3.4 Case 4: Single Phase Fault and PV Farm at Bus 3

In this section, the PV farm and fault were connected at bus 3. It is expected that results from this case should mimic the results from case 2, in which the PV and fault locations lie on the same bus.

Table 3.12: Case 4: Slack Bus Results

PV (MW)	Voltage p.u		Peak current (A)	
	Pre-fault	L-G fault	Pre-fault	fault
1.667	1.000	1.000	353	2091
6.668	1.000	1.000	196	1965
10.002	1.000	1.000	204	1876
13.336	1.000	1.000	403.6	1784
16.67	1.000	1.000	603	1700
23.338	1.000	1.000	1027	1609
26.672	1.000	1.000	1246	1582
30.006	1.000	1.000	1452	1631

Table 3.13: Case 4: Bus 2 Results

PV (MW)	Voltage p.u		Peak current (A)	
	Pre-fault	L-G fault	Pre-fault	fault
1.667	0.965	0.783	200	77
6.668	0.996	0.797	204	84.9
10.002	1.014	0.807	212	90.7
13.336	1.031	0.816	221	95.93
16.67	1.043	0.824	231	102
23.338	1.047	0.840	247	113
26.672	1.052	0.841	251	113
30.006	1.094	0.847	254	120

Table 3.14: Case 4: Bus 3 Results

PV (MW)	Voltage p.u		Peak current (A)	
	Pre-fault	L-G fault	Pre-fault	fault
1.667	0.938	0.575	263	2027
6.668	1.000	0.603	116.8	1901
10.002	1.029	0.622	251.7	1806
13.336	1.056	0.641	440	1715
16.67	1.105	0.656	641	1645
23.338	1.173	0.680	1067	1533
26.672	1.193	0.692	1283	1486
30.006	1.210	0.701	1407	1428

Table 3.15: Case 4: Relay Tripping Time

Tripping time (s)		
Penetration levels (MW)	Relay 1	Relay 2
1.667	no trip	0.3966
6.668	no trip	0.437
10.002	no trip	0.473
13.336	no trip	0.521
16.67	no trip	0.5714
23.338	no trip	0.709
26.672	no trip	0.722
30.006	no trip	0.739

The data gathered for Case 4 shows similar behavior to Case 2, in which the fault and PV are established at the same bus in the distribution feeder. Similar to Case 2, the PV impacts the system, creating an extreme scenario of delayed response from the relay scheme from Fig. 3.8 which will again lead to an eventual blinding condition as

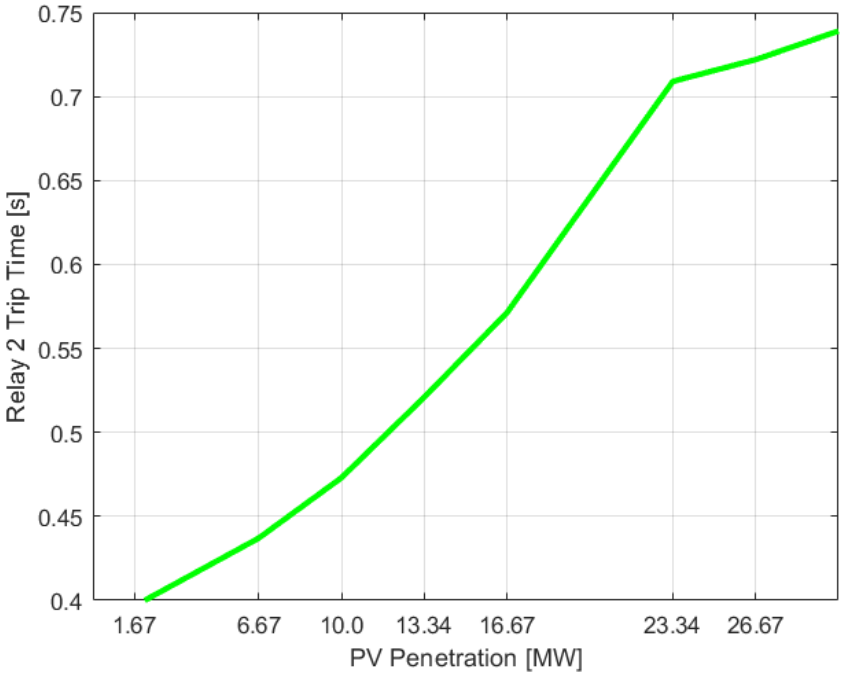

Fig. 3.8: Case 4: Relay 2 Tripping Time

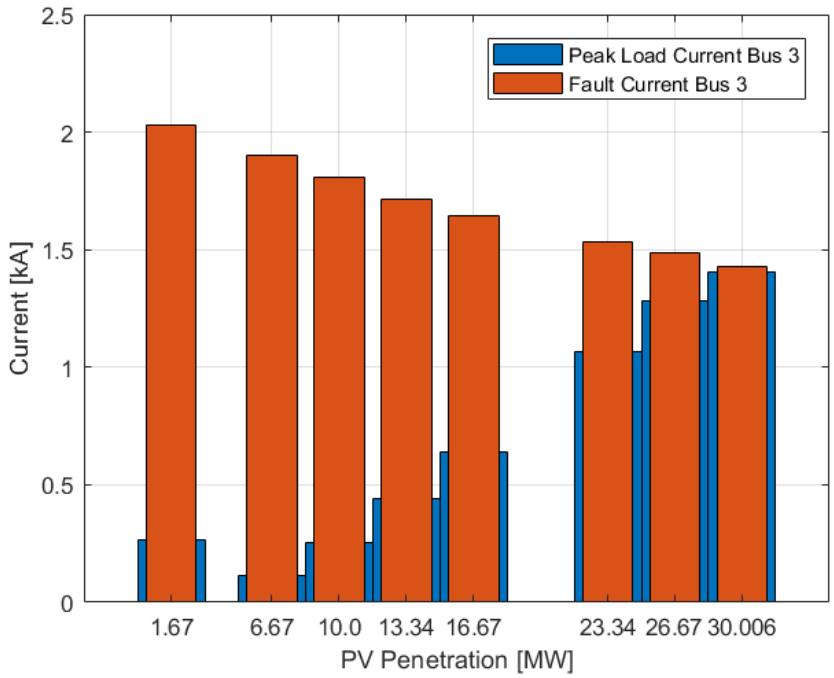

Fig. 3.9: Case 4: PV Penetration vs Fault Current Bus 3

the solar output is raised. From Fig. 3.9, it is clear to see the current magnitude during a fault at bus 3 decreasing when increasing PV penetration at that same location.

3.4 Simulation Summary and Significance

An investigation was carried out to identify impacts of solar PV farms on distribution feeder protection coordination. It was observed that a larger PV penetration level can reduce the fault current contribution from the substation, and create relay blinding conditions in which the protection system does not properly operate as designed. The simulated cases have demonstrated that the trip time of the protection relays is negatively impacted by increasing PV penetration levels, causing delayed response times, and even extreme conditions in which the relay may not even see the fault or clear it entirely.

Although newer adaptive relay designs have been proposed, these methods rely on completely new protection systems built from the ground up as opposed to integration with existing older structure. For example, one method proposes an adaptive overcurrent relay model capable of switching between islanded and grid-connected modes to adjust for variable fault current levels [53]. This technique, however, is not practical on preexisting older distribution networks which may have been in place for many years, and are now being forced to accommodate variable renewable generation.

The next section of this chapter examines the previously discussed data and attempts to recreate the power protection scenario using a 480V testbed to validate the results.

3.5 Development of a Distribution Feeder Testbed for Protection Systems Studies

3.5.1 Testbed Purpose

The previous section discusses the impacts of solar PV injection on distribution feeders regarding power system protection. In order to study the coordination challenges of distribution protection systems due to solar PV, a physical testbed circuit is being

designed and constructed as part of this thesis. This work is in support of a funded research project by the Solar Energy Technology Office (SETO) of the Department of Energy (DoE). The remainder of this chapter discusses the work performed for the DoE SETO project at the University of Oklahoma Laboratory for Electrical Energy and Power Systems (LEEPS).

The purpose of the DoE project is to study power system protection technologies to overcome integration issues of solar PV systems in distribution feeders. As smart grids continue to become integrated with renewable energy for additional power, traditional protection schemes already in place do not provide reliable response to inverter-based PV systems. Evaluating the vulnerabilities in these relay systems can provide a better understanding of the problems faced and shed light on possible solutions to solar PV integration in distribution systems.

3.5.2 Testbed Design and DER

The work carried out as part of this thesis contributed to key design elements designed for safe and expandable operation of the testbed. The testbed is designed to be flexible and re-configurable to mimic emerging problems with high penetration of DERs as previously highlighted in EMTP. A distribution testbed protection system (DTPS) is designed to act as a re-configurable distribution feeder capable of producing any of the four main common topologies: radial, mesh, parallel, and ring-type networks. In addition, multiple laterals are included in the design to mimic true distribution style power delivery systems. The testbed shall be capable of test voltages up to 480V three-phase medium voltage distribution at 200A.

A rack-mounted bus bar system was proposed and designed herein capable of conducting 480V at 200A max, which will comprise the foundation of the DTPS circuitry. A separate resistive-inductive series combination circuit is included to represent line elements typical of a medium voltage distribution feeder (designed separately). In order

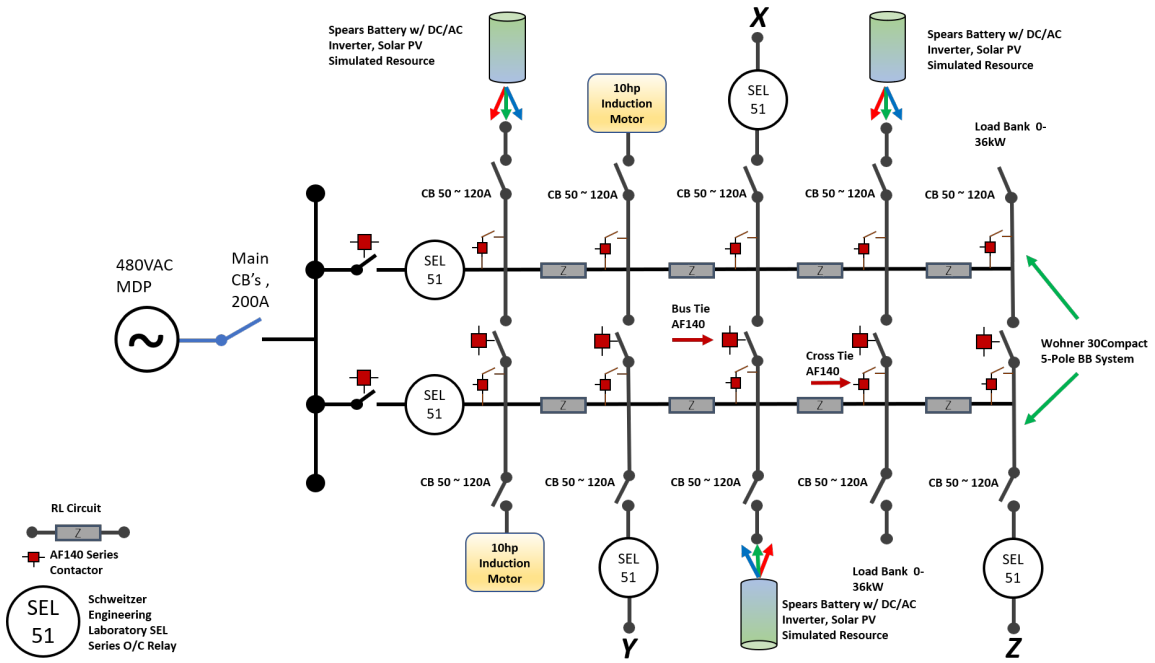

Fig. 3.10: Testbed Single Line Diagram

to provide the automated switching capability required to quickly change the feeder configuration of the DTPS, heavy duty contactors are placed throughout the circuit at each junction for cross tie connection and for the busbar ties. A 24 VDC control signal will trigger the open/close terminal action on each contactor, allowing quick transitions of the circuit reconfiguration without the need to manually disconnect and reconnect cabling.

Various inverter based resources (IBRs) are included in the design to inject power at specific locations similar to modern solar PV/inverter combinations used in distribution systems, such as batteries. These devices shall be installed at points of common coupling (PCC), the point at which the public utility system interconnects to the customer side electric power system via some interface (typically an inverter). Other load banks and induction motors will be connected to provide a realistic demand on the circuit. The IBRs consisting of DC/DC converters and DC/AC inverters provide fully programmable inverter controls to accurately reproduce the dynamic solar PV profiles experienced in modern systems by time of day, weather forecast, etc.

In Fig. 3.10, the contactors are shown in red at each cross tie and bus tie location for switching. The busbar pairs are pictured vertically, with connections to the local RL circuit if desired. Various relays will be included at the load locations (X, Y, and Z) for realistic mimicking of laterally placed relays in distribution feeders. These loads could be various types of motors, load banks, or other device which consumes power (see Fig 3.10.).

Finally, a computer system using a programmable logic controller (PLC) will be used in the DTPS to control switching events, monitor equipment statuses (temperatures checks, power,etc.), and provide a safe shutdown process in the event of an emergency during operation. The PLC and computer system will allow users to manage the DTPS remotely and troubleshoot system malfunctions without putting themselves at risk of electric shock. The main goal of the DTPS is to *intentionally* inject high current faults to study transient behavior, voltage sags or swells, and protective relay functions.

The next section of this chapter describes in detail, the construction of the busbar enclosure system used in the DTPS.

3.5.3 Circuit Construction - Prototype

Completing the physical build of this test system involves construction of the main busbar system which contains the physical copper bars used in power distribution for the 480VAC circuit. The components which comprise the circuit are housed in a dual equipment rack enclosure system designed to provide installation space and mobility to the DPST. This system must be capable of easy access for physical adjustment and adhere to proper safety protocol. Below is a list of critical components included in the DPST phase 1 installation prototype build.

- *Tripp-Lite SR48UBDPWD* - Large vented enclosure capable of holding up to 3000lbs of 19" rack rail mounted equipment and accessories. Rack measures

48 rack units (RU) high ($1RU = 1.75$”) and 45"D x 30"W and comes with removable side panels and doors. All components of the enclosure are grounded to the frame. Front and rear grounding points are provided for connection to the facility earth ground. Compliance with the following standards: RoHS, UL 60950, IP20. 2 x enclosures.

- *Wohner 30Compact BB System* - 480V, 200A rated 5-pole copper modular busbar system at 160mm. Neutral (N) and Protected Earth (PE) conductors are positioned between the three phases and connection sets for phases L1, L2, L3, N and PE are included which carry a maximum cable termination size AWG of 1/0 solid or stranded. Direct feed-through design allows for touch safe installation and termination at all connection points. Various adaptors for miniature circuit breakers (MCBs) at 63A and 105A are available with quick attach/release mechanisms for the addition of loads to simulate a true distribution system. 10 x busbar systems.

- *ABB AF-140-40-11-11* - 4 pole, 200A rated switching contactors capable of controlling power circuits up to 690 VAC. Dual add-on auxillary contact terminal blocks can be installed to incorporate 24V DC control signal(s) for automated opening and closing. Contactors feature reduced panel energy consumption, provide distinct opening and closing action, and can withstand brief voltage dips and sags. 15 x contactors.

- *SMRL SF2 Lead Wire* - 1/0 AWG stranded high wattage, power circuit lead copper wire suitable for applications up to 200 degrees Celsius at 200 V. Braided fiberglass jacket high heat and temperature tested with flame resistant compound. Silicone rubber insulation for extreme environments and flexibility allow cable to be scored precisely for accurate termination. Meets the following standards: UL 3231, CSA SEW-2 FTI, VW-1 flame test, IEEE 383 vertical flame test. 1000’ spool.

Strategically, the enclosure will allow for each busbar set (10 sets total) to be mounted across the 19" rear rack rails, using standard cage nuts and extra deep M6 rated machine screws for secure installation. The busbars will face into the center of the enclosure, allowing modular connections to be made quickly by accessing the rear door and removing the covers while the system is de-energized. Five weight rated vented 2RU shelves are installed across the front rack rails, which are designed to hold each pair of *cross-tie* contactors (5 pairs) used to connect to the RL circuit in the adjacent enclosure to the busbar system.

Five remaining individual bus tie contactors are mounted to vertical support bars specific to the enclosures to minimize the distance of cable required to connect to the busbars. Just as importantly, the vertical support bars provide various slots and teardrop holes useful for proper cable management inside the rack. All PE connections shall share a common wire connected to each busbar unit and terminated directly to the enclosure chassis for proper grounding at the extreme top and bottom via 3/8" lug nut. All three-phase and neutral connections between bus bar systems and their corresponding contactors shall be contained neatly and in a precise manner within the cable path. Velcro, cable ties and other management tools will be used to properly route all wires along each support column in a neat and professional manner.

The components in the phase 1 prototype build listed above are the *critical* items in this phase 1 build. Additional items such as mounting hardware, shelving, cable management and thermal regulation supplies were also included in the design. Several rack mountable SEL Type 51 relays will be installed in either enclosure after the busbar-to-contactor wiring is complete which includes installation of shelf-mounted CTs at each RL circuit tie contactor location for measurement purposes.

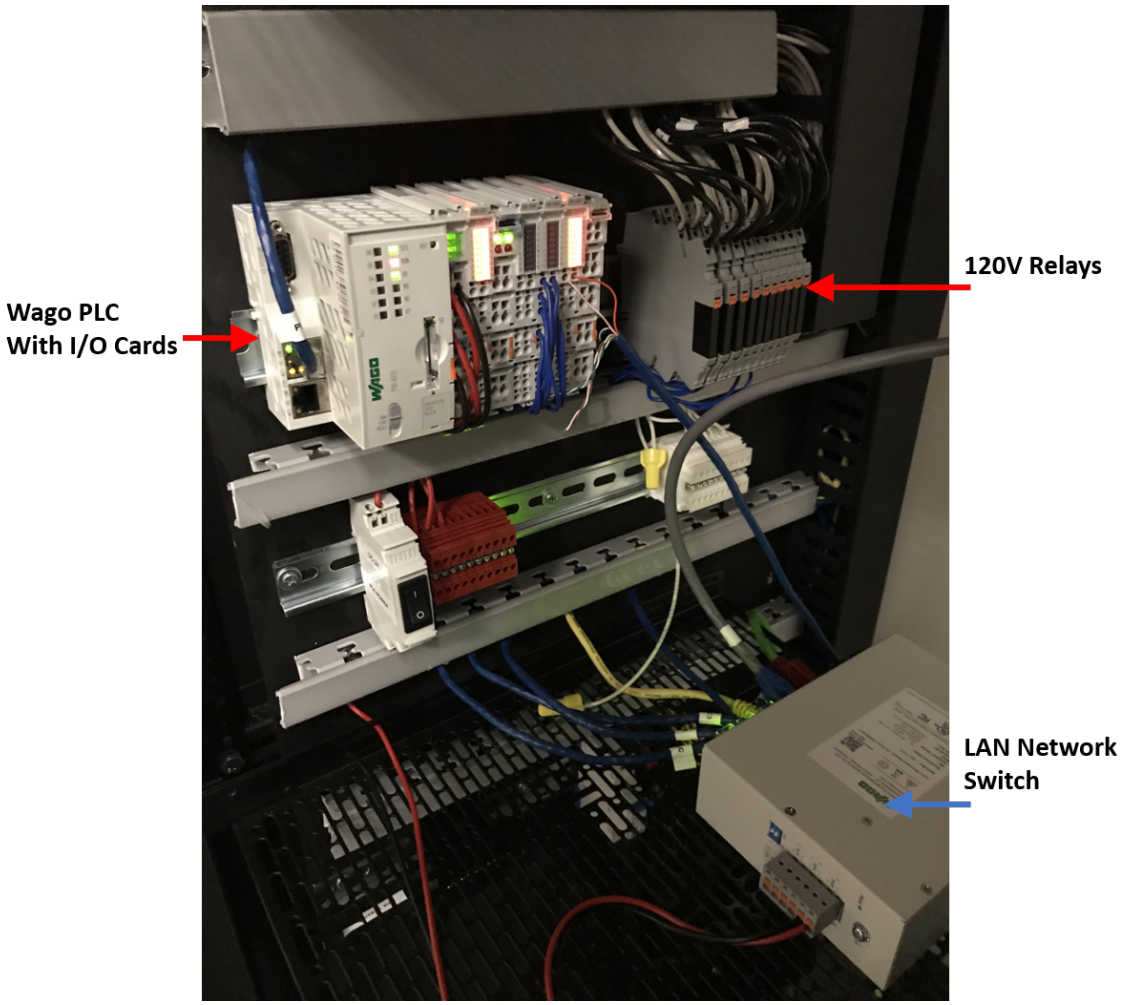

Fig. 3.11: Testbed PLC Control System

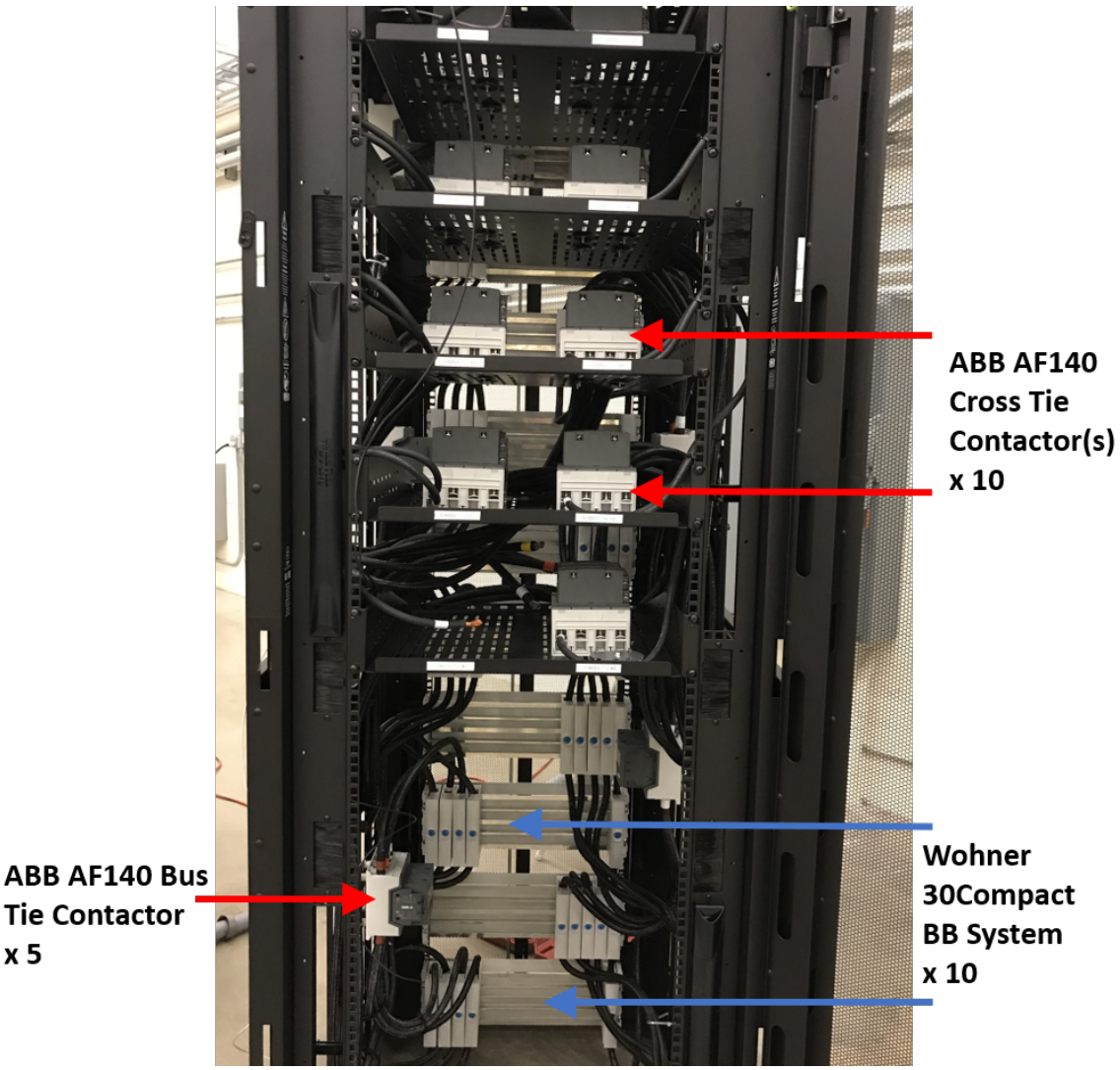

Fig. 3.12: Enclosure 1 Prototype

Fig. 3.13: Control Room Visual Display System

3.5.4 Testbed Control System

The control system for the DTPS is designed for remote data acquisition and monitoring of the physical hardware during live testing. A control room display system was designed and installed as part of this work consisting of a low voltage HDMI and CAT6 network for video and visual data monitoring of component statuses. Within the control room, multiple PC stations are located facing out into the test bay area, with 3 x 70" 4K HD displays mounted for visual data examination in real time. An 8 x 8 HDMI matrix video switch allows all local PC's immediate access to quickly send data to the larger displays for analysis. A supervisory control and data acquisition (SCADA) equipment rack was also designed and built containing low voltage equipment is used to house the PLC, various audiovisual control equipment and a terminal block system for low voltage signal rerouting via DIN rail mounted components.

Typical SCADA architecture involves a master controller communicating with all slave devices in the system via standard communication protocol. More importantly, this system is used in modern power applications for real-time data gathering and logging, while directly interacting with multiple devices within the network. This hierarchy

provides utilities the ability to mitigate system issues to avoid downtime. In this case, the testbed PLC acts as the master device, communicating through a local area network (LAN) as the central controller via Modbus TCP protocol.

Within the SCADA rack, various category six (CAT 6) shielded cable runs from the underlying communication network are connected to a locally housed switch for status indication on various components within the system. For example, a single CAT 6 connects to the control module responsible for monitoring a large 400 VDC battery energy storage system stored outdoors. In order to duplicate existing SCADA practices in utility grids, all protection relaying points will have data transmitted to the PLC as is common in substations.

Unfortunately, due to the impacts of COVID-19, the DoE project has suffered multiple setbacks and delays in equipment delivery and laboratory access. However, after completion of the testbed circuit and control system, a successful no load test was carried out on the DTPS. The main achievement(s) in this scenario are energizing the system and testing out the basic reconfigurability functions of the testbed for normal operation, without DERs.

3.6 Concluding Remarks

In conclusion, the significance of this chapter demonstrates the need for improved fault monitoring methods via protection system relays in distribution feeders. Multiple case studies conducted using various levels of PV penetration at locations in a 3-bus test network demonstrated the vulnerabilities of traditional relay time grading techniques considering large quantities of DER. Time graded protection systems exhibit a stronger susceptibility to blinding conditions due to excessive DG (which is increasing in smart grids each year). Therefore, new protection schemes are needed in order to adjust their sensitivities to the variable dynamics created by PV such as fluctuating fault current levels to accommodate the popular increase of solar PV penetration in distribution

feeders, while maintaining adequate protection coordination for the network.

A new distribution system protection testbed was developed and built as part of this work. The new testbed is part of a larger effort to better understand the weaknesses and complexities of large scale solar PV integration into distribution grids. This chapter has also shown the serious consequences of high PV penetration on power distribution protection relays using traditional time grading techniques. The data collected reinforces the need to develop improved protection schemes with evolving DERs in place on the smart grid. The next chapter discusses another aspect of integrating high penetration of solar PV onto distribution feeders which considers hosting capacity constraints arising from voltage profile and sizing issues.

CHAPTER 4

Multi-Objective Optimization of Solar Photovoltaics in Radial Distribution Feeders

Although research has shown the benefits of solar photovoltaic (PV) systems penetrating onto distribution grids, improperly sized and placed PVs can cause extreme over-voltages, higher power losses and grid capacity violations. In some cases, high PV penetration may lead to reverse power flow conditions and disruption of existing protection schemes, as explored in the previous chapter. This chapter proposes multiple improvements to an existing multi-objective optimization genetic algorithm (IMO) technique designed for PV sizing and site locations in radial distribution systems based on power loss reduction and limiting nodal voltage deviation.

The proposed algorithm and mathematical model yields a solution set of PV sizes based on bus location. The proposed approach aims to reduce the instances of voltage profile constraint violations across all laterals of the system, while improving power losses at each nodal location. The described method in this chapter is an improvement over previous works which were only applicable to single radial feeders without any branches, or focused on singularly localized PV sizing only. Second, a mathematical voltage deviation correction is considered which alters the multi-objective characteristic output, and suggests an alternative approach to solving the optimization objectives.

4.1 Solar PV Integration and Hosting Capacity Issues

Due to advancements in communication protocol, cloud-based data storage, and enhanced control systems, smart grid systems have become more popular worldwide [54]. Smart homes are equipped with monitoring technology to maintain flexibility and al-

low for consumer control [4]. The importance of proper grid planning by the utility cannot be understated, and consideration of system sustainability and efficiency are of the upmost importance. Forecasting of future load demand and power loss estimation in smart grid systems must also take into account demand-side participation of DG.

Studies have shown the importance of DG to help support peak demand and reduce power losses, while also improving the overall system voltage profile in radial distribution systems [55]. By providing power loss reduction and maintaining a low environmental impact, the benefits of DG are clearly recognizable. However, improper sizing and placement of DG can lead to a plethora of problems in the modern day smart grid. Capacity violations on heavily supplied nodes can produce extreme overvoltages, leading to reverse power flow conditions, loss of protection relay coordination, and system instability [56].

Several methods have been proposed for proper optimization of integrated solar photovoltaics (PV) in distribution systems based on various objectives (e.g. cost, power losses, geographical location, etc.). Multi-objective methods allow for multiple parameter optimization under specific conditions, such as [57], which proposes a *Local Search Optimization* to determine placement of various DG sizes on a radial feeder using a forward/backward sweep technique. Alternatively, [22] evaluates PV placement for power loss reduction and voltage profile improvement of radial systems using a *Particle Swarm Algorithm*. Both [31] and [30] propose a multi-objective approach based on time-varying load models to optimize real and reactive power losses with voltage deviation improvements.

These methods, however, focus on optimization of a *single* grid-connected PV source only in a simple radial distribution system. This chapter proposes an alternative improved sizing method to the multi-objective optimization index (IMO) suggested in [30] for optimization of single source radial distribution feeders in an IEEE 33-bus system with multiple laterals. The mathematical model aims to appropriately size

and place PV, using various impact indices to minimize active and reactive power losses while maintaining the voltage profile within regulatory limits. The results of the simulation(s) will show the effectiveness of optimizing multiple solar grid-connected PV to improve radial distribution feeder power losses and voltage deviation.

This work is structured as follows. Section 4.2 describes the fundamental power flow in a radial feeder, and Sections 4.3 and 4.4 discuss the detail of the IMO and both sizing methods. Section 4.5 describes the analysis and test results from simulation of the PV sizing and placement on two separate networks. Section 4.6 concludes the study with final takeaways and an overview of the results, and Section 4.7 describes a fundamental mathematical formulaic correction which was not originally used in this study, but provides relevant data which suggests an alternative approach to PV sizing and placement using the IMO.

4.2 Radial Distribution Feeder Power Flow

Prior to investigating the IMO and proposed algorithm, it is important to verify the fundamental equations used in this study. One of the most important concepts to power engineering is the *power triangle* shown below in Fig. 4.1. This section describes the relationship between real and reactive power, and how this relationship pertains to power flow in a radial distribution feeder.

Here, *Apparent Power (S)*, which is the combination of both *Real Power (P)* and *Reactive Power (Q)*, is shown as the hypotenuse of the *power triangle*. The Greek symbol δ is referred to as the *phase angle* which determines the *power factor* of the system. Apparent power is also given as the relationship between voltage and current phasors in a power system, where $\bar{I}^*$ is the complex conjugate of $\bar{I}$. These equations are vital in determining the calculated power injections (and losses) per bus in a distribution system. Following equations 4.1 and 4.2 is an example single line diagram consisting of a 2-bus, radial feeder with basic line impedance Z model.

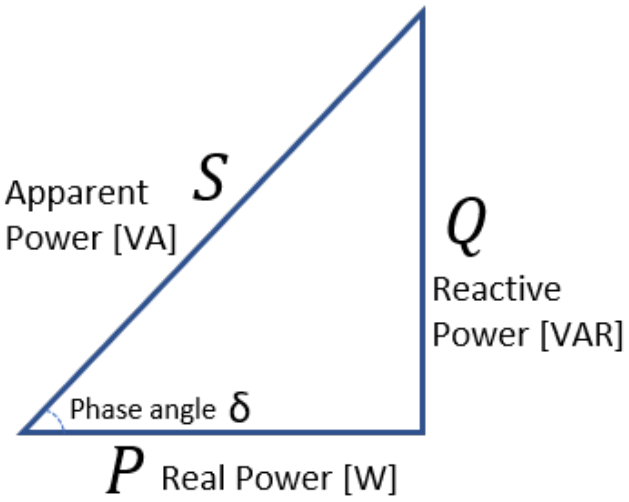

Fig. 4.1: Power Triangle

$$\bar{S} = P + jQ \tag{4.1}$$

$$\bar{S} = \bar{V}\bar{I}^{*} \tag{4.2}$$

$$\bar{Z} = R + jX \tag{4.3}$$

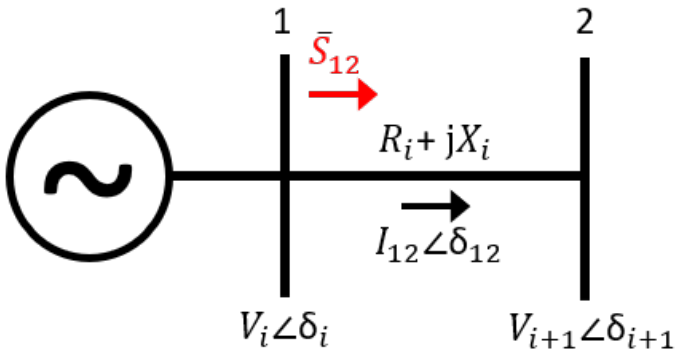

Fig. 4.2: 2-Bus Radial Distribution Feeder Single Line Diagram with No Load

In Fig. 4.2, the voltages of each bus are modeled according to magnitude and phase angle, with reference direction of the current shown moving from bus 1 to bus 2. The line between both buses consists of a typical impedance Z combination of a resistive

and reactive component. From equations 4.1 and 4.2, the flow of power from the slack bus to bus 2 is given as S_{12} in the radial feeder.

From the power equation $P = V * I$ for all elements (absorbed or supplied) and *Ohm's Law*, the power lost during delivery between nodes can be derived. For a typical circuit, line losses are tabulated according to the real and reactive properties of the line, the current in the line, and the local bus voltages therein.

$$P = V * I \tag{4.4}$$

$$V = I * R \tag{4.5}$$

Substituting for voltage,

$$P = V * I = I * R * I = I^2 * R$$

$$P_l = I^2 * R \tag{4.6}$$

$$Q_l = I^2 * X \tag{4.7}$$

Note that real, or active, power is the true amount of power absorbed or supplied in the circuit, while reactive power is associated with inductive and capacitive elements on the line and load.

Expanding from equations 4.1, 4.2, and 4.4,

$$\bar{S} = P + jQ = \bar{V}\bar{I}^*$$

$$I^* = \frac{P + jQ}{|V|}$$

or

$$I = \frac{P + jQ}{V^*}$$

Substituting active line loss, $P_l = I^2 * R$,

$$I * I^* = |I|^2$$

$$\frac{P_l}{R} = \frac{P^2 + Q^2}{|V|^2}$$

$$P_l = \frac{P^2 + Q^2}{|V|^2} * R$$

Through this derivation, the total active power loss P_L in [W] per phase over a line from node to node is given using the active and reactive powers, voltage, and resistance between buses. Reactive losses are determined in the same fashion using equation 4.7. It should be noted that this approximation is important in determining losses in a radial distribution feeder considering PV deployment. [58]. This approximation shows that both real and reactive power contribute equally to the real power line losses.

In a single source radial distribution feeder, power flows from the source to the load, where the power is absorbed and losses accumulate further down the feeder. However, introducing solar PV at bus locations means that power is injected locally and losses can be reduced with careful calculation. These methods are examined throughout this chapter to demonstrate the positive impacts of multiple solar PV injections along a single radial network.

4.3 Multi-Objective Optimization of Solar PV using the IMO

The *Multi-Objective Index (IMO)* defined in [30] is extended here with additional formulation for greater generality to different feeder topologies. The original and extended definitions of the IMO are defined and compared herein.

4.3.1 Multi-Objective Index Definition

The IMO definition in [30] uses an analytical expression with multiple impact indices to minimize active power loss, reactive power loss, and voltage deviation. Typically, PV allocation for planning focuses on a single objective minimization which most benefits the utility and conserves energy during peak hours (i.e. power losses, capacity hosting, etc.) However, if a single PV array is sized based on real or reactive power loss, a threshold is placed on the degree of penetration due to voltage deviation constraints. On the contrary, a larger penetration can improve the system voltage profile but power loss reduction is limited. Therefore, the *IMO* attempts to optimize both parameters. The governing IMO optimization equation is given by

$$IMO = \sigma_1 \frac{P_{LPV}}{P_L} + \sigma_2 \frac{Q_{LPV}}{Q_L} + \sigma_3 \frac{VD^2_{PV}}{VD^2} \tag{4.8}$$

From 4.8, P_L, Q_L are the active and reactive power losses and VD^2 is the voltage deviation squared for a base case load flow analysis with no PV connected to the distribution grid.

$$P_L = \sum_{i=1}^{n} \frac{P_i^2 + Q_i^2}{|V_i|^2} R_i \tag{4.9}$$

$$Q_L = \sum_{i=1}^{n} \frac{P_i^2 + Q_i^2}{|V_i|^2} X_i \tag{4.10}$$

$$VD^2 = \sum_{i=1}^{n} \frac{(R_i P_i + X_i Q_i)^2}{|V_{i+1}|^2} \tag{4.11}$$

P_{LPV}, Q_{LPV}, *and* VD^2_{PV} are the active and reactive power losses at a grid-connected PV location and voltage deviation squared at a grid-connected PV location. σ_N are the weighted factors (0.5, 0.25, 0.25) determined by the local utility and planning

committees (Note the relative importance on real power). These values may be adjusted based on local utility regulations, load and power forecasting, feeder design and various additional factors [31].

4.3.2 Solar PV Sizing and Placement

The IMO defines optimal sizing and placement based on power losses and includes a voltage profile improvement in the form of a deviation reduction. Thus, to specify the *minimum* IMO value as the calculated PV sizing for a particular branch or bus of the network, the partial derivative of 4.8 is taken with respect to P_{PVK} and set equal to zero in 4.12.

$$\frac{\partial IMO}{\partial P_{PVK}} = \frac{\sigma_1}{P_L}\frac{\partial P_{LPV}}{\partial P_{PVK}} + \frac{\sigma_2}{Q_L}\frac{\partial Q_{LPV}}{\partial P_{PVK}} + \frac{\sigma_3}{VD^2}\frac{\partial VD_{PV}^2}{\partial P_{PVK}} = 0 \tag{4.12}$$

The PV model given in 4.13 from [30] is designed to show the relationship between active and reactive power at a grid connected PV inverter, where pf equals the operational power factor of the PV unit at *bus k*. The partial derivatives of P_{LPV}, Q_{LPV}, and VD_{PV}^2 with respect to P_{PVK} are derived as follows:

$$Q_{PVK} = a_k P_{PVK}, a_k = \pm\tan(\arccos(pf_{PVK})) \tag{4.13}$$

$$\frac{\partial P_{LPV}}{\partial P_{PVK}} = -2A_k + 2C_k P_{PVK} - 2B_k a_k + 2C_k {a_k}^2 P_{PVK} \tag{4.14}$$

$$\frac{\partial Q_{LPV}}{\partial P_{PVK}} = -2D_k + 2F_k P_{PVK} - 2E_k a_k + 2F_k {a_k}^2 P_{PVK} \tag{4.15}$$

$$\begin{aligned}\frac{\partial VD_{PV}^2}{\partial P_{PVK}} = 2G_k P_{PVK} - 2H_k + 2I_k {a_k}^2 P_{PVK} - 2J_k a_k \\ -2K_k a_k - 2L_k + 4M_k a_k P_{PVK}\end{aligned} \tag{4.16}$$

$$A_k = \sum_{i=1}^{k} \frac{R_i P_i}{|V_i|^2} \tag{4.17}$$

$$B_k = \sum_{i=1}^{k} \frac{R_i Q_i}{|V_i|^2} \tag{4.18}$$

$$M_k = \sum_{i=1}^{k} \frac{R_i X_i}{|V_{i+1}|^2} \tag{4.19}$$

Before proceeding with the IMO model, the provided partial differential equations which ultimately determine the optimal PV size P_{PVK} are derived for verification of the constant values A_k, B_k, ...M_k. Equation 4.12 is determined from the given loss equations *with* a local PV at the respective bus i under study for all buses of the system through bus k. For example, to derive equation 4.14 for the active power loss index, beginning from the active power loss equation at a local bus with a grid-connected solar PV.

$$P_{LPV} = \sum_{i=1}^{k} \frac{P_{PVK}^2 - 2P_i P_{PVK}}{|V_i|^2} R_i + \frac{a_k^2 P_{PVK}^2 - 2Q_i a_k P_{PVK}}{|V_i|^2} + P_L \tag{4.20}$$

Solving the partial derivative with respect to P_{PVK}, equation 4.20 becomes

$$\frac{\partial P_{LPV}}{\partial P_{PVK}} = \sum_{i=1}^{k} \frac{2P_{PVK} - 2P_i}{|V_i|^2} R_i + \frac{2P_{PVK} a_k^2 - 2Q_i a_k}{|V_i|^2} R_i$$

The resulting expansion proves equivalent to the given partial derivative in 4.14, where each resulting term contains the constants A_k, B_k, and C_k.

$$\frac{\partial P_{LPV}}{\partial P_{PVK}} = \sum_{i=1}^{k} [2P_{PVK} R_i - 2P_i R_i + 2a_k^2 P_{PVK} R_i - 2Q_i a_k R_i] \frac{1}{|V_i|^2}$$

Similarly, the reactive loss component index of the IMO is derived from the reactive

power loss equation at a local bus with a grid-connected solar PV as

$$Q_{LPV} = \sum_{i=1}^{k} \frac{P_{PVK}^2 - 2P_i P_{PVK}}{|V_i|^2} X_i + \frac{a_k^2 P_{PVK}^2 - 2Q_i a_k P_{PVK}}{|V_i|^2} + Q_L \tag{4.21}$$

Solving the partial derivative with respect to P_{PVK}, equation 4.21 becomes

$$\frac{\partial Q_{LPV}}{\partial P_{PVK}} = \sum_{i=1}^{k} \frac{2P_{PVK} - 2P_i}{|V_i|^2} X_i + \frac{2P_{PVK} a_k^2 - 2Q_i a_k}{|V_i|^2} X_i$$

Again, the resulting expansion proves equivalent to the given partial derivative in 4.15, where each resulting term contains the constants D_k, E_k, and F_k.

$$\frac{\partial P_{LPV}}{\partial P_{PVK}} = \sum_{i=1}^{k} [2P_{PVK} X_i - 2P_i X_i + 2a_k^2 P_{PVK} X_i - 2Q_i a_k X_i] \frac{1}{|V_i|^2}$$

From verification of the partial derivatives for both the active and reactive power loss indices and voltage deviation, the complete minimal P_{PVK} size can be calculated by substitution in equation 4.22. It should be noted that the remaining constants for the voltage deviation index (G_k, H_k,...M_k) which are derived in a similar fashion are not shown due to repetitive procedure, but were verified mathematically. Here, the optimized PV size P_{PVK} based on these parameters is determined, per bus location.

$$P_{PVK} = \frac{\frac{\sigma_1}{P_L}(A_k + a_k B_k) + \frac{\sigma_2}{Q_L}(D_k + a_k E_k) + \frac{\sigma_3}{VD^2}(H_k + a_k J_k + a_k K_k + L_k)}{\frac{\sigma_1}{P_L}(C_k + {a_k}^2 C_k) + \frac{\sigma_2}{Q_L}(F_k + {a_k}^2 F_k) + \frac{\sigma_3}{VD^2}(G_k + {a_k}^2 I_k + 2a_k M_k)} \tag{4.22}$$

Constants A_k, B_k and M_k describe the relationship between the given parameters for a grid-connected PV array at bus i through bus k. This sizing technique shall be identified as *Method One* from [30]. Once substituted into 4.22, the expression determines the minimum PV output power P_{PVK} using the relationship from 4.13 and an assumed a_k value or *power factor*.

As an alternative, this work proposes a second PV sizing technique used to obtain each constant value A_k, B_k, ...M_k, which takes into account the location of the IMO evaluated at any specific *bus k* directly to the source of generation via the shortest physical line path. These constant values are simply a series of running sum totals moving from the slack bus out to the final bus, and any linear radial distribution system with T-branches must correctly account for true electrical distance to the source, regardless of bus index value or location. This correction for true PV location-based sizing shall be identified as *Method Two*. Finally, P_{PVK} is also subject to the single objective function of minimizing active power loss with a bus voltage profile constraint of 1 ± 0.05 p.u.

4.4 Proposed Shortest Electrical Path Identifier - *Method Two*

In this section, a PV sizing optimization formulation model is proposed to appropriately appropriately consider the true electrical topology of radial distribution feeders with multiple branches which was not considered in the previous study. The constants provided in the previous section using *Method One* are effective, but do not adequately optimize solar PV for losses and voltage correction for locations not along the main feeder, such as lateral lines (which may go off into a separate zone or district). This simple adjustment accounts for the change in topology and true electrical distances between solar PV sites to the source. The algorithm for achieving this is as follows.

1 Assuming a radial feeder with multiple laterals and a single source of power generation, identify the line(s) connecting the branch to the main feeder as l_{b1b2}. The two buses on each end of the line shall be b_1 on the main feeder and b_2, the first bus on the T-branch.

2 Create an ordered set (array) $B_n\{\ \}$ of bus index values starting with the slack bus moving sequentially to bus b_1 then across line l_{b1b2} to bus b_2 out to *bus k*.

3 The set of ordered buses $B_n\{\ \}$ now contains the path of least impedance for power flow from the source to a grid-connected PV module located at any T-branch on *bus k*.

4 Recalculate PV sizes using IMO at each bus in the network.

The mathematical model for the proposed *Method 2* is derived as follows. From *Method One*, 4.17, 4.18, and 4.19 become

$$A_k = \sum_{i \in B_n\{\}}^{k} \frac{R_i P_i}{|V_i|^2} \tag{4.23}$$

$$B_k = \sum_{i \in B_n\{\}}^{k} \frac{R_i Q_i}{|V_i|^2} \tag{4.24}$$

$$M_k = \sum_{i \in B_n\{\}}^{k} \frac{R_i X_i}{|V_{i+1}|^2} \tag{4.25}$$

For example, suppose that a grid-connected PV *bus k* occurs at bus 21 on the IEEE 33 bus radial distribution system. From step 1 above in the *Shortest Path Identifier*, l_{b1b2} becomes l_{b2b19}. Moving from the slack bus out to bus 21 (*bus k*), $B_n\{\} = \{1, 2, 19, 20, 21\}$. This is opposed to *Method One* which computes $B_n\{\}$ as the entire set of buses from 1 to *bus k*. The differences in both methods are illustrated in Fig. 4.3.

Shown in red, the sizing approach for *Method One* would not correctly account for location and line impedance from source to PV at bus 21. Instead, the result of the sizing constant is modeled based on a single radial feeder topology which places the indexed branches after bus 18 due to the summation of bus indices. This leads to an incorrect path of impedance for power flow calculations and will produce a P_{PVK} size which could potentially cause poor system performance. The proposed *Method Two* shown in green, displays the correct path for sizing which allows for proper single

PV allocation at the specified location. The resulting P_{PVK} will accurately reflect the results of a correct power flow calculation with a grid-connected PV of specified size at *bus k*.

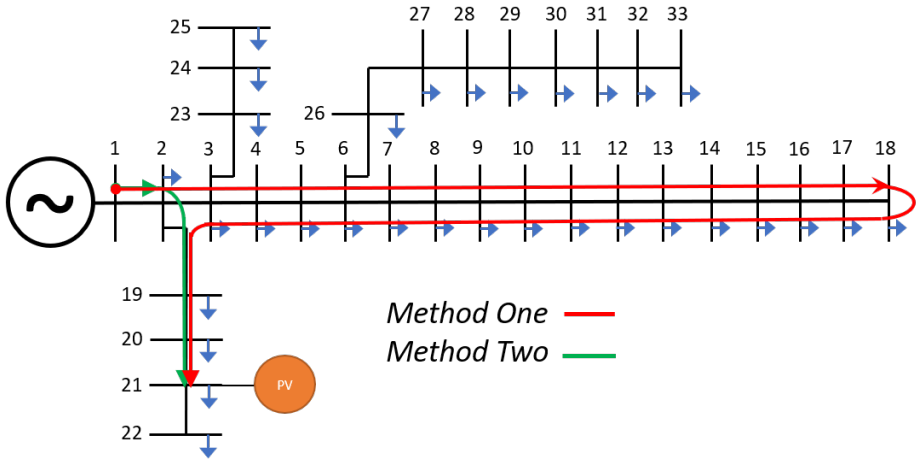

Fig. 4.3: PV sizing path Bus 21 - *Method One vs. Method Two*

The computational algorithm for implementing *Method 2* using a multi-solar PV optimization allocation in a radial distribution feeder is summarized as follows.

1 Run a power flow with zero PV connected and calculate P_L, Q_L and VD^2 from [30]. This is the *base case*. Plot the system voltage profile for later use.

2 Calculate 4.12 from 4.8 at each bus using *Method One* and *Method Two*.

3 Test all P_{PVK} sizes and evaluate a load flow for each size at the particular bus or branch from the IMO results, and calculate power losses per PV size. Compare.

4 Using the results from *Method Two* only, identify the pair of buses or branches of the network subject to the single objective: minimum power loss. The P_{PVK} result from step 3 will be used here for power loss improvement.

5 From step one, identify the two buses which most violate the constraint 1 ± 0.05 p.u (or deviate furthest from 1.0 p.u.). For the bus which most violates this constraint, that particular P_{PVK} value is used for voltage profile improvement.

6 Test the four various PV size combinations together at the designated location(s) from the IMO.

4.5 Test Results and Analysis

In this section, a series of simulations are carried out to demonstrate the validity of the proposed algorithm. Two separate radial networks are considered for testing purposes and validation of the techniques for optimization of solar PV using the Multi-Objective Index. The simulation approach is described followed by a comparative analysis of Methods 1 and 2 results followed by a voltage deviation correction on the larger network.

First, a smaller 6-bus network from [59] is considered for simple verification of the IMO. This system contains no additional T-branches and models a single linear radial feeder by which the newly proposed sizing model *Method Two* is not applicable. Second, the IEEE 33-bus system with multiple T-branches is tested using both sizing methods, with an expansive technique applied to the multi-solar allocation approach for solar PV optimization.

4.5.1 System(s) Under Study

The simulations are conducted using *PandaPower 2.2.2* [59] with *Python 3.7.4*. All *PandaPower* power flow methods employ a balanced AC Power Flow using the *Newton-Raphson* method. From equation 4.13, a unity power factor is assumed for all testing, producing an a_k of zero for both networks. Any and all tie lines are left open and disconnected and *PandaPower* power flow results folders tabulate line losses to verify all *base case* calculations. Details of each network and the associated parameters are listed below, aside an appropriate single-line diagram for reference.

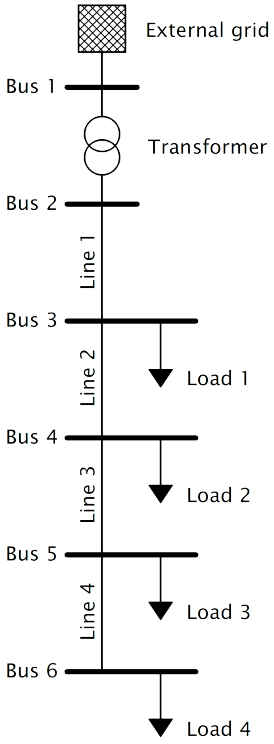

Fig. 4.4: PandaPower 6-Bus Radial Network

- 6 Bus Radial System used for IMO unit testing and formula verification
- 10kV ext grid connection (primary), 0.4kV Vbase (secondary)
- 1MVA Sbase
- Four identical loads at $0.03MW$ and $0.01MVAR$

- 33 Bus Radial System used for IMO expansion and sizing model correction
- 3 Separate T-style radial branches containing 15 loads
- 5 Tie lines (left open, disconnected)
- 1MVA Sbase
- 32 loads with a total combined demand of $3.7MW$ and $2.3MVAR$

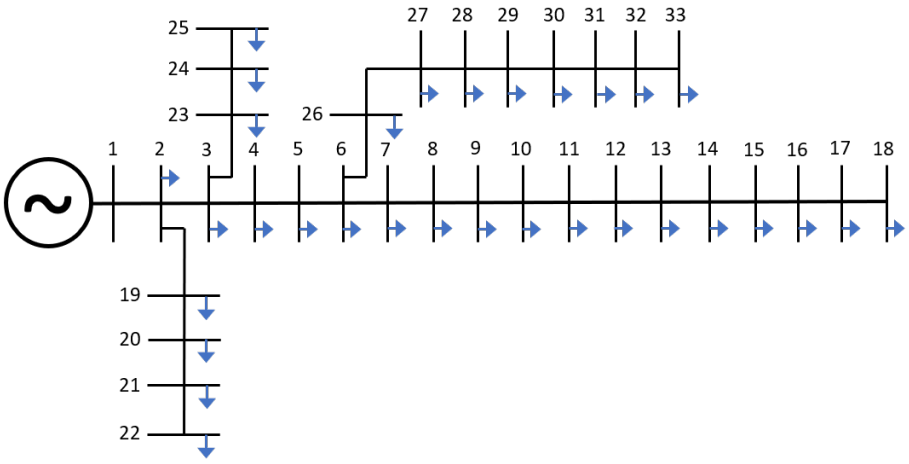

Fig. 4.5: IEEE 33 Bus Radial Distribution System

4.5.2 Base Case Load Flow Results

Results of the initial *base case* load flow (with no PV connected to the test system(s)) are shown in Tables 4.1 and 4.2. The smaller network shows an active power loss of 6.76 kW and a reactive power loss of 2.4 kVAR, while the larger network load flow provides a resulting total active power line loss of 202.7 kW and reactive power loss of 135.1 kVAR. It should be noted that after running a power flow in the *base case*, the losses calculated by both the derived equations for P_L and Q_L, and the line losses summed from *PandaPower* are equivalent in *both* networks, thus validating the loss equations. The corresponding voltage profile of each system is shown below for reference to voltage deviation per bus.

Table 4.1: Base Case Power Losses 6-Bus System

Base Case Power Loss Comparison	
Active Power Loss [kW]	Reactive Power Loss [kVAR]
P_L	Q_L
6.76	2.4
$P_{L_{PP}}$	$Q_{L_{PP}}$
6.76	2.4

It becomes clear to see that the voltage magnitude of each bus in a radial distribution feeder drops further away from 1.0 p.u. as distance from the source increases. Bus 6 on the smaller network and buses 18 and 33 in the larger network show the furthest

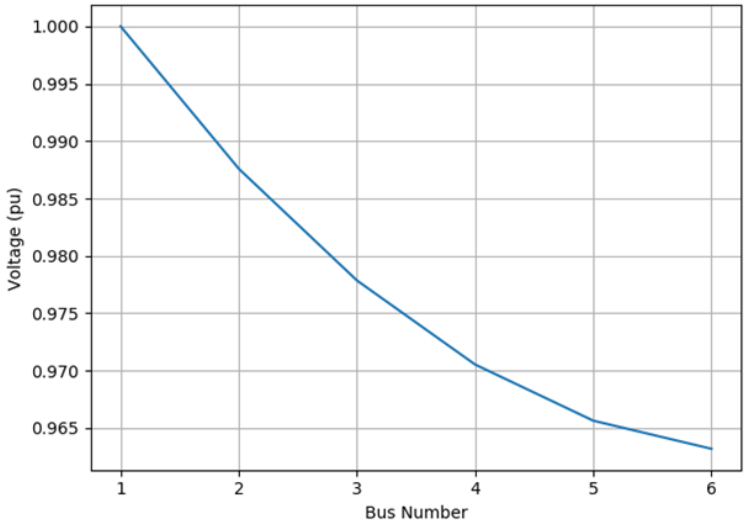

Fig. 4.6: Base Case System Voltage Profile PP 6-bus system

.

deviation from the base voltage of each system. From [57], these buses are an optimal target for introducing solar PV to offset this deviation.

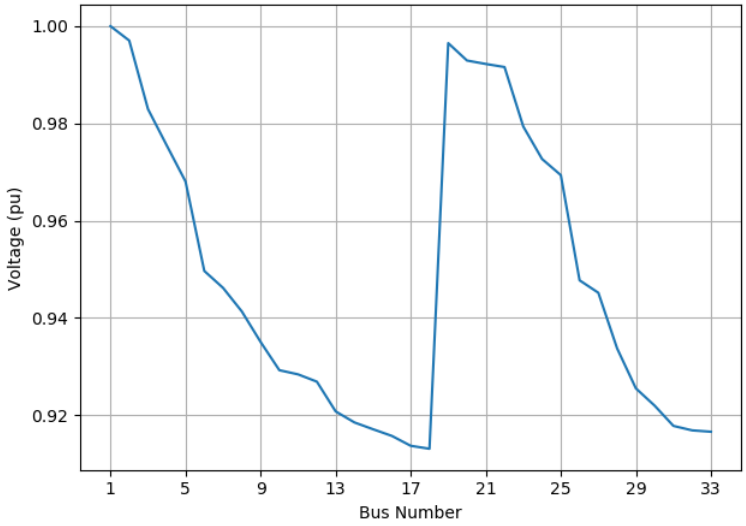

Fig. 4.7: Base Case System Voltage Profile IEEE 33-bus system

.

4.5.3 PV Sizing and Loss Determination

The results of the IMO using *Method One* on the 6-bus system yield the following PV sizes in Table. Due to the step down transformer between buses 1 and 2, only buses

Table 4.2: Base Case Power Losses 33 Bus System

Base Case Power Loss Comparison	
Active Power Loss [kW]	Reactive Power Loss [kVAR]
P_L	Q_L
202.7	135.1
$P_{L_{PP}}$	$Q_{L_{PP}}$
202.7	135.1

3-6 are considered for PV sizing and placement.

Table 4.3: PV sizing and Associated Power Loss 6-Bus System

IMO PV Sizing with losses			
Bus	PV Size[MW]	$P_L[kW]$	$Q_L[kVAR]$
3	0.12557	3.419	1.208
4	0.10939	1.729	0.607
5	0.09336	1.238	0.432
6	0.07751	1.634	0.573

From Table 4.3, the results of the IMO using *Method One* (both methods produce equivalent results on any singular radial feeder with zero branches) yields an optimal sizing of 0.09336 MW at bus 5, with relative calculated sizes at the other buses. When each determined size is connected to its respective bus and a power flow is performed on the system, the active and reactive power losses are given, with the objective $P_{loss}(min)$ occurring at bus 5 with $P_L = 1.238$ kW. Thus, from step 3, bus 5 is identified as the critical bus location for power loss compensation via grid connected PV integration for this system.

After evaluating the IMO for both *Method One* and *Method Two* on the 33-bus system, both approaches provide a set of PV sizes ranging from 0.31 MW to 3.98 MW based on bus location. It should be noted that the sizes determined by both methods for buses 1-18 are nearly equivalent due to location on the main feeder. *However*, the results for buses 19-33 differ drastically because the proposed method takes into consideration the true electrical distance from the source. The sizing charts in Fig. 4.9 show how *Method One* will produce decreasing sizing results as the distance from bus to generation is

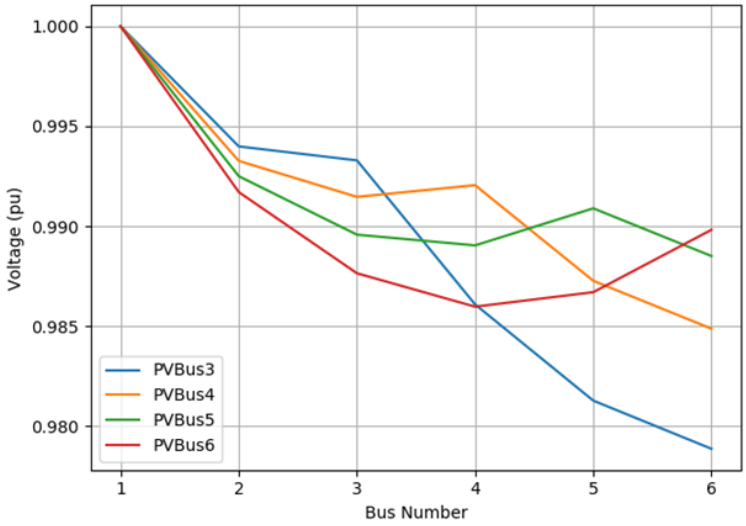

Fig. 4.8: IMO PV Sizes System Voltage Profile(s) 6-Bus Radial Network

.

increased. The *Method Two* mathematical model produces PV sizing consistent with [60] based on the shortest, direct electrical path to the grid.

From step 3, active power losses are calculated as each P_{PVK} IMO result is tested at its respective bus/branch location according to both methods. Power loss results due to PV sizing are compared in Fig. 4.10 to relate the calculated sizes to the single objective $P_L(min)$. The losses tabulated along the main feeder, again, are equal between both methods. However, active power losses across the branches of the network using *Method One* do not drop below 140 kW. This leads to an inaccurate summation model for buses on any branch when calculating each constant from 4.17, 4.18, through 4.19 which neglects the true electrical path from generation to *bus k*.

In contrast, *Method Two* accounts for line impedance path in the power flow from each *bus k* and produces P_{PVK} PV sizes for each bus which show reduced power losses beginning at bus 19 through bus 33 compared to *Method One*. This becomes more evident as the distance from the source increases. For example, all active losses on the last branch from buses 26 - 33 are reduced by a combined average of 14.3% at 121.2 kW from *Method One* at 141.4 kW.

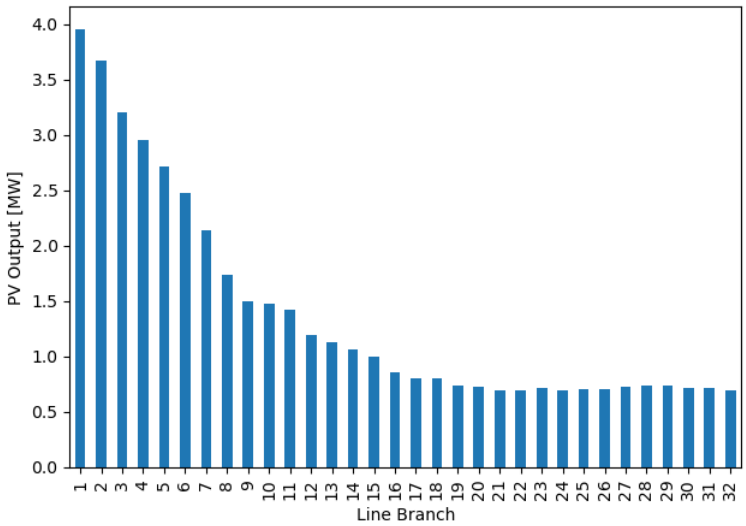

(a) Method I

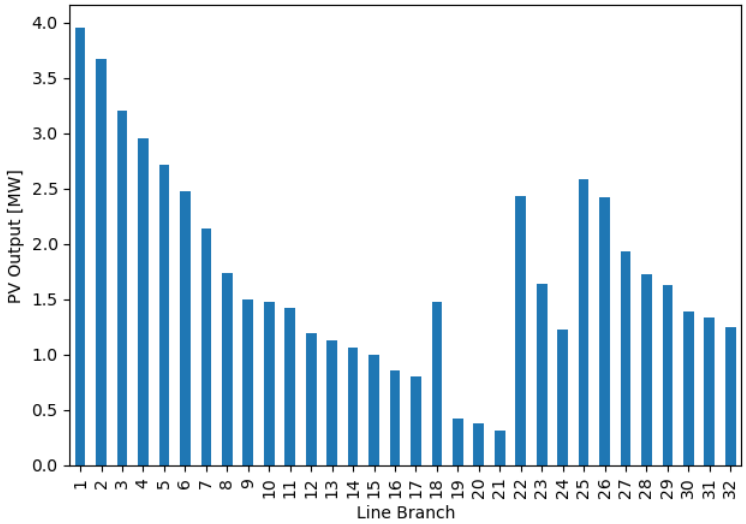

(b) Method II

Fig. 4.9: IMO PV Sizing Comparison.

Voltage profiles for each calculated IMO PV size at the designated bus are shown in Fig. 6. In this scenario, a single grid-connected PV is connected to the distribution system at the appropriate bus location, sized according to the IMO, with system voltage profiles plotted after a power flow is conducted. For each case of a single PV, the voltage profiles of the system for both methods are shown.

It is clear from Fig. 4.11 that the resultant PV sizes using *Method One* and *Method Two* produce system voltage profiles which are closely related along the main feeder

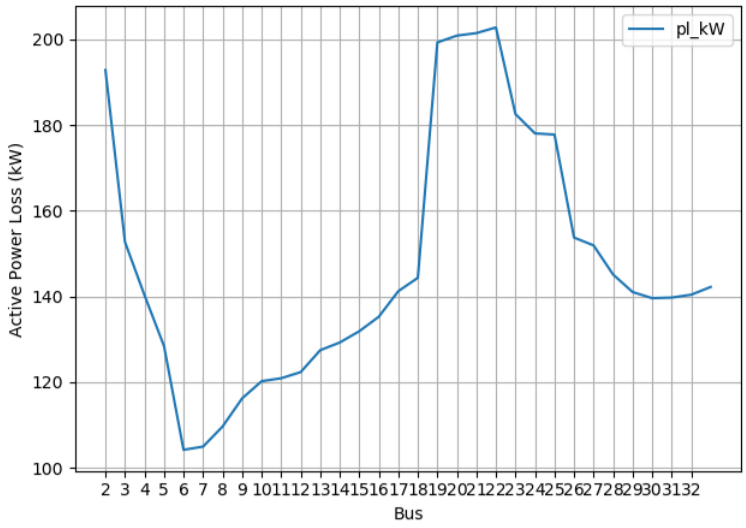

(a) Method I Bus Power Losses

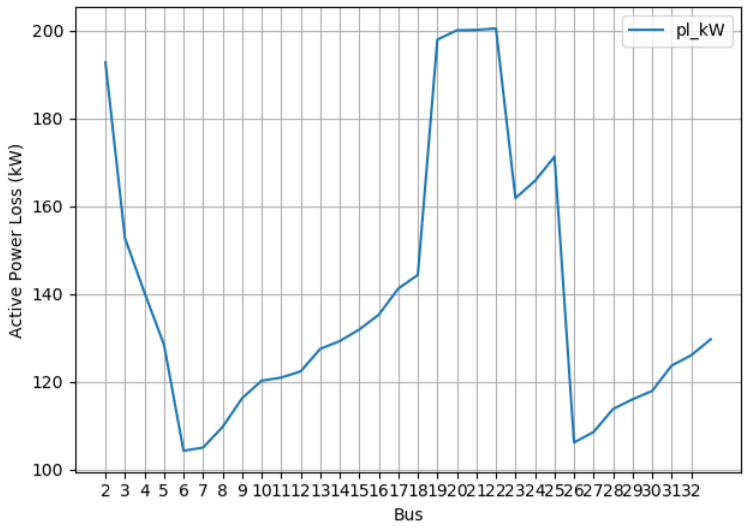

(b) Method II Bus Power Losses

Fig. 4.10: IMO PV Sizing Active Power Loss Comparison.

(up to bus 18), yet differ in p.u. magnitude from buses 19 - 32, which includes all three T-Branches in the system. Here, it is clearly visible to see the differences made by appropriate PV sizing per bus location via the IMO, as distance from bus_k to the generator is taken into account. Appropriate sizing for the first branch using *Method Two* shows all bus voltages just under 1 p.u. However, *Method One* results for PV sizing demonstrate a less desirable voltage profile with multiple cases of 1.0 p.u. threshold violations for any bus *extremely* close to the source which happens to sit on a branch. Although this may seem insignificant in this particular system, on a much

larger system, results could be much more negatively impactful.

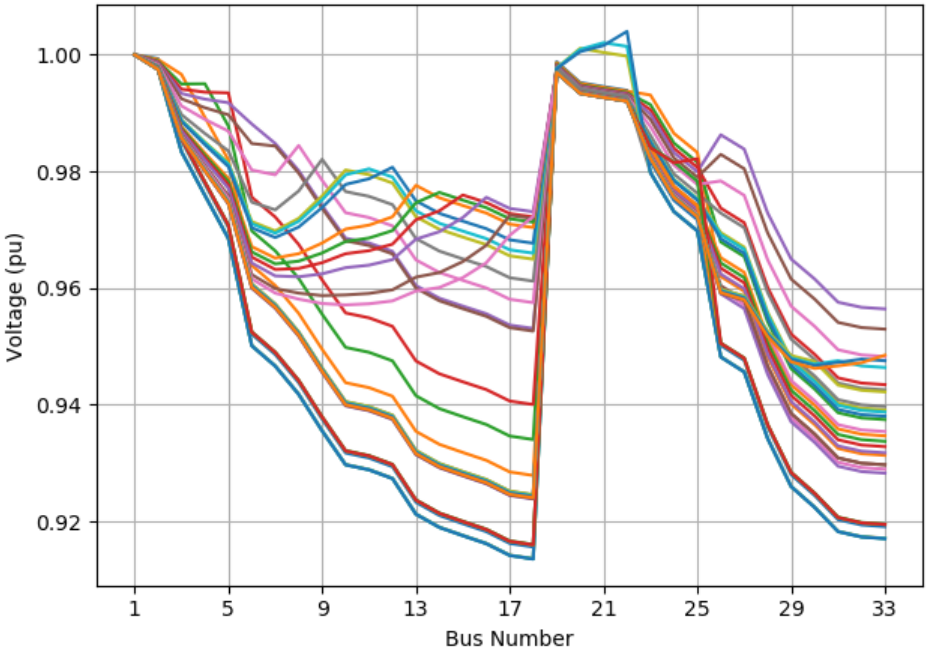

(a) Method I Voltage Profile(s)

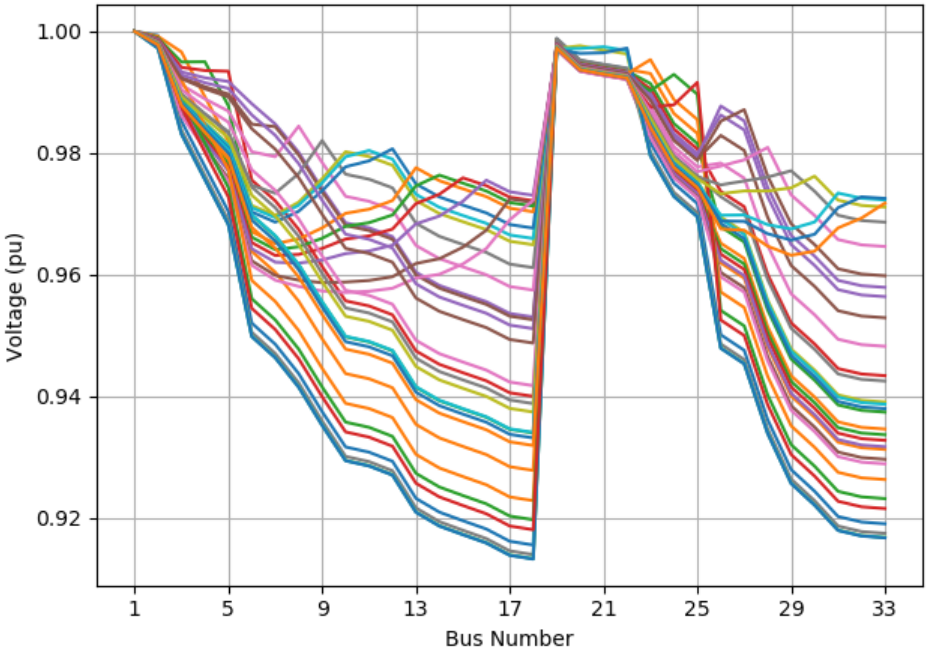

(b) Method II Voltage Profile(s)

Fig. 4.11: IMO PV Sizing Voltage Profile Comparison.

4.5.4 IEEE 33-Bus and 6-Bus Networks Optimized PV Sizing and Placement Power Flow Simulations

It has already been determined that bus 5 in the 6-bus system is the critical PV location identified from using a $P_{PVK} = 0.09336$ MW from step 4. In addition, the bus closest to violation of the system profile constraint of 1 ± 0.05 p.u. is bus 6. Therefore, this location will be used for voltage improvement from step 5. It is also noted that due to the small size of this system and close proximity between buses 5 and 6, this multiple PV allocation will use the determined P_{PVK} from bus 5 shared between the two buses, thus allowing for a combination of *two* solar PV to be implemented for testing simultaneously.

Continuing with step 4 from the *Method Two* results for the 33-bus system, buses 6 and 7 on the main feeder and bus 26 on the last branch exhibit minimal power loss according to Fig. 4.10. The result from step 3 is a P_{PVK} value of 2.473 MW, which will be used for power loss improvement. By examining Fig. 4.7, bus 18 is closest to violating the system profile constraint with a magnitude of 0.913 p.u., followed by bus 33 at 0.916 p.u. This is typical on a single source radial distribution system as location(s) furthest from the source experience a higher level of voltage deviation [55].

The result from step 5 is a P_{PVK} value of 1.473 MW, which will be used for voltage profile improvement. From [57], it has been shown that these locations exhibit a larger sensitivity to PV implementation, making higher penetration levels at these locations a larger risk when considering future load growth models. To prevent over-voltages, this PV size is reduced by half to 0.737 MW for simulation.

A trial simulation is constructed for multi solar PV analysis on the 6-bus system and the IEEE 33 bus radial system, using various combinations of the selected PV sizes at the critical locations. Again, because the smaller network has no branches and is used for validation purposes, a smaller combination of selected grid-connected PV is used. Each combination is varied using scaled ten percent values of the derived sizes

to identify the optimal combination of grid-connected PV for use on the main feeder and/or branch support. Tables for each combination trial are listed below.

Table 4.4: PV Sizing Trials 6 Bus System

PV Sizing Bus 5 and 6		
Case	Bus 5 PV [MW]	Bus 6 PV [MW]
1	0.09336	0.00000
2	0.08402	0.00934
3	0.07469	0.01867
4	0.06535	0.02801
5	0.05602	0.03734
6	0.04668	0.04668
7	0.03734	0.05602
8	0.02801	0.06535
9	0.01867	0.07469
10	0.00934	0.08402
11	0.00000	0.09336

Table 4.5: PV Sizing Trials 33 Bus System

PV Sizing Per Bus [MW]				
Trial	Bus 6	Bus 18	Bus 26	Bus 33
1	2.473	0.736	0.0	0.0
2	2.226	0.663	0.247	0.074
3	1.979	0.589	0.495	0.147
4	1.731	0.515	0.742	0.221
5	1.484	0.442	0.989	0.295
6	1.237	0.368	1.237	0.368
7	0.989	0.295	1.484	0.442
8	0.742	0.221	1.731	0.515
9	0.495	0.147	1.979	0.589
10	0.247	0.074	2.226	0.663
11	0.0	0.0	2.473	0.736

Each combination of solar PV sizing per bus is applied to the system and a power flow is conducted per trial. Both simulations provide unique circumstances with various amounts of power injection throughout the network simultaneously, as opposed to a singular PV injection at only one location as the IMO was originally intended. The 6-bus system will receive penetration at two locations, while the 33-bus system will receive the injected solar PV at four locations. This experiment will allow for maximum

penetration to occur on the main feeder only in *Trial 1* and maximum penetration on the branches in *Trial 11*. Meanwhile, *Trial 6* will distribute PV over the four bus locations in relatively equal quantities.

4.5.5 6-Bus and IEEE 33-Bus Results

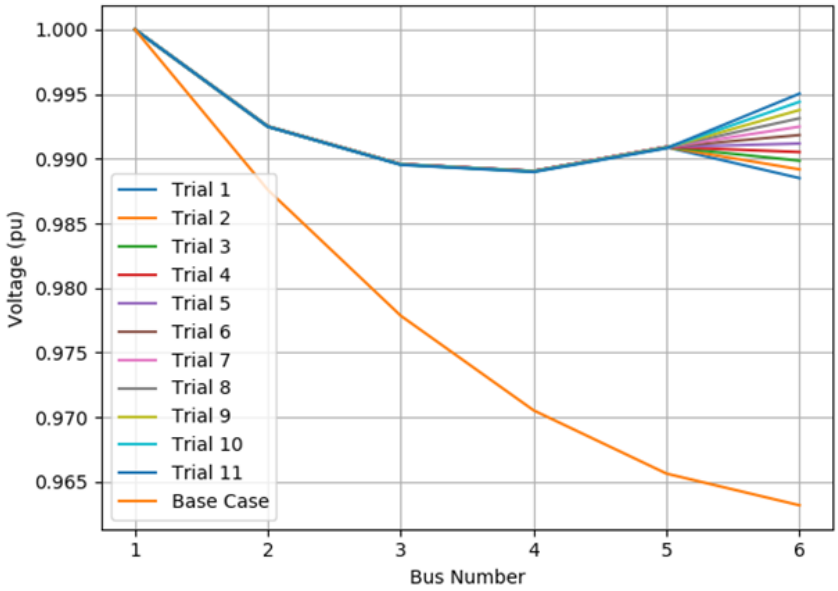

Fig. 4.12: PV Sizing Trials Voltage Profiles 6-Bus System

.

Table 4.6: PV Trial Results Active Power Loss 6-Bus System

Active Power Loss Reduction		
Trial	Active Power Loss kW	Base Case Reduction%
Base	6.759	0.0
1	1.239	82.0
2	1.136	83.1
3	1.072	83.8
4	1.045	85.1
5	1.055	84.0
6	1.104	83.7
7	1.189	82.2
8	1.312	81.0
9	1.472	78.4
10	1.668	75.3
11	1.902	72.0

Data from the 6-bus simulation confirms an excellent improvement in active power loss reduction and voltage profile improvement using an optimal PV pairing size of 0.065 MW on bus 5 and 0.028 MW on bus 6 in Trial 4, compensating base case losses by approximately 85%. The voltage profile is also improved as is seen in Fig. 4.12 for *all* buses in the network, with an average bus voltage above 0.99 p.u. These results show the positive impact of PV injection furthest from the source in a radial feeder with no branches. However, it must be noted that this system is small and unrealistic in nature compared to much larger modern smart feeders. Additionally, because the PV in this simulation are located adjacent to one another, it could be viewed as a singular PV penetration on a larger scale. Nonetheless, the improvement of bus voltage and line loss reduction are evident.

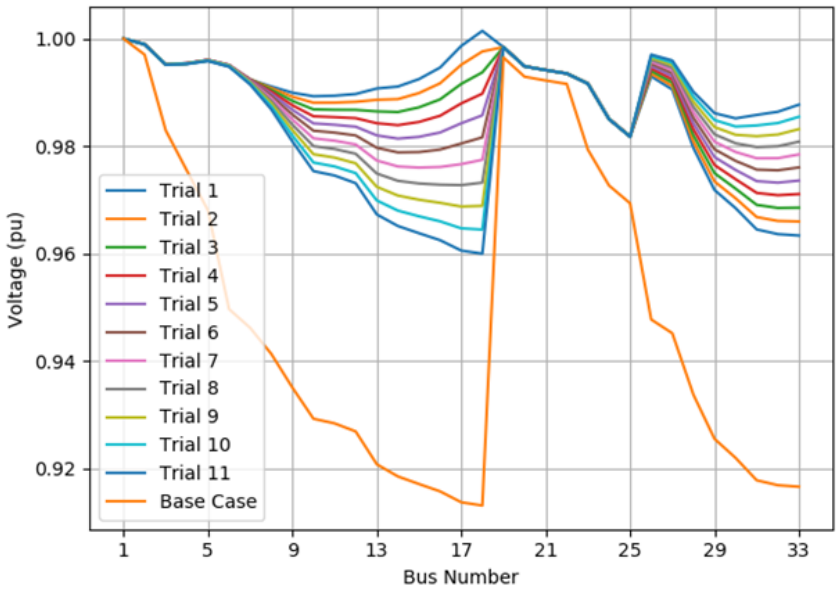

Fig. 4.13: PV Sizing Trials Voltage Profiles IEEE 33-Bus System

.

The results of the 33-bus simulation show that a total of four PVs in various combinations along the critical bus locations may be used via the IMO to compensate for power loss and voltage profile improvement. All cases display significant improvement over the base case scenario, with an average active power loss of 94.5 kW and an average voltage profile of 0.984 p.u. The optimal proper P_{PVK} sizing shared between buses in

Trial 6 produces a maximum active power loss reduction of 56.43%, a maximum reactive power loss reduction of 53.9% and an average system voltage profile of 0.989 p.u using an evenly distributed PV output of 1.237 MW at buses 6 and 26 and 0.368 MW at buses 18 and 33. This is the ideal scenario which offers the most beneficial trade-off between voltage deviation compensation and reduced losses, without compromising nodal hosting capacity. This is evident in Tables 4.7 and 4.8.

In Trial 1, all PV is concentrated on buses 6 and 26, yielding active loss reduction at 49.4% and an improved system voltage profile along the main feeder, yet little compensation is offered to the remaining branches. Conversely, in Trial 11 where all PV is concentrated on buses 18 and 33 furthest from the source, loss reduction is nearly identical and the profile is improved along buses 19-33, yet weaker along the main feeder. This trade-off is observed in Fig. 4.13.

It should also be noted that by adjusting the PV location for bus 26 to bus 25 produced active power loss reductions of up to 65%, yet due to the distance of bus 25 to the source, several cases of extreme over-voltages were reported.

Table 4.7: PV Trial Results Active Power IEEE 33-Bus System

Active Power Loss Reduction		
Trial	Active Power Loss kW	Base Case Reduction%
Base	202.677	0.0
1	102.553	49.4
2	97.279	52.0
3	93.211	54.01
4	90.354	55.42
5	88.715	56.23
6	88.3	56.43
7	89.120	56.03
8	91.185	55.01
9	94.508	53.37
10	99.101	51.1
11	104.982	48.2

Table 4.8: PV Trial Results Reactive Power IEEE 33-Bus System

Reactive Power Loss Reduction		
Trial	Reactive Power Loss kVAR	Base Case Reduction%
Base	135.141	0.0
1	74.192	45.0
2	69.890	48.3
3	66.542	50.8
4	64.151	52.5
5	62.725	53.6
6	62.270	53.9
7	62.794	53.5
8	64.308	52.4
9	66.821	50.6
10	70.346	47.9
11	74.896	44.6

By comparison, the multi-solar allocation results on the IEEE 33-bus system using various combinations of PV are compared to results using a *single* grid-connected PV at the minimal active power loss location (bus 6). This method uses the original design of the IMO which was meant for optimization of a single PV only for loss reduction and voltage profile improvement. After performing an iterative load flow and calculating power loss reduction using only a single PV of equal size $P_{PVK} = 2.473$ MW at bus 6, the power flow results prove that the proposed multi-solar technique provides a greater benefit to the overall network.

Although the voltage profile of the network is improved in Fig. 4.14, the magnitude of improvement is much less significant compared to the multi-solar trials. The voltages at buses furthest from the source still exhibit undervoltages and the branches are not adequately benefited from this integration. Similarly, active power losses are reduced in the 33-bus network to 104.11 kW, a base case reduction of 48.55%. This is also not as significant an improvement as Trials 3-9 of the multi-solar allocation, which saw its greatest improvement in Trial 6, with an active power loss of 88.3 kW, a reduction from the base case by 56.4%.

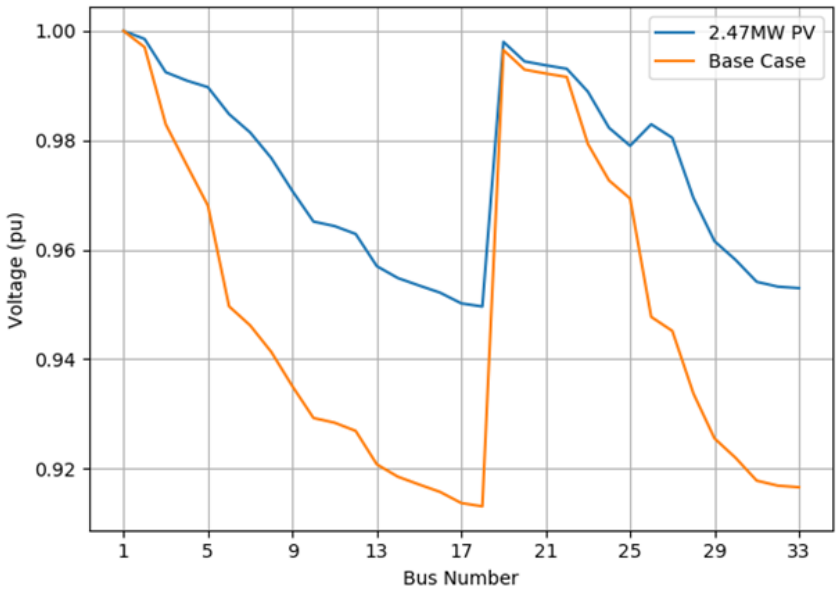

Fig. 4.14: PV Sizing using Singular PV at Bus 6 IEEE 33-Bus System

.

Table 4.9: Single VS. Multiple PV Integration Comparison IEEE 33-Bus System

IMO PV Sizing with losses			
Bus	PV Quantity	$P_L[kW]$	Base Case Reduction %
6	1	104.110	48.6
6,18,26,33	4	88.3	56.4

4.6 Voltage Deviation Correction

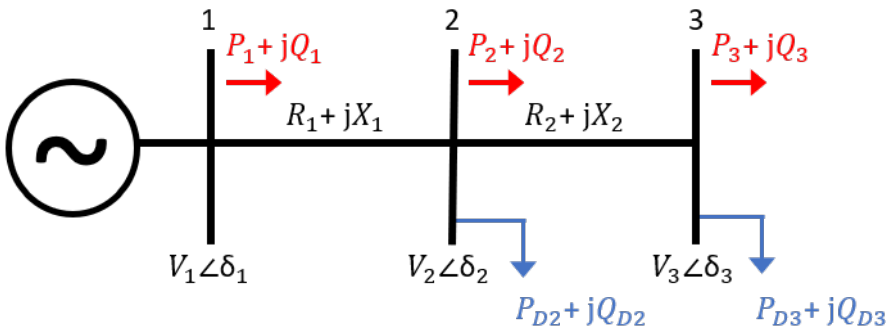

Fig. 4.15: 3-Bus Radial Distribution Feeder Single Line Diagram

Although the results of the multi-solar allocation optimization proved effective, a significant correction to the voltage deviation approximation of the IMO must be stated. In this section, the correction is discussed, along with the importance of recognizing

how the inclusion of such parameters will impact the optimization process of solar PV integration. Here, a proper mathematical correction using voltages in complete phasor form is used to compare results of the multi-solar PV allocation on the IEEE 33-Bus system.

The flow of power in a radial distribution feeder from bus i to bus $i+1$ is given in red across the line (branch) with a specific impedance $Z = R + jX$ as discussed at the beginning of this chapter. Fig. 4.15 shows the voltages in true phasor form at each bus location with a given magnitude and phase angle. The loads on buses 2 and 3 represented in blue designate power absorbed from local demand at each bus. From [30], the proposed voltage deviation model is given as follows from 4.11:

$$VD^2 = \sum_{i=1}^{n} \frac{(R_i P_i + X_i Q_i)^2}{|V_{i+1}|^2}$$

where the real and reactive powers and line properties of the *ith* bus (or line between buses) are taken over the voltage magnitude of the following bus $i+1$. However, this formula does not include the complete load power model which accounts for true voltage deviation between consecutive buses (real and imaginary portions). Therefore, a correction is proposed to improve the accuracy of the IMO in relation to the voltage deviation index, or ratio of voltage difference between consecutive buses with and without a locally grid-connected solar PV.

In any distribution system topology, the per unit voltages of the buses are subject to the nominal 1 ± 0.05 p.u. requirement to achieve adequate system stability. In a radial feeder, those buses nearest to the point of generation (slack bus) typically adhere to this standard due to close proximity to the source. However, areas at the end of the feeder further away from the slack bus will suffer from undervoltage conditions in which the nodal voltage may dip extremely low beyond the desired voltage magnitude required for system sustainability and require additional power compensation to improve the

performance of the overall network.

Initially, the system is designed to support the peak demand with anticipation of estimated load growth over a certain block of time. However, this affect is enhanced with growing load banks, EV charging stations, and increasing residential demand from the time the distribution feeder is constructed throughout its lifetime. As lines become slowly overloaded over time, nodal voltage sags can worsen, leading to system instability and overload. Fortunately, this consequence offers great opportunity for locally injected solar PV to provide voltage compensation in these weakened areas of the feeder through optimized injected power.

The flow of power from bus to bus in a radial feeder is modeled using the voltage and current in phasor form given as $\bar{S} = \bar{V}\bar{I}^*$. Ultimately, this means that the true power flow is dependent on both the magnitude and angle of the given parameters. By expanding on this power flow model, it can be proven that the difference between nodal voltages in true phasor form are composed of both real and reactive components. This derivation is followed by a simulation example for comparison with the previous section's results on the IEEE 33-Bus System.

First, Ohm's law is used to replace the current phasor to describe the relationship between power at each bus. The derivation is taken from the perspective of incoming power to the *ith* bus.

$$\bar{S} = P_i + jQ_i = \bar{V}_{i+1}\bar{I}_i^* \tag{4.26}$$

Solving for current, removing the complex conjugate,

$$\bar{I} = \left[\frac{\bar{P}_i - j\bar{Q}_i}{\bar{V}_{i+1}}\right]$$

Therefore, from *Ohm's Law*,

$$\bar{V}_{i+1}\bar{I}_i^* = \bar{V}_{i+1}\left[\frac{\bar{V}_i - \bar{V}_{i+1}}{R_i + jX_i}\right]^* = (P_2 + jQ_2) + (P_{D2} + jQ_{D2})$$

$$= (P_2 + P_{D2}) + j(Q_2 + jQ_{D2})$$

Let $\bar{V}_{i+1} = \bar{V}_2$ and combine terms,

$$\bar{V}_2^*\left[\frac{\bar{V}_1 - \bar{V}_2}{R_1 + jX_1}\right] = (P_2 + P_{D2}) - j(Q_2 + Q_{D2}) \tag{4.27}$$

Thus, the difference in voltage deviation between buses using the true phasor form is,

$$\bar{V}_1 - \bar{V}_2 = \frac{(R_1 + jX_1)\left[(P_2 + P_{D2}) - j(Q_2 + Q_{D2})\right]}{\bar{V}_2^*} \tag{4.28}$$

Expanding 4.28 to show real and imaginary components,

$$= \frac{[R_1(P_2 + P_{D2}) + X_1(Q_2 + Q_{D2})]}{\bar{V}_2^*} + j\frac{[X_1(P_2 + P_{D2}) - R_1(Q_2 + Q_{D2})]}{\bar{V}_2^*}$$

It is clear to see that the true voltage deviation between nodal buses using the phasor form of each voltage results in a real and imaginary portion. To obtain the formula from equation 4.11 used in the IMO, the magnitude of this difference is taken so that only the real portion is accounted for, thus neglecting the imaginary portion of the derived equation.

$$\left|\bar{V}_1 - \bar{V}_2\right| = \frac{[R_1(P_2 + P_{D2}) + X_1(Q_2 + Q_{D2})]}{V_2} \tag{4.29}$$

Squaring both sides and substituting for the *ith* bus yields the real portion of voltage magnitude only.

$$\left|\bar{V}_i - \bar{V}_{i+1}\right|^2 = \left[\frac{\left[R_i(P_{i+1} + P_{D_{i+1}}) + X_i(Q_{i+1} + Q_{D_{i+1}})\right]}{V_{i+1}}\right]^2 \tag{4.30}$$

Thus, the load power must be considered using both the *real* and *imaginary* portions of the relative bus voltage difference. It has been shown in previous studies that the effect of load increases can change the predicted optimal value in real time as distribution feeders expand. The results of using the true phasor form of voltage deviation in the simulation reflect *improved* accuracy in PV sizing and drastically improved voltage deviation during the trial, while losses are still adequately minimized. After implementation of this correction in the IMO and calculating the P_{PVK} minimal size for optimal PV at each bus location, results show an overall *increase* in PV sizing using the *Method Two* sizing model.

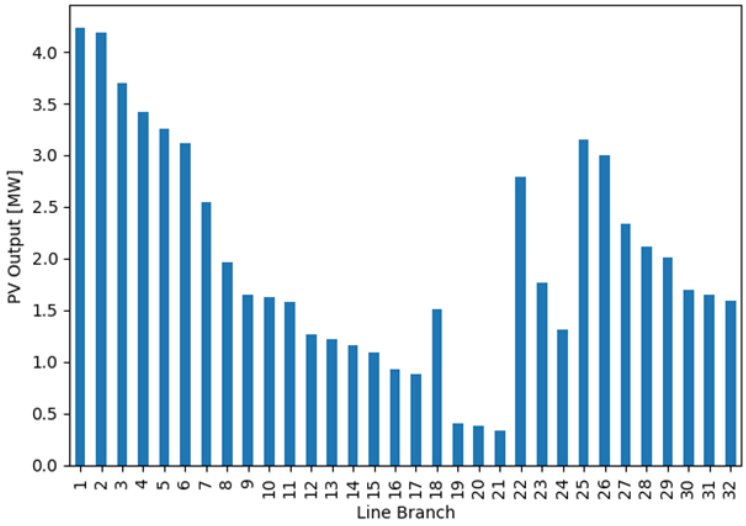

Fig. 4.16: PV Sizing Trial using True Phasor Voltage Deviation

.

As observed in Fig 4.16 the resulting difference in sizing per bus is determined by both the magnitude *and* angle of the bus voltages. This correction is significant in relation to the IMO voltage deviation index in that it *raises* the calculated P_{PVK} magnitude at each bus location in the system by a range of 0.02 - 0.65 MW across the resulting optimal solution set compared to the determined PV sizes using the

absolute value voltage difference squared for magnitude. This means that the overall penetration levels of the multi-solar allocation will be higher when compared to the original results, which ignored the *imaginary* portion of the true voltage deviation phasor.

After executing an iterative load flow using the IMO at each bus and examining the active power losses, the same buses which were previously identified in the study are determined as critical locations for a grid-connected solar PV placement of the calculated size. This is expected as the line and load properties of the system remain the same. Again, minimal power loss is identified at buses 6 and 26, and voltage profile improvement compensation at buses 18 and 33 (furthest from the source). Corresponding P_{PVK} sizes used for the given case study are determined to be 3.111 MW (bus 6) and 1.516 MW (bus 18), which are larger than the sizes used previously. Similar to the original study, this value at bus 18 is reduced in half to 0.758MW to reduce voltage constraint violations from oversensitive locations further away from the source [57].

The similar multi-case trial simulation is repeated in a similar manner on the IEEE 33-bus system using the updated solar PV sizes in combination across the same four buses used in the original study for comparison.

Table 4.10: PV Sizing Trials Voltage Deviation Correction

PV Sizing Per Bus [MW]				
Trial	Bus 6	Bus 18	Bus 26	Bus 33
1	3.111	0.758	0.0	0.0
2	2.8	0.682	0.311	0.076
3	2.489	0.606	0.622	0.152
4	2.178	0.531	0.933	0.227
5	1.867	0.455	1.244	0.303
6	1.556	0.379	1.556	0.379
7	1.244	0.303	1.867	0.455
8	0.933	0.227	2.178	0.531
9	0.622	0.152	2.489	0.606
10	0.311	0.076	2.8	0.682
11	0.0	0.0	3.111	0.758

The various case studies are simulated again one at a time to determine the best combination of PV which reduces power losses and improves the voltage profile of the system. It is clear to see from Fig. 4.17 that the overall voltage profile of the 33-bus system is *increased*, resulting in an average bus voltage magnitude of 0.992 p.u, a significant improvement over the original results across all buses of the network.

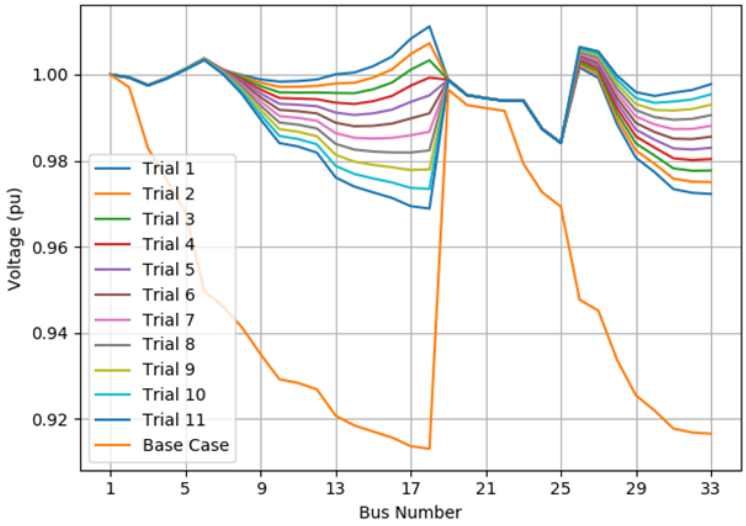

Fig. 4.17: Voltage Profile Comparison using true phasor voltage deviation

.

The voltage deviation results per trial are shown below in Table 4.11. It is important to observe that regardless of the size combination of solar PV used, base case reduction percentages topped 80% in *every* trial. Overall, the voltage deviation using the derived formula delivered an average voltage reduction of 83.63% from the base case, an increase over the original results using equation 4.11 by 26.2%.

The largest reduction occurs in trial 4, using a larger PV size on bus 6 with smaller sizes located at buses 18, 26 and 33. This data suggests that the system voltage is perhaps better regulated (in this case) using a *single* larger grid-connected PV located at any local bus k subject to $P_L(min)$ along the main distribution feeder, in combination with multiple smaller localized grid-connected PV positioned along the T-branches of a radial network at V_{bus_k} using the constraint 1 ± 0.05 p.u. to compensate for voltage dips and sagging due to overload.

Table 4.11: PV Trial Results Voltage Deviation Correction

Voltage Deviation Reduction [kV]		
Trial	Voltage Deviation [kV]	Base Case Reduction%
Base	58.687	0.0
1	11.074	81.13
2	9.682	83.5
3	8.929	84.79
4	8.676	85.22
5	8.728	85.13
6	8.919	84.8
7	9.149	84.41
8	9.402	83.98
9	9.731	83.42
10	10.256	82.52
11	11.137	81.02

Additionally, the active power loss reduction observed in each trial is shown in Table 4.12 below. Overall losses are noted to be slightly *lower* (average reduction of 44.17%) when compared to results from the first study, which showed an average reduction of 53.38% compared to the base case. This difference is best explained by the drop in magnitude of solar PV penetration at each bus. When both the voltage magnitude and previously ignored phase angle are considered, the IMO produces a *larger* array of PV sizes. When only the real portion of the phasor is used and the load angle is not considered, the IMO outputs *lower* sizes at all buses in the network. This contrasting result clearly demonstrates that higher penetration levels in a radial distribution feeder will have a greater impact on voltage profile improvement while loss reduction is slightly sacrificed. On the contrary, lower penetration levels may improve overall power loss reduction, but do not improve the system bus voltage profile sag to the same degree.

In conclusion, by using the magnitude and phase angle of the voltage phasor to determine the voltage deviation index portion of the IMO, the system voltage profile is significantly improved from both the base case and the main study which ignores the real portion of the phasor in Section 4.5. This introduction of the true voltage phasor results in an increase in PV sizing, which accurately accounts for both the real

Table 4.12: PV Trial Results Active Power Loss Comparison

Active Power Loss Reduction		
Trial	Active Power Loss [kW]	Base Case Reduction%
Base	202.677	0.0
1	120.378	40.61
2	114.895	43.31
3	110.747	45.36
4	107.937	46.75
5	106.470	47.47
6	106.354	47.53
7	107.598	46.91
8	110.212	45.62
9	114.210	43.65
10	119.604	40.99
11	126.411	37.63

and reactive portions of power flow at any given bus location. As discussed earlier in the chapter from [58], limiting line losses is equally dependent on active and reactive power components.

Therefore, to accurately forecast load demand and size PV accordingly, means to include the complete powers at all locations. Although this improvement comes with a small sacrifice of power loss reduction during the multi-solar allocation process, the striking bus voltage improvement leads to an alternative approach to the IMO which suggests use of a combination of a single large PV located along the main feeder of a radial system to compensate power losses, with multiple smaller sized PV introduced at locations furthest away from the source on branches of the network to greatly improve bus voltages.

4.7 Conclusion

In conclusion, the IMO may be successfully used to properly optimize smart grid-connected solar PV at multiple location(s) in a single source radial distribution system. The data gathered in this study validates the sizing model correction and affirms a

method by which multiple solar PV can provide a greater benefit to the distribution feeder in regards to loss reduction and bus voltage. When undergoing implementation of solar PV on an existing distribution grid, the IMO allows for various combinations of PV to be tested using proper sizing techniques and the improved method based on location in the system. These various combinations provide a unique balancing scheme which offers multiple solutions to a set of common power system objectives, namely, power active and reactive power loss and voltage deviation. In this case, the most efficient PV integration which provided the best combination of power loss reduction and voltage profile improvement included an even distribution of PV at the critical locations as opposed to a single highly concentrated area of PV.

The improvement of the voltage deviation index equations also provides insight into the importance of considering both real and reactive properties to optimize DG in a radial distribution feeder. The proposed algorithm has a greater generality to branched radial distribution feeders for improved accuracy in the optimization. Prior methods ignored this and it was shown that it makes s significant difference if considered in the algorithm during planning for integration of properly sized and placed solar PV.

To achieve regulated line and bus voltages, optimized PV may be used in areas of undervoltage to reduce power losses, however the level of PV penetration must be carefully determined to avoid a hosting capacity violation. This is especially concerning during low demand hours with peak solar output. On the contrary, reducing the amount of solar penetration will help prevent voltage spikes, however, line losses will be higher in this regard. This proposed solution provides an expandable approach to sizing and placement on a multi-branch system using a sizing model which allows for adequate DG overhead in a multi-branch network, and accounts for projected growth expansion in modern smart grid networks.

The next two chapters discuss future research direction for this work using modern machine learning and deep learning techniques. Time based profiles are developed and

examined for various 24-hour solar PV models and load types for an even closer look at time series behavior. Finally, newly developed research area is covered using deep learning models to conduct power systems analysis.

CHAPTER 5

Volatile Solar PV Pattern Analysis and Distribution Feeder Hosting Capacity Impacts

5.1 Time Series PV Profile Development

A major part of solar PV integration data analysis involves dynamic model development to accurately incorporate variable generation data into a power flow. Time series data captured by smart meters and demand side monitoring devices provides utilities with accurate solar irradiance models to enable proper distribution level DER planning. This data can be used to develop forecasting models and provides hosting capacity (HC) information critical to successful PV integration relative to specific time intervals throughout the day [61].

The output power of solar PV is heavily dependent on weather conditions and the physical solar panel surface exposure percentage to available sunlight. During clear sunny days, solar PV units potentially produce maximum power output as opposed to zero output at night. Most profile models show peak power absorption and output when the sun is directly over the PV arrays with no visible interference in the middle of the day, usually around early afternoon. These levels follow a typical Guassian distribution with PV output levels rising with the sun in the morning hours and lowering as the sun sets.

Basic normally distributed PV profile curves, however, do not accurately mimic the behavior of true output patterns. Intermittent cloud cover and events such as thunderstorms and snowstorms, can cause the grid-connected PV systems to produce rapid fluctuation in power output at a much faster rate compared to demand curve changes on a smaller scale throughout any given day. In cloudy weather (which is common in

many geographical areas where distributed level solar PV is installed) this behavior due to variable irradiance level exposure can cause significant drops in power output up to 70% [62]. It is for this reason that the nodal HC can become compromised due to voltage regulation violations suffered from variable generation. Consequently, geographical information systems (GIS) models and smart meter data serve as accurate tools to provide realistic PV model behavior.

The next section describes the development of time based profiles for solar PV and commercial loads for testing in a DER integrated medium distribution feeder.

5.1.1 27 MW Solar PV Plant Profile Modeling

In order to further analyze the impact of variable DER behavior at a distribution level, data is collected from a solar PV generation plant in central Texas from the National Renewable Energy Laboratory (NREL). The data set contains solar PV output power recorded over a full annual cycle from a 27 MW distributed PV station collected from 2006-2007 and available for public access at [63]. The data is organized into a time series form using a t_{step} of 5 minutes between recorded measurements. After some basic data pre-processing, various monthly patterns of solar PV output are collected and plotted on an identical 24-hour time axis for comparison.

It is clear to see from Fig. 5.1 that the solar plant starts outputting power just after sunrise, peaks around midday, and returns to zero when the sun sets in the evening. Even more noticeable are the various transients and erratic behavior of the solar PV output throughout the day. Rapid rises and falls during the daytime indicate moving cloud cover or possible thunderstorms on a sunny summer day in central Texas. The continuous sudden changes in PV power can directly impact grid voltage regulations and frequency stability management on the utility side, if not properly managed.

Similarly, in Fig. 5.2, four randomly selected days in four randomly selected months are compared on a similar axis of time. Weather patterns become more relevant here to

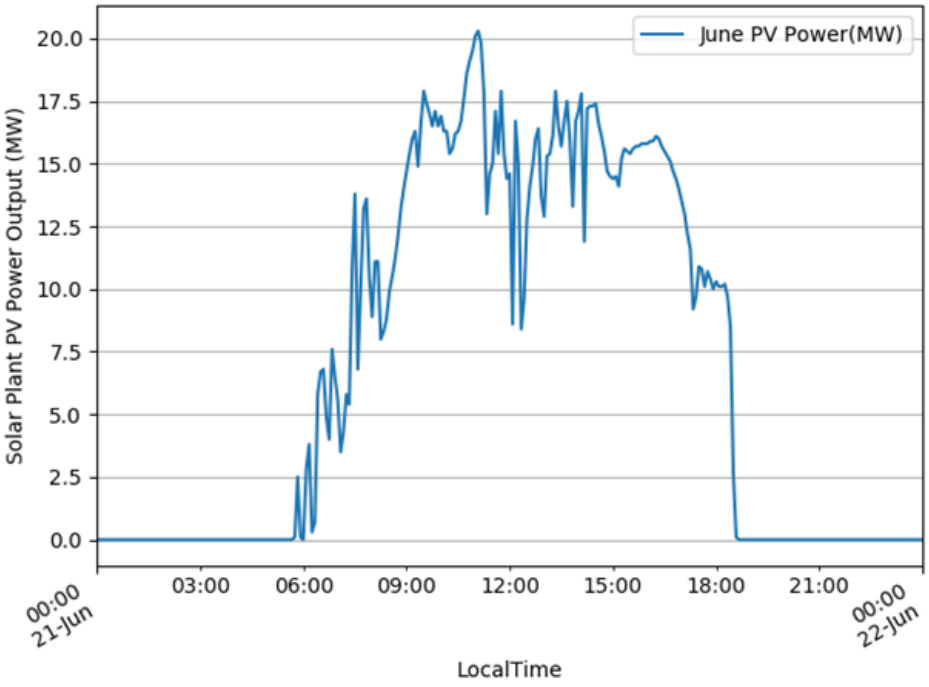

Fig. 5.1: June 21st 2006 PV Profile Irradiance Model 27 MW Solar Plant

.

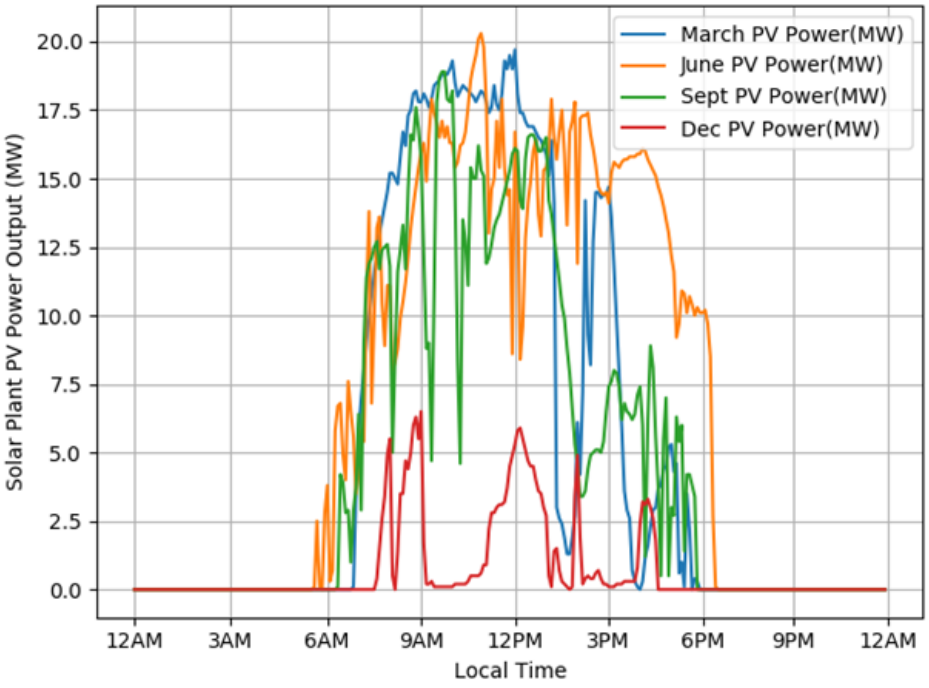

Fig. 5.2: Seasonal 2006 PV Profile Irradiance Comparison 27 MW Solar Plant

.

distinguish the available sunlight during a particular time of the year. Clearly, annual power generation is much lower in the winter months and picks back up in the Spring and Summer. Again, severe drops in power output during March and September demonstrate the importance of understanding the inconsistencies of renewable generation. In some periods throughout the day, there is little disruption to the system and in others, there is an extreme amount. Nonetheless, the intermittent behavior of the solar generation is consistent across all data collected.

5.1.2 Impact of Dynamic and Intermittent Solar PV Power on Distribution Feeder Voltage

Utilities must consider solar data for more accurate model forecasting in simultaneous studies with time based load curves when estimating precise HC limitations on distribution feeders. Various load type curves such as residential, commercial and industrial each have unique time series properties which provide vital information regarding peak demand magnitude during specific time intervals. Distribution planners and utilities rely on load data collected by smart devices to anticipate for distribution growth and classification of demand patterns to better support the grid. For example, a typical residential load curve will show a brief rise in demand in the morning as families prepare for work and school and an even larger rise after 6 PM when families are home and power consumption is at its maximum.

Various load curves from [63] are shown in 5.3 taken from an industrial plant in central Texas in a similar annual time series format. Certain data sets using larger time steps may require manipulation via interpolation prior to model deployment to reduce error in power flow simulations. Linear interpolation is used on the 15 minute interval load dataset to create a time series with 5 minute intervals. In this manner, both PV and load profiles contain equivalent numbers of samples within a 24-hour period and can be used simultaneously in network studies to more accurately model distribution network

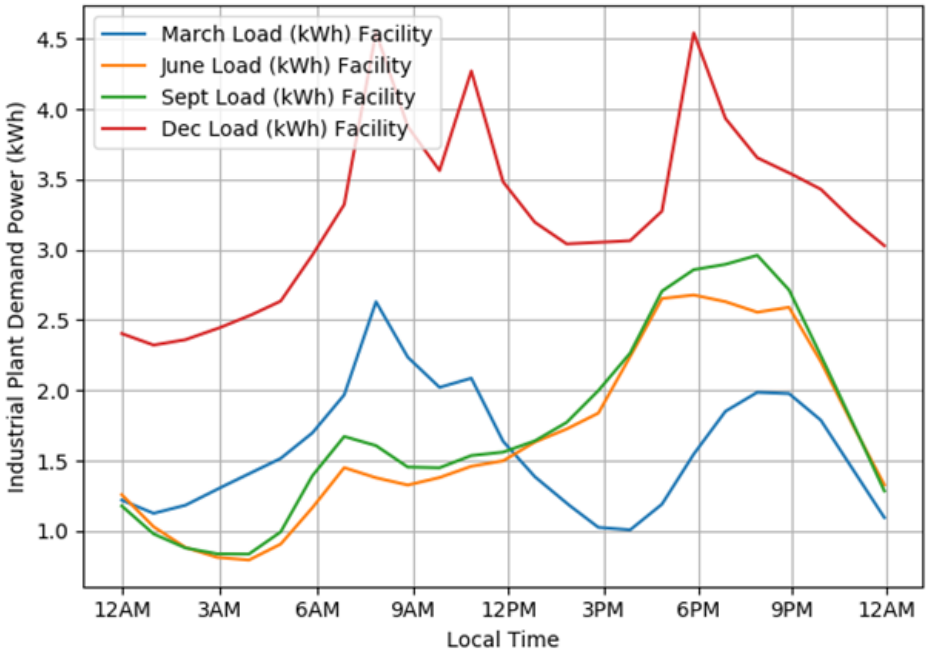

Fig. 5.3: Seasonal Load Curves 100kW Industrial Plant

.

behavior with DER integration.

5.1.3 20 kV CIGRE-Network Test System with Time Series Controller

Load and PV profiles can be implemented together in network simulations to allow for quasi-static time series analysis using iterative power flow techniques to simulate real time behavior. Reference [59] provides a time series-based controller module designed for time based operations which updates parameters of specified elements (loads, PV generation, wind generation, etc.) in loaded networks in each time step of a loop. Within the control loop, any given number of individual controllers can be added to control various elemental power generators or load banks using any number of data sources (PV or load profiles) for reference to the numerical adjustments every time step. An output writer is added to store iterative power flow results such as system voltage profile information and other load flow parameters into a separate .xlsx file.

A 15-bus 20 kV medium voltage distribution feeder CIGRE-Network from [59] is se-

lected for experimentation of the time series controller using the gathered load and solar profile curves (see Fig. 5.4). CIGRE-Networks are a set of developed systems to facilitate the continued analysis of DER integration for high voltage, medium voltage, and low voltage transmission and distribution systems. This extensive library contains various networks of differing grid topologies produced for the study of renewable integration. The 20 kV distribution network contains eight solar PV generation points and one wind generation point.

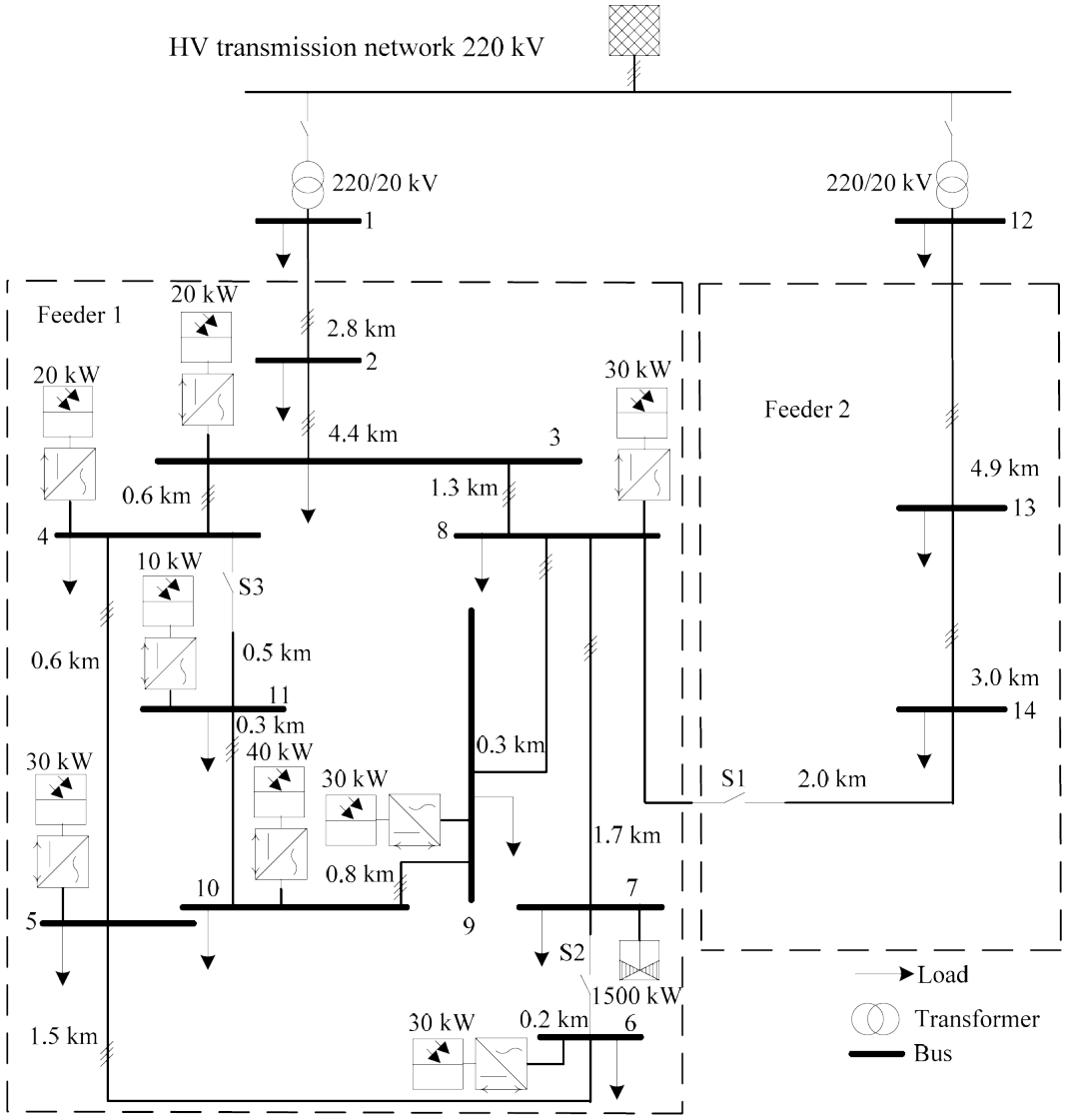

Fig. 5.4: 15-bus MV CIGRE-Network with DER

.

PV profiles gathered from the central Texas plant are converted and scaled to fit the distribution system PV peak powers, and used as static generator (sgen) control at buses 4, 5, 6, and 8. Only active power is injected at each sgen location, avoiding complex inverter reactive power compensation schemes. Similarly, load profiles from the industrial facility are converted and scaled to fit four of the network loads and used as load controllers on buses 7, 9, 10, and 13. The 5 minute time series data allows for 289 total iterative steps (including the initial sequence) in a 24-hour window within the control loop in which a power flow is performed using the profile data for power control. Results of the calculated bus voltages and load powers per iteration are collected and stored for review.

Preliminary results from the controller simulation via the on board output writer yields independent time series data sets of the bus voltages in p.u. per iteration (load power not shown). The voltage profiles of buses 4-12 are examined for line limit violations and 24-hour behavior using the generated load and solar PV profiles to model realistic power output during daily operation. The remaining buses were not adjusted from the preset load and sgen values. It should also be noted that these profiles were selected at random and the data collected from the central Texas datasets was not designed for integration with this particular 20 kW network.

At first, only the PV profiles are used in the controller in Fig. 5.6, and the resulting bus voltages from Feeder 1 are shown. As expected, improvement during the daylight hours is noticeable and shows some improvement over the static case in Fig. 5.5 (taken at a single instant in time using quasi static time based power flow with no control). When both the load and solar PV curves are used with a total of 8 controllers in Fig. 5.7, the bus voltages experience limit violations by dropping below the regulation standard of 1 ± 0.05 p.u. due to overload. As expected, the largest voltage violation occurs around 6 P.M. at peak load and minimum solar PV power output.

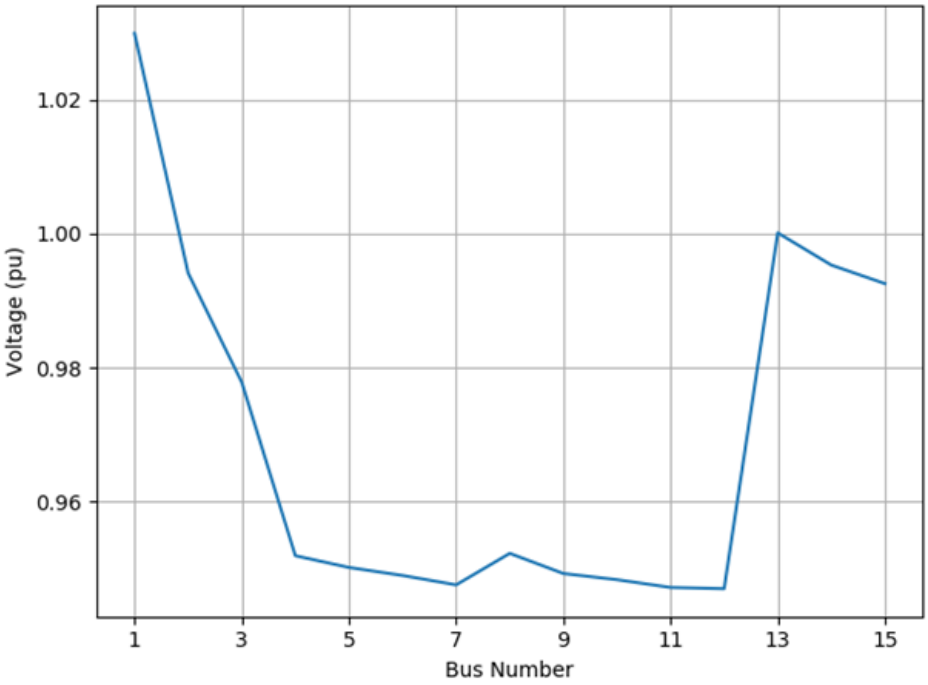

Fig. 5.5: CIGRE-Network Static Case Voltage Profile

.

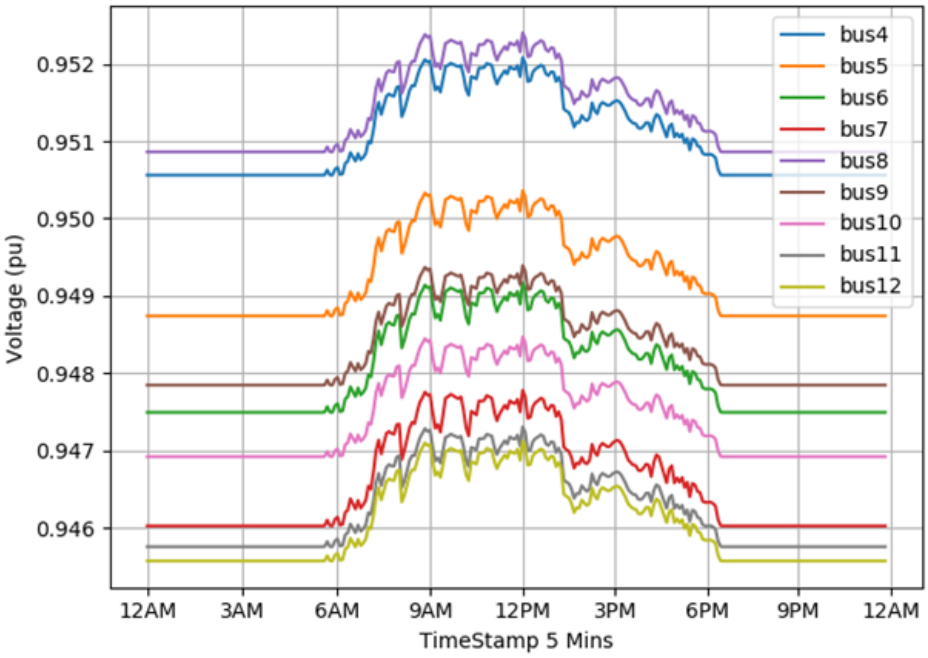

Fig. 5.6: 15-bus Network PV control on buses 4, 5, 6, and 8 - voltage profiles

.

In conclusion, time series analysis can provide a deeper insight to the behaviors of solar PV integration at target time intervals throughout the day. While steady state

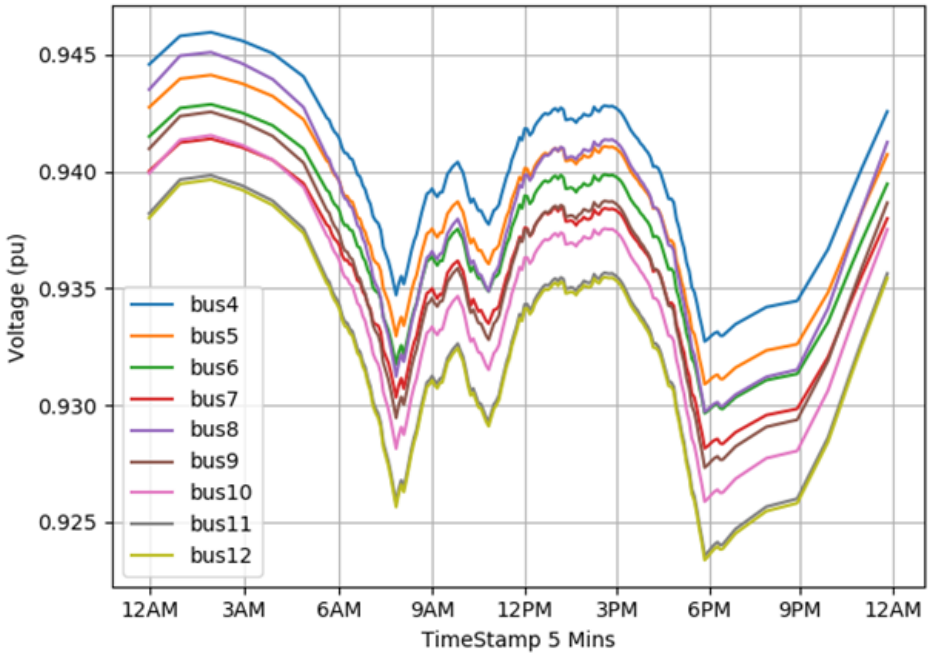

Fig. 5.7: 15-bus Network Load and PV Control buses 4-6, 8 - voltage profiles

.

power flow results do provide critical information regarding grid performance when integrating DERs, the time-based power fluctuations produced by solar PV require more studies at specific instances during daily operation. More importantly, the variability of solar PV requires dynamic time based modeling for improved integration studies compared to traditional static steady state models.

The time series controller from [59] contains many more adjustable features not discussed in this work which must take time to properly develop on larger systems, such as dynamic reactive power injection mimicking inverter side control on local PV units. Continued research involves developing these models with higher accuracy to improve prediction models for power system stability and load growth management.

The next chapter discusses analysis of a deep learning data structure platform used for creating learning models which operate using feature extraction to solve complex non-linear relationships.

CHAPTER 6

An Improved Power System Analysis Approach Using Tensor-based Analytics

6.1 Power Systems Analysis using Pytorch

6.1.1 Non-Linear DER Behavior and Power System Stability

As discussed throughout this work, DERs such as solar PV and wind turbines have become a vital option in combating the increasing demand in power systems distribution. The absence of harmful emissions and limitless driving supply for this technology provides advantages in long term market cost and field deployment. However, the variable nature of these resources creates the need for models which can better optimize renewable systems by dealing with their unpredictable dynamic behavior. This chapter describes some preliminary notions of applying tensor-based analytics to solving power system load flow-type problems using Pytorch. This section aims to provide remarks on its suitability to a much wider range of power-flow-based optimization problems which could lead to improved system planning and better computational efficiency for larger systems.

Power system stability is a key factor for utilities involved in maintaining a resilient distribution grid with continuously integrated renewable resources. Non-linear modeling is required for DERs which produce a highly fluctuating power output. For example, the solar PV power output is dependent on several factors such as climate, load, array temperature, solar irradiance percentages, etc. These relationships create a non-linear operating characteristic [64] and significantly affect the steady state and dynamic performance of the power system.

Inherently, there is a need for improved model development and analysis techniques to accurately simulate, predict and rapidly account for changes within the system in real time operation. The development of AI based algorithms which "learn" system behavior and response based on data inputs have become more desirable due to their flexibility and run time. Unfortunately, practical implementation of these models remains scarce and many proposed methods which seem promising in simulation do not survive in realistic application.

6.1.2 Understanding Pytorch and the Fundamental Tensor

Traditional ML models used in power systems analysis require massive amounts of static data to train on specific features used in classification algorithms for supervised learning. Over the last decade, demand for graph theory based computational frameworks is in high demand, thus Deep Learning (DL) models are being used across a wide variety of scientific research platforms to solve complex problems [65]. One of the most recent developmental frameworks proposed to build DL models and neural networks is *Pytorch*.

Created by the FaceBook Artificial Intelligence Research Laboratory Division in 2016 for digital image processing [66], Pytorch is a library for Python-based programming which facilitates DL model development by use of multi-dimensional arrays known as *tensors*. Pytorch provides an extensive mathematical tool set for fast and efficient tensor operations which users can import using the *torch* module. Tensors act as input representations in an n-dimensional array format using floating point d-type values. Floating point numbers could be representative of the hair of a dog or the value of a pixel in an image. The tensor data structure also shares many similarities with *NumPy* arrays, allowing Pytorch to be used with other scientific Pythonic libraries. Several advantages compared to other various Python data types and competitive DL platforms include:

- Accelerated computing on a CPU (Central Processing Unit) or NVIDIA GPU (Graphics Processing Unit)
- Immediate execution vs deferred runtime execution
- Contiguous memory allocation
- Dynamic Computational Graph Engine
- Automatic differentiation and backpropogation via gradient descent

```
In[5]: x = torch.rand(5, 3) # creates a random  5x3 matrix tensor
  ...: print(x)
  ...:
tensor([[0.9524, 0.2546, 0.6627],
        [0.4493, 0.5192, 0.9349],
        [0.0263, 0.0867, 0.3968],
        [0.8808, 0.0523, 0.7701],
        [0.6007, 0.1667, 0.6004]])
```

Fig. 6.1: Randomly generated 5x3 tensor

.

Tensors use a native 32-bit floating point d-type for all real world data encoding representations, and are stored as contiguous blocks in memory. This is opposed to, for example, lists and one-dimensional vectors in python, which are boxed and stored as individual objects in memory. Basic Pythonic lists are simply indexable pointers to objects which must be retrieved and re-stored in memory for operation in training loops. When handling small data sets, this is no issue, but thousands or millions of data points could prove troublesome for consumer grade computers. On the other hand, tensors are stored in un-boxed, C numeric types, thus access to a specific tensor only requires only a "view" over its contiguous memory location for manipulation without removing, renaming and restoring the data as an object in memory [67].

Tensors are the core data structure at the heart of model development in Pytorch. Under the hood, these n-dimensional arrays allow for fast and efficient mathematical

operations and offer several advantages when dealing with large computations. From Fig. 6.2, the tensor can be viewed as an array of arbitrary number of dimensions compared to a standard 2-D matrix or vector (array of scalar values). This dimension reflects the n-indices comprising the tensor. Although an undefined number of dimensional usage with tensors is difficult to conceive, this work will primarily maintain the mathematical expressions used in tensor calculus and limit the data structure to 3 dimensions for sake of argument.

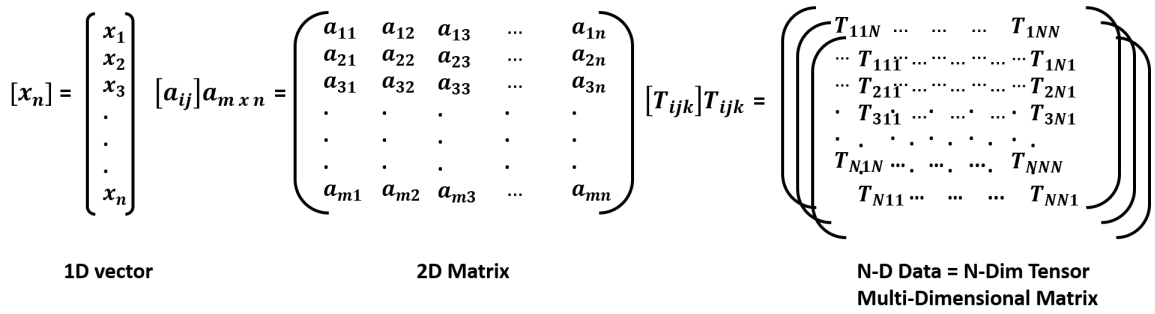

Fig. 6.2: Tensor vs. Standard Array Structure

.

When viewed from the traditional mathematical and physics perspective of tensors in a 3D vector space, a tensor of rank n is a mathematical object with n indices containing M^n components (if using M-dim space) which must obey a specific set of rules. Specifically, a tensor must remain invariant under a change of coordinate system. This is because in a 3D tensor, each component contains a pair of basis vectors shown in equation 6.1 indicating specific axes or coordinate system. Only when speaking in terms of relativity does an additional fourth dimension exist in mathematical representation of a tensor using the addition of *time* - $T_{ijkt} = [X_n, Y_n, Z_n, t_n]$. For simplicity and the main purpose behind Pytorch tensors used in scientific computing, this brief explanation is offered for some further understanding of this complex ideal.

$$T_{ij} = \begin{bmatrix} T_{xx} & T_{xy} & T_{xz} \\ T_{yx} & T_{yy} & T_{yz} \\ T_{zx} & T_{zy} & T_{zz} \end{bmatrix} \tag{6.1}$$

$$\mathbf{T} = (T_{ijk}) = (T_{NNN})$$

for any number of indexed dimensions. This arbitrary tensor, T, may also be written under dimensional transform regarding any basis vector as...

$$\mathbf{T} = (T^{k}_{ij}) \quad or \quad \mathbf{T} = (T^{jk}_{i})$$

6.1.3 The Learning Process - Backpropogation and the Gradient

One of the core aspects which Pytorch provides allows tensors to maintain a record of the mathematical operations performed on them, so that any derivative of a nodal output in the network can be calculated with respect to any of its inputs (nodal leaves) automatically using the *torch.autograd* package [67]. Other packages such as *torch.optim* and *torch.nn* give the end user expansive tools build complex neural networks and optimize various functions within a network model so that the transformed inputs begin producing outputs similar to that of the training set.

The fundamental component of any deep learning or neural network (NN) is the *neuron*, which are strung together in large quantities in formation of a learning network. For simplistic reasons, only the fundamental algebraic expression using a linear relationship is given for theoretical purposes in this work from [67]. In this example, x is the input to the single-neuron computation, w is the weight parameter, b is the bias parameter, and o is the output.

$$o = tanh(w * x + b)$$

The dynamic computation graph which provides a record of all operations performed on a specific tensor is constructed using neurons to form nodal layers of the model. Initially, the user assigns some error using mean squared error (MSE) to the parameters using a basic cost function (loss function) which evaluates accuracy between the desired and predicted values of the model. As the parameters are updated to reduce the error and reach convergence, the model is re-trained over each pass of data. The convex nature of the MSE optimization curve allows for a closer prioritization of the slightly weighted parameters closer to absolute zero compared to the absolute valued difference of squares.

$$L(y, \hat{y}) = (y_{pred} - y_{des})^2 \tag{6.2}$$

$$MSE(y, \hat{y}) = 1/n \sum_{i=0}^{n-1} (y_{pred} - y_{des})^2 \tag{6.3}$$

Given valid input data and the desired outputs with initial parameter weights, the model is fed the input data (forward pass). After the output is produced, a measure of the error is calculated by comparison of the predicted outputs with the correct outputs. Next, the derivative of the loss function with respect to the weights, or gradient, is computed using the chain rule and passing back through from output to initial input (backward pass). This process is essentially moving backwards through the nodes to calculate the reverse derivative of the output with respect to the inputs. Finally, the weights are updated based on local minima, or the direction by which the updated parameters lead to the largest decrease in error. The procedure is then repeated until the MSE reaches a specified threshold set by the user, or target condition set during

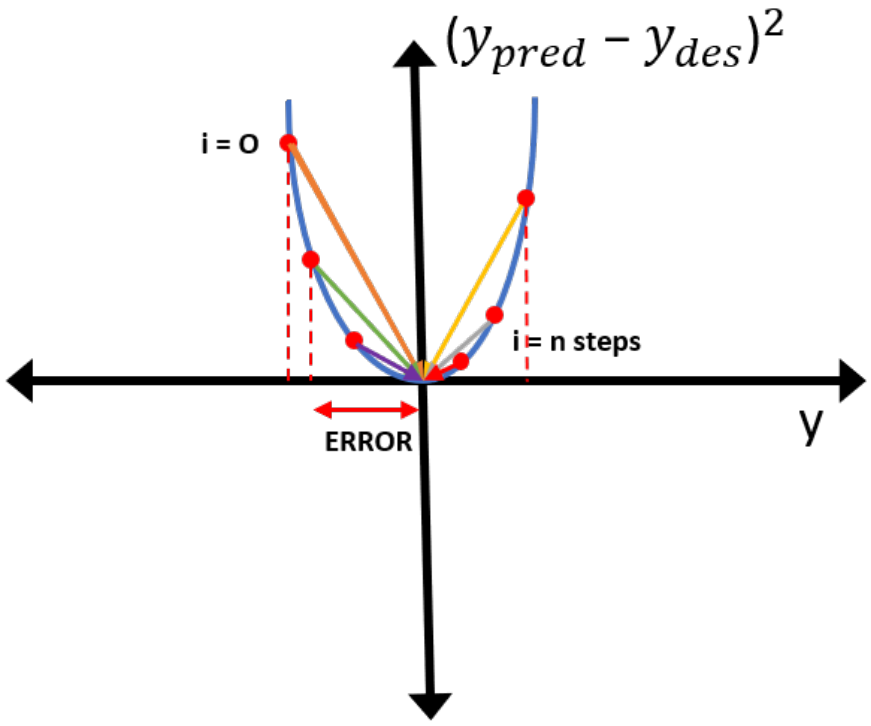

Fig. 6.3: MSE Convex Loss Function using n-Steps to Converge

.

optimization.

Basically, Pytorch is designed to create NN models for which the derivatives of the fitting error, with respect to the parameters, can be expressed analytically. The ability to calculate the gradient of a loss function with respect to various weighted parameters at any node of the network allows Pycharm to make adjustments using a specified step size to iteratively train a model [65, 67]. In reference to the mathematical definition of the gradient, this procedure of taking reverse derivatives of the loss function with respect to parameter weights can be expressed from [67] by using the function model m as $LossL(M_{w,b}(x))$ and the gradient as:

$$\nabla_{w,b} L = \left[\frac{\partial L}{\partial w}, \frac{\partial L}{\partial b}\right] = \left[\frac{\partial L}{\partial M} \cdot \frac{\partial M}{\partial w}, \frac{\partial L}{\partial M} \cdot \frac{\partial M}{\partial b}\right] \tag{6.4}$$

An example of reverse differentiation is given in the computational node graph in Fig.

6.4. If a and b are given as inputs to the model and e is the output. By traversing upward starting from the inputs, typical derivatives for the relationships between each layer and the previous nodes are determined until the output is reached. In contrast, by moving backwards from the output to the input nodes, and taking the rate of change from e with respect to a and b, the resulting reverse derivatives describe how a change in either input will directly affect the output of the model. This concept is very important because multiple input parameters require precise adjustments via the weights to improve the target output.

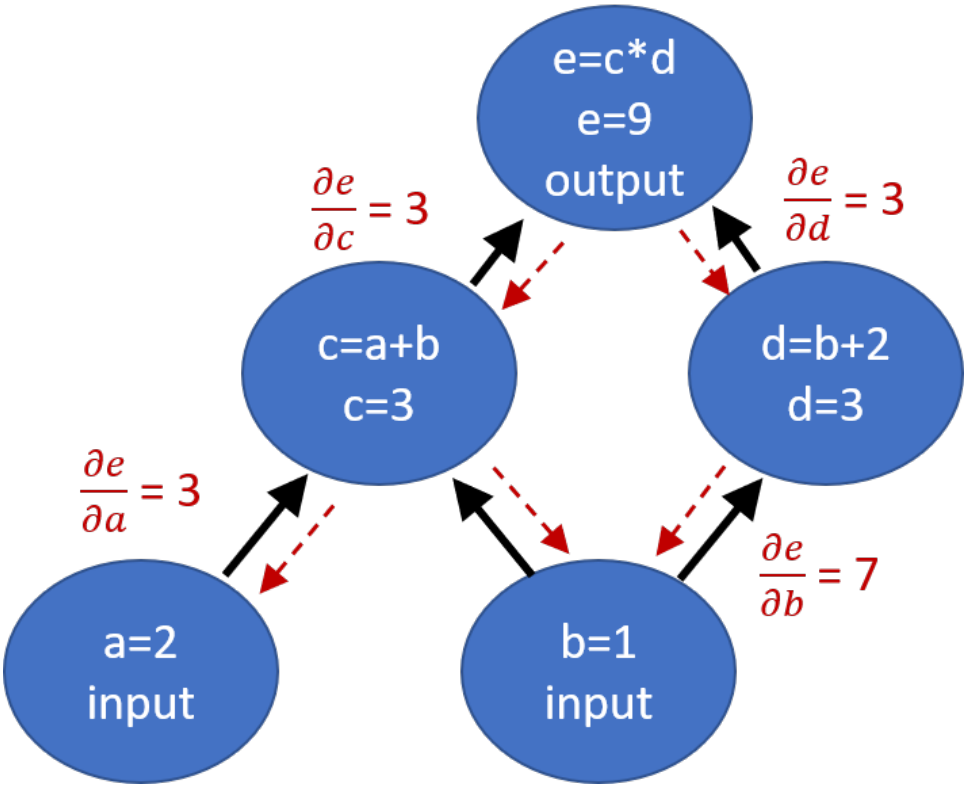

Fig. 6.4: Computational Node Graph Reverse Derivative

.

By optimizing the loss function in Pytorch during training, which does require much practice and a good understanding of the model behavior, the concept known as *gradient-descent* is used in backpropogation to update these parameters (as described). This form of optimization is highly used across various engineering disciplines to im-

prove model implementation and convergence quickly. Creating learning loops by which this training is delivered is essential in neural network development using tensors in Pytorch. Fine tuning the model by adjusting step size for weight and bias adjustment can be tricky at first, however, this concept has proven to yield high accuracy among many other implementations in which models may have thousands or even millions of adjustable parameters.

The following subsections describe possible uses for Pytorch in power systems analysis. Due to the newness and constantly changing beta software platform, very few research publications involving Pytorch in power systems studies are available. Therefore, only conceptual theory for usage is presented in this chapter, as this research will continue over the next several years.

6.1.4 Tensor-based Analytics for Traditional Power Flow Methods

Analyzing the performance of any power system both in normal operational conditions and under short-circuit (fault) conditions is vital for understanding distribution behavior with or without DER integration. Conducting a *load flow* or *power flow* in steady-state (SS) conditions determines bus voltages and angles under a given set of load conditions. Typically, this is handled internally by modern software engines, however, developing a method of solving power flow equations using tensor techniques is considered.

The first step in analyzing a power system SS response load flow is data structure conversion from the native data type into a set of organized tensors. Software such as *Pandapower v2.2.2* which operates using the native *Pandas* library data structure, the *DataFrame* (DF), contains various IEEE and CIGRE test networks for simulation and testing. Each network contains element tables for each individual element in the network (generators, load powers, line impedances, etc.). In order to correctly map this data to usable tensors while retaining order per bus, an iterative loop is constructed

to convert each DF row or column entry into a NumPy array and directly into a tensor, which can be "tagged" for identification similar to a variable. In this manner, the indices of the floating point values are maintained, along with the associated bus location or line location sorted from the slack bus out to the last.

Once all parameters have been successfully mapped to native tensors, all mathematical procedures required for power flows can be employed. The bus admittance matrix can be calculated if needed prior to the data conversion type or afterwards using similar techniques to invert individual line impedance powers. Assuming all values are converted to the per unit scale using system wide base values, the bus admittance matrix can be determined by taking the multiplicative inverse of each line impedance in the converted square matrix using the *torch.linalg* package, designed for fast element-wise linear algebraic operations. For a radial distribution feeder, this matrix will contain mainly diagonal entries as each bus is only connected to two lines (to and from).

$$\mathbf{T_{y_{ij}}} = 1/[r_{ij} + jx_{ij}]_{ijn} \tag{6.5}$$

After substitution of the power balance equations, the general form of the *Newton-Raphson* power flow equations can be determined using true phasor form. Solving the power flow equations involves finding a solution to the non-linear equations using an iterative process in which a convergence criterion is reached.

$$\Delta P_k = V_k \sum_{i=1}^{n} |Y_{ki}| V_k V_i \cos(\delta_k - \delta_i - \theta_{ki}) - P_k^{sp} \tag{6.6}$$

$$\Delta Q_k = V_k \sum_{i=1}^{n} |Y_{ki}| V_k V_i \sin(\delta_k - \delta_i - \theta_{ki}) - Q_k^{sp} \tag{6.7}$$

Ultimately, once all data has been mapped into tensors, it must remain in this format in order to accelerate all computational methods, therefore all mathematical operations must be performed using tensors after the conversion to form the admittance matrix. Additionally, computation of the admittance matrix and other properties is tedious and gives Pytorch no edge over practical software which can already perform such tasks very quickly. However, Pytorch excels in situations which call for computation of derivatives quickly and efficiently, using n-dimensional tensors which can hold any type of floating point data. Therefore, determination of the *Jacobian Matrix* could potentially allow for faster load flow approximations in large networks.

$$\mathbf{T_{ijJac}} = \begin{bmatrix} \frac{\partial P_n}{\partial \delta_n} & \cdots & \frac{\partial P_n}{\partial V_n} \\ \cdots & \cdots & \cdots \\ \frac{\partial Q_n}{\partial \delta_n} & \cdots & \frac{\partial Q_n}{\partial V_n} \end{bmatrix} \tag{6.8}$$

From equation, 6.8, the generalized tensor form of the Jacobian matrix is introduced where each of the four individual square matrix sections within the matrix relate the partial derivative relationships between active and reactive powers and respective voltage magnitudes and angles per bus. By using Pytorch's automatic differentiation tool set, *torch.autograd*, this process could see a significant speed up in runtime compiling on larger networks. In order to build the Jacobian matrix using tensors, all data in the network is initially converted to complex form during the data structure conversion process, and can be *serialized* allowing all data to be stored as complex values.

Simply, the Jacobian matrix holds all the possible partial derivatives of our two vectors of interest at a time, which provides the gradient of one function with respect to another. For example, if a tensor $\hat{\mathbf{X}} = [x_1, x_2, ...x_n]$ contains multiple inputs in a single node and tensor $\hat{\mathbf{W}} = [w_1, w_2, ...w_n]$ holds the weights of a model that upon adjustment, produces another tensor $\hat{\mathbf{Y}}$ used to calculate the loss function L from 6.2. Then the gradient of the scalar loss L with respect to vector $\mathbf{Y}$ is used in *autograd.backward*

as the gradient tensor, $\hat{\mathbf{G}}$. When multiplied by the Jacobian matrix, the relationship between the loss with respect to the inputs $\hat{\mathbf{X}}$ is achieved in 6.9.

$$\hat{\mathbf{X}}_j = \hat{\mathbf{G}}_i \mathbf{T}_{\mathbf{ijJac}} \tag{6.9}$$

$$\left[\frac{\delta_n}{|V_n|}\right]^{j+1} = \left[\frac{\delta_n}{|V_n|}\right]^{j} - \mathbf{T}_{\mathbf{ijJac}}{}^{-}1 \left[\frac{\Delta P_n}{\Delta Q_n}\right]^{j} \tag{6.10}$$

Simple usage of the *torch.autograd.grad* module allows for auto-differentiation of multiple functions which returns a list of gradients w.r.t the inputs of that function. In the case of a power flow, the weights could be initialized as very small values since the main interest is in the bus voltages relative to the power. So taking the inverse of $\mathbf{T}_{\mathbf{ijJac}}$ and multiplying by the determined powers allows for the voltages to be updated until convergence is reached after taking derivatives of equations 6.6 and 6.7. Due to immediate execution, it makes little sense to spend time gathering all partial derivatives and storing them in a matrix, when each relationship can be calculated instantly and vectorized. Thus, defining the vector-Jacobian products for each child node in the network (bus) could prove to be effective as a work-around to produce voltage magnitudes and angles during the backpropogation process.

However, other power flow methods such as *Decoupled* and *Fast Decoupled* power flow could be considered. Although standard techniques are used heavily in modern research with success, they remain computationally heavy and require tremendous computing power. In smaller networks, this is no issue for modern day machines, however, when dealing with networks with hundreds or even thousands of buses and loads in which extremely large arrays must be constructed to form this matrix for power flow calculations, Pytorch could provide a new and efficient approximation to the solution.

6.1.5 Pytorch Applications in Power Systems - IMO Improvement(s)

Optimization for multivariate equations as discussed in Chapter 4 using multiple objectives, or cost functions, can also be implemented using Pytorch. Integration of solar PV using the IMO (Chapter 4) uses a set of index relations: active power loss, reactive power loss, and voltage deviation to determine the optimal minimal solar PV sized per nodal bus location in a radial distribution feeder. Although the IMO is productive at singularly sizing a single solar array per bus, opportunity for using and expanding this algorithm proved successful.

$$IMO = \sigma_1 \frac{P_{LPV}}{P_L} + \sigma_2 \frac{Q_{LPV}}{Q_L} + \sigma_3 \frac{VD^2_{PV}}{VD^2}$$

$$\frac{\partial IMO}{\partial P_{PVK}} = \frac{\sigma_1}{P_L} \frac{\partial P_{LPV}}{\partial P_{PVK}} + \frac{\sigma_2}{Q_L} \frac{\partial Q_{LPV}}{\partial P_{PVK}} + \frac{\sigma_3}{VD^2} \frac{\partial VD^2_{PV}}{\partial P_{PVK}} = 0$$

As a reminder, the IMO is calculated using a partial derivative relationship between power loss and voltage deviation ratios (indices) with a local grid-connected PV over the base case losses recorded in the initial load flow of the network at steady state. Recall that the IMO performs well with the additional multi-objective allocation technique *Method Two* proposed to add multiple PV support on branch laterals and compensate for a poor system voltage profile using the IEEE 33-bus radial distribution system. This process is effective, yet computationally inefficient due to the excessive algorithmic looping required to run power flows at each bus location while making calculating loss with and without solar PV present. In extremely large networks with thousands of buses and laterals, the script run time could significantly increase.

The results of the IMO also yielded specific PV sizes which covered a range of active PV power outputs, assuming no reactive power injection on the inverter side (unity power factor). While the weighted factors σ_n are fixed scalars, the other terms are

simply loss functions designed to approximate the differences in power lost along the lines between nodes. The gradients of the loss functions with respect to the PV size determine the smallest solar PV capable of reducing loss and supplementing voltage at the location of power injection. The question arises as to if a larger combination of sizes could be tested simultaneously, and the power loss gradient determined immediately following the calculation?

Creating target tensors for the voltage deviation and loss functions simply consists of creating single array tensors with the desired targeted values of the variables dictated by the IMO. This same technique is used in [67] for a classification problem where the desired outputs are strings represented by a class of integers. For instance, the desired bus voltage following a power flow after injection solar PV is ideally 1.0 ± 0.05 p.u., which means that the target tensor can hold values of this constraint range depending on their amount of undervoltage present in the base case condition. Those buses with the most voltage deviation at critical load locations of power loss could ideally be set to the maximum, while other buses could be set to 1.0 for all buses except the slack bus. Similarly, the desired active and reactive power loss target tensors could simply be set to zero.

$$\hat{\mathbf{T}}_{VP_{DES}} = \begin{bmatrix} 1.0 \\ 1.0 \\ 1.0 \\ \cdots \\ \cdots \\ 1.05 \\ 1.05 \\ 1.05 \end{bmatrix} \tag{6.11}$$

$$\hat{\mathbf{T}}_{PL_{DES}} = \begin{bmatrix} 0.0 \\ 0.0 \\ 0.0 \\ \cdots \\ \cdots \\ 0.0 \\ 0.0 \\ 0.0 \end{bmatrix} \tag{6.12}$$

If after running the IMO, a pareto front of PV sizes is produced to satisfy the minmal PV values over a specific set of locations, the range of $P_{PVK_{min}}$ to $P_{PVK_{max}}$ can be used to create any specific built in Pytorch distribution of PV sizes for testing and act as input to the model. Using the loss functions, the model can be fed various PV array sizes simultaneously, and assuming an approximate load flow method is available, losses can be determined accordingly. The resulting losses and bus voltages can be stored in separate tensors and compared to using tensor boolean operations such as *torch.le* to determine if the bus voltages are hitting the target.

Using comparative tools to match resulting values with their target values allows for iterative adjustments to the respective PV sizes. Weights and bias tensors could also be included to determine the degree by which the solar PV sizes are adjusted based on the MSE difference at each bus. Recall that the load powers and line parameters needed are included in the load flow calculation. After computing the MSE, a set of weights associated with the PV sizes makes an adjustment and the simulation is run again for any given number of PV on the network until the optimal percentage of solar penetration is achieved such that losses are globally minimal and bus voltages are maximized.

Although this improvement seems minimal, the ability to use the IMO to deduce an

acceptable range of PV may prove to be more selective. However, this "brute force" method of model adjustment is not so readily available using the IMO on its own. The looping and nested looping processes required to manage a larger system would no doubt prove to be time costly compared to tensors in a neural network model which can make adjustments *automatically* to improve the desired conditions. Other potential applications in power systems analysis for tensor-based analytics includes profile development and forecasting, regression analysis, and signal decomposition, among many others.

Overall, Pytorch offers a vast library of features and tools that make model development more powerful, no matter the problem at hand. Applications in power systems and DER integration have not yet been established and accepted by the community, but there is quite a bit of potential with the emerging acceptance of AI based solutions. Although this tool is still in beta phase, results and adaptability to other sectors like power will find a benefit from such a unique computing platform. Finally, Pytorch provides extensive optimization and mathematical scientific computing packages which accelerate the computing required to deal with DER modeling using DL models for solar PV integration and power systems analysis.

CHAPTER 7

Summary of Work and Future Research Direction

In summary, the studies conducted in this work have shown the importance of PV integration analysis in distribution systems. The introduction of solar PV power injecting into the modern smart grid can have both positive and negative impacts. Key areas of focus such as power systems protection, optimization, planning, hosting capacity and forecasting analysis are all areas of study challenging the adoption of renewable energy in power networks.

The analysis and simulation results from *Chapter Three* demonstrated concerns regarding large-scale PV penetration on radial feeder protection schemes. Studies carried out on the feeder with various levels of PV penetration in combination with a single phase fault showed vulnerabilities using traditionally time-graded overcurrent digital relays. The tripping response times and sequence of both relays in various scenarios proved inconsistent with desired operation due to locally excessive PV power injections during a simultaneous fault in the network.

From a larger standpoint, this work has shown that with an increasing amount of DERs in distribution systems, traditional time-grading protection techniques are susceptible to failure in certain realistic circumstances. Especially during conditions in which the protection system should function normally (fault conditions), the abnormal behavior of the line currents caused by highly injected solar PV can cause further damage to the power system. Future research involves improving relay adaptability to better handle these conditions.

Chapter Four showed how vital solar PV optimization has become regarding correct sizing and placement in radial distribution feeders. Using proper optimization tech-

niques, a multi-objective approach to solar PV planning proved to reduce power losses and voltage deviation across the network. More importantly, several major improvements were proposed to the original IMO method which properly allocated solar PV for distribution feeders containing lateral branches. The mathematical sizing algorithm using the path of least electrical impedance accounted for each bus location correctly while maintaining excellent loss reduction and profile improvement at critical locations in the system.

Additionally, it was shown by derivation and simulation that by using the complete voltage magnitude and phase angle information in the optimization, bus voltage regulation was drastically improved over all other scenarios. This significant improvement also did not require a heavy sacrifice of power loss reduction, and provides a more accurate estimation of the resulting bus voltages with PV integration. Simulation results from both the IEEE 33-bus and *PandaPower* 6-bus network validated the usage of multiple solar PV's on radial feeders to improve network operational performance such as reducing congestion and improving stability in feeders effectively. Further research expanding on this technique to consider all models in a time-series analysis using load and solar PV profiles could more accurately depict the proper PV size and location based on local demand and time of day.

Time series analysis in *Chapter Five* uses a controller module to show voltage profile fluctuations throughout a 24-hour period based on data gathered from a solar plant and various load models. The iterative power flows conducted at each time stamp display how a system can respond based on the variable level of power absorption versus simultaneous consumption in a 15-bus CIGRE network. Plots of the system voltages after implementation showed areas of undervoltages during evening hours and erratic behavior caused by uncontrollable weather patterns. Models such as these are used extensively in forecasting and impedance matching by utilities to plan for proper PV deployment.

Finally, a discussion in *Chapter Six* is presented regarding the use of tensors for power systems analysis proposing several ideas using an alternative scientific computing based approach. A method for extracting the Jacobian Matrix to perform a load flow using multi-dimensional arrays to solve a system of non-linear equations is suggested. Tensor usage for classification and improvement over existing optimization techniques is feasible and should be more closely examined.

Future research involving solar PV integration studies is becoming more reliant on machine and deep learning models which can handle the complexities and massive sizes of data sets required in modern analysis. The ability of these models to extract unique features and relationships between input and output parameters of a system using derivatives are unquestionably important, as more and more devices are added to smart grids. It is clear that the integration of PV in distribution feeders requires analysis techniques built to handle massive data in real time, while also providing the capabilities to make mathematical decisions based on underlying relationships to benefit the grid and maintain resiliency in a growing network.

List of Abbreviations

PV	Photovoltaic
DG	Distributed Generation
PEV	Plug-In Electric Vehicle
DER	Distributed Energy Resources
p.u.	Per-unit (system)
O/C	Overcurrent
FCL	Fault Current Limiter
PCC	Point of Common Coupling
LVRT	Low Voltage Ride Through
HVRT	High Voltage Ride Through
HC	Hosting Capacity
IMO	Multi-Objective Index
MPPT	Maximum Power-Point Tracking
ML	Machine Learning
DL	Deep Learning
AI	Artificial Intelligence
NN	Neural Network
ANN	Artificial Neural Network
RNN	Recursive Neural Network
POI	Points of Interconnection
IDMT	Inverse Definite Minimum Time
CT	Current Transformer
SEL	Schweitzer Engineering Laboratory
EMTP	Electromagnetic Transient Program

PSM	Plug Setting Multiplier
TMS	Time Multiplier Settings
AVM	Average Value Model
PWM	Pulse-Width Modulation
DoE	Department of Energy
DTPS	Distribution Testbed Protection System
IBR	Inverter-based Resources
PLC	Programmable Logic Controller
MCB	Miniature Circuit Breaker
AWG	American Wire Gauge
RU	Rack Unit
SCADA	Supervisory Control and Data Acquisition
pf	Power Factor
GIS	Geographical Information System
d-type	Data Structure Type
MSE	Mean Squared Error
QSTS	Quasi-Static Time Series
SS	Steady State
DF	DataFrame
IEEE	Institute of Electrical and Electronics Engineers

List of Key Symbols

T_{op}	Time of Operation
I_{Pkp}	Pickup current relay setting
$\bar{S}$	Complex Power
$\bar{Z}$	Line impedance
$P = V * I$	Elemental Power Equation
$V = I * R$	Ohm's Law
P_L, Q_L	Active and Reactive power loss base case
VD^2	Voltage Deviation squared base case
P_{LPV}	Active Power loss with grid-connected PV
Q_{LPV}	Reactive Power loss with grid-connected PV
VD^2_{PV}	Voltage Deviation Squared with grid-connected PV
σ_N	Weighted IMO factors (normalized)
P_{PVK}	Grid-connected solar PV active power magnitude
Q_{PVK}	Grid-connected solar PV reactive power magnitude
$\bar{V}_1 - \bar{V}_2$	True voltage phasor deviation
$\lvert\bar{X}_n\rvert$	Absolute magnitude
t_{step} or ΔT	Time interval measurement
$\mathbf{T} = (T_{ijk}) = (T_{NNN})$	3D Tensor
$o = tanh(w * x + b)$	Neuron using input x, weight w, and bias b
$L(y, \hat{y})$	Convex loss function
$MSE(y, \hat{y})$	Mean Squared Error
$\nabla_{w,b} L$	Gradient of the Loss Function w.r.t. w and b
$\mathbf{T_{ijJac}}$	Jacobian Tensor Matrix
ΔP_k, ΔQ_k	Newton-Raphson Power Flow Equations

Bibliography

[1] S. Massoud Amin and B. F. Wollenberg, "Toward a smart grid: power delivery for the 21st century," *IEEE Power and Energy Magazine*, vol. 3, no. 5, pp. 34–41, 2005.

[2] F. Katiraei and J. R. Agüero, "Solar pv integration challenges," *IEEE Power and Energy Magazine*, vol. 9, no. 3, pp. 62–71, 2011.

[3] S. M. Amin, "For the good of the grid," *IEEE Power and Energy Magazine*, vol. 6, no. 6, pp. 48–59, 2008.

[4] F. Li, W. Qiao, H. Sun, H. Wan, J. Wang, Y. Xia, Z. Xu, and P. Zhang, "Smart transmission grid: Vision and framework," *IEEE transactions on Smart Grid*, vol. 1, no. 2, pp. 168–177, 2010.

[5] D. J. Feldman and R. M. Margolis, "Q4 2018/q1 2019 solar industry update," National Renewable Energy Lab.(NREL), Golden, CO (United States), Tech. Rep., 2019.

[6] X. P. Zhang, "A framework for operation and control of smart grids with distributed generation," in *2008 IEEE Power and Energy Society General Meeting - Conversion and Delivery of Electrical Energy in the 21st Century*, 2008, pp. 1–5.

[7] A. Darwish, A. Abdel-Khalik, A. Elserougi, S. Ahmed, and A. Massoud, "Fault current contribution scenarios for grid-connected voltage source inverter-based distributed generation with an lcl filter," *Electric Power Systems Research*, vol. 104, pp. 93–103, 2013.

[8] A. Cesar, K. M. Abo-Al-Ez, and M. T. Kahn, "Overcurrent directional protection with pv system integration," in *2019 International Conference on the Domestic Use of Energy (DUE)*. IEEE, 2019, pp. 2–7.

[9] A. Dhoke, R. Sharma, and T. K. Saha, "Pv module degradation analysis and impact on settings of overcurrent protection devices," *Solar Energy*, vol. 160, pp. 360–367, 2018. [Online]. Available: https://www.sciencedirect.com/science/article/pii/S0038092X1731085X

[10] S. Corsi, *Voltage control and protection in electrical power systems: from system components to wide-area control*. Springer, 2015.

[11] N. I. Nkhasi and A. K. Saha, "Protection coordination and anti-islanding control of grid-connected pv systems," in *2019 Southern African Universities Power Engineering Conference/Robotics and Mechatronics/Pattern Recognition Association of South Africa (SAUPEC/RobMech/PRASA)*. IEEE, 2019, pp. 605–610.

[12] M. Jafari, T. O. Olowu, A. I. Sarwat, and M. A. Rahman, "Study of smart grid protection challenges with high photovoltaic penetration," in *2019 North American Power Symposium (NAPS)*. IEEE, 2019, pp. 1–6.

[13] B. K. Perera, P. Ciufo, and S. Perera, "Point of common coupling (pcc) voltage control of a grid-connected solar photovoltaic (pv) system," in *IECON 2013 - 39th Annual Conference of the IEEE Industrial Electronics Society*, 2013, pp. 7475–7480.

[14] C. A. Plet, M. Graovac, T. C. Green, and R. Iravani, "Fault response of grid-connected inverter dominated networks," in *IEEE PES general meeting*. IEEE, 2010, pp. 1–8.

[15] M. C. Vargas, M. A. Mendes, and O. E. Batista, "Faults location variability in power distribution networks with high pv penetration level," in *2018 13th IEEE International Conference on Industry Applications (INDUSCON)*. IEEE, 2018, pp. 459–466.

[16] C.-Y. Tang, Y.-T. Chen, and Y.-M. Chen, "Pv power system with multi-mode operation and low-voltage ride-through capability," *IEEE Transactions on Industrial Electronics*, vol. 62, no. 12, pp. 7524–7533, 2015.

[17] Z. Tian, B. Perers, S. Furbo, and J. Fan, "Thermo-economic optimization of a hybrid solar district heating plant with flat plate collectors and parabolic trough collectors in series," *Energy Conversion and Management*, vol. 165, pp. 92–101, 2018.

[18] N. Aste, C. Del Pero, and F. Leonforte, "Optimization of solar thermal fraction in pvt systems," *Energy Procedia*, vol. 30, pp. 8–18, 2012.

[19] F. Ascione, N. Bianco, R. F. De Masi, C. De Stasio, G. M. Mauro, and G. P.

Vanoli, "Multi-objective optimization of the renewable energy mix for a building," *Applied Thermal Engineering*, vol. 101, pp. 612–621, 2016.

[20] R. Bornatico, M. Pfeiffer, A. Witzig, and L. Guzzella, "Optimal sizing of a solar thermal building installation using particle swarm optimization," *Energy*, vol. 41, no. 1, pp. 31–37, 2012.

[21] Z.-D. Cheng, Y.-L. He, B.-C. Du, K. Wang, and Q. Liang, "Geometric optimization on optical performance of parabolic trough solar collector systems using particle swarm optimization algorithm," *Applied energy*, vol. 148, pp. 282–293, 2015.

[22] A. El-Zonkoly, "Optimal placement of multi-distributed generation units including different load models using particle swarm optimisation," *IET generation, transmission & distribution*, vol. 5, no. 7, pp. 760–771, 2011.

[23] T. Khatib, A. Mohamed, and K. Sopian, "A review of photovoltaic systems size optimization techniques," *Renewable and Sustainable Energy Reviews*, vol. 22, pp. 454–465, 2013. [Online]. Available: https://www.sciencedirect.com/science/article/pii/S1364032113001251

[24] F. Ding and B. Mather, "On distributed pv hosting capacity estimation, sensitivity study, and improvement," *IEEE Transactions on Sustainable Energy*, vol. 8, no. 3, pp. 1010–1020, 2016.

[25] W. Niederhuemer and R. Schwalbe, "Increasing pv hosting capacity in lv grids with a probabilistic planning approach," in *2015 International Symposium on Smart Electric Distribution Systems and Technologies (EDST)*. IEEE, 2015, pp. 537–540.

[26] S. Wang, S. Chen, L. Ge, and L. Wu, "Distributed generation hosting capacity evaluation for distribution systems considering the robust optimal operation of oltc and svc," *IEEE Transactions on Sustainable Energy*, vol. 7, no. 3, pp. 1111–1123, 2016.

[27] B. B. Navarro and M. M. Navarro, "A comprehensive solar pv hosting capacity in mv and lv radial distribution networks," in *2017 IEEE PES Innovative Smart Grid Technologies Conference Europe (ISGT-Europe)*. IEEE, 2017, pp. 1–6.

[28] Y. Wang, J. Cheng, F. Fan, Z. Chen, Z. Xiao, and K. Deng, "Maximum pv access

capacity planning method for rural power grid considering overload risk," in *2019 IEEE 3rd Conference on Energy Internet and Energy System Integration (EI2)*. IEEE, 2019, pp. 387–391.

[29] S. Jothibasu, S. Santoso, and A. Dubey, "Optimization methods for evaluating pv hosting capacity of distribution circuits," in *2019 IEEE 46th Photovoltaic Specialists Conference (PVSC)*. IEEE, 2019, pp. 0887–0891.

[30] D. Q. Hung, N. Mithulananthan, and K. Y. Lee, "Determining pv penetration for distribution systems with time-varying load models," *IEEE Transactions on Power Systems*, vol. 29, no. 6, pp. 3048–3057, 2014.

[31] D. Singh, D. Singh, and K. Verma, "Multiobjective optimization for dg planning with load models," *IEEE transactions on power systems*, vol. 24, no. 1, pp. 427–436, 2009.

[32] M. Zarghami, B. Kaviani, F. Tavatli, and M. Vaziri, "Complex power optimization of photovoltaic systems," in *2014 IEEE PES General Meeting| Conference & Exposition*. IEEE, 2014, pp. 1–5.

[33] Q.-C. Zhong and T. Hornik, *Control of power inverters in renewable energy and smart grid integration*. John Wiley & Sons, 2012, vol. 97.

[34] C. Ma, F. Luo, W. Wei, M. Tong, G. Sun, and Y. Wang, "Preliminary study on reactive power optimization of local high-voltage distribution network with large-scale pv integration," in *IEEE PES Innovative Smart Grid Technologies*. IEEE, 2012, pp. 1–4.

[35] S. Rinaldi, M. Pasetti, P. Ferrari, G. Massa, and D. Della Giustina, "Experimental characterization of communication infrastructure for virtual power plant monitoring," in *2016 IEEE International Workshop on Applied Measurements for Power Systems (AMPS)*. IEEE, 2016, pp. 1–6.

[36] T. Hong, C. Chen, J. Huang, N. Lu, L. Xie, and H. Zareipour, "Guest editorial big data analytics for grid modernization," *IEEE Transactions on Smart Grid*, vol. 7, no. 5, pp. 2395–2396, 2016.

[37] S. M. Miraftabzadeh, F. Foiadelli, M. Longo, and M. Pasetti, "A survey of machine learning applications for power system analytics," in *2019 IEEE International Conference on Environment and Electrical Engineering and 2019 IEEE Industrial*

and Commercial Power Systems Europe (EEEIC/I&CPS Europe). IEEE, 2019, pp. 1–5.

[38] J. Xie, I. Alvarez-Fernandez, and W. Sun, "A review of machine learning applications in power system resilience," in *2020 IEEE Power & Energy Society General Meeting (PESGM)*. IEEE, 2020, pp. 1–5.

[39] R. Eskandarpour and A. Khodaei, "Leveraging accuracy-uncertainty tradeoff in svm to achieve highly accurate outage predictions," *IEEE Transactions on Power Systems*, vol. 33, no. 1, pp. 1139–1141, 2017.

[40] P.-N. Tan, M. Steinbach, and V. Kumar, "Data mining introduction," 2006.

[41] R. A. Sowah, N. A. Dzabeng, A. R. Ofoli, A. Acakpovi, K. M. Koumadi, J. Ocrah, and D. Martin, "Design of power distribution network fault data collector for fault detection, location and classification using machine learning," in *2018 IEEE 7th International Conference on Adaptive Science Technology (ICAST)*, 2018, pp. 1–8.

[42] K. Mahmoud and M. Abdel-Nasser, "Fast yet accurate energy-loss-assessment approach for analyzing/sizing pv in distribution systems using machine learning," *IEEE Transactions on Sustainable Energy*, vol. 10, no. 3, pp. 1025–1033, 2018.

[43] M. Abdel-Nasser and K. Mahmoud, "Accurate photovoltaic power forecasting models using deep lstm-rnn," *Neural Computing and Applications*, vol. 31, no. 7, pp. 2727–2740, 2019.

[44] F. Schäfer, J.-H. Menke, and M. Braun, "Contingency analysis of power systems with artificial neural networks," in *2018 IEEE International Conference on Communications, Control, and Computing Technologies for Smart Grids (SmartGridComm)*. IEEE, 2018, pp. 1–6.

[45] R. S. Salgado and A. F. Zeitune, "A direct method based on tensor calculation to determine maximum loadability power flow solutions," *Electric power systems research*, vol. 103, pp. 114–121, 2013.

[46] A. Garcés, J. J. Mora, and M.-A. Useche, "Putting tensors back in power systems analysis," in *2019 International Conference on Smart Energy Systems and Technologies (SEST)*. IEEE, 2019, pp. 1–5.

[47] Y. Chen, Y. Tan, and D. Deka, "Is machine learning in power systems vulnerable?" in *2018 IEEE International Conference on Communications, Control, and Computing Technologies for Smart Grids (SmartGridComm)*. IEEE, 2018, pp. 1–6.

[48] N. Papernot, P. McDaniel, A. Swami, and R. Harang, "Crafting adversarial input sequences for recurrent neural networks," in *MILCOM 2016-2016 IEEE Military Communications Conference*. IEEE, 2016, pp. 49–54.

[49] R. A. Walling, "Application of direct transfer trip for prevention of DG islanding," in *2011 IEEE Power and Energy Society General Meeting*, July 2011, pp. 1–3.

[50] V. Telukunta, J. Pradhan, A. Agrawal, M. Singh, and S. G. Srivani, "Protection challenges under bulk penetration of renewable energy resources in power systems: A review," *CSEE Journal of Power and Energy Systems*, vol. 3, no. 4, pp. 365–379, 2017.

[51] P. S. E. Group. (Technical Report, 2016) Direct transfer trip requirements for large inverter DER interconnecting to the LIPA distribution system.

[52] M. Meskin, P. Iyer, and A. Domijan, "Impact of pv sources on the overcurrent relays in medium voltage distribution networks," in *2017 Ninth Annual IEEE Green Technologies Conference (GreenTech)*. IEEE, 2017, pp. 271–275.

[53] A. Ghoor and S. Chowdhury, "Design of adaptive overcurrent protection scheme for a grid-integrated solar pv microgrid," in *2020 IEEE PES/IAS PowerAfrica*. IEEE, 2020, pp. 1–5.

[54] N. Rajagopal and K. V. Prasad, "Process framework for smart grid implementation," in *2013 IEEE Innovative Smart Grid Technologies-Asia (ISGT Asia)*, 2013, pp. 1–5.

[55] M. Jamil and A. S. Anees, "Optimal sizing and location of spv (solar photovoltaic) based mldg (multiple location distributed generator) in distribution system for loss reduction, voltage profile improvement with economical benefits," *Energy*, vol. 103, pp. 231–239, 2016.

[56] B. Huang, J. Hu, B. Hong, H. Yan, and K. Feng, "Macro-level evaluation of distribution network operational risks caused by distributed generation," in *2019*

IEEE Innovative Smart Grid Technologies - Asia (ISGT Asia), 2019, pp. 1576–1579.

[57] P. K. Kaushal and M. Tomar, "Real and reactive power loss minimization of ieee-33 bus by optimal dg placement using lso in rds," in *2017 International Conference on Energy, Communication, Data Analytics and Soft Computing (ICECDS)*. IEEE, 2017, pp. 1841–1844.

[58] O. Elgerd, P. Van der Puije, and P. van der Puije, *Electric Power Engineering*. Springer US, 1997. [Online]. Available: https://books.google.com/books?id=tcgvWjB1LVkC

[59] L. Thurner, A. Scheidler, F. Schäfer, J.-H. Menke, J. Dollichon, F. Meier, S. Meinecke, and M. Braun, "pandapower—an open-source python tool for convenient modeling, analysis, and optimization of electric power systems," *IEEE Transactions on Power Systems*, vol. 33, no. 6, pp. 6510–6521, 2018.

[60] K. Seepromting, R. Chatthaworn, P. Khunkitti, A. Kruesubthaworn, A. Siritaratiwat, and C. Surawanitkun, "Optimal grid-connected with multi-solar pv placement and sizing for power loss reduction and voltage profile improvement," in *2018 18th International Symposium on Communications and Information Technologies (ISCIT)*. IEEE, 2018, pp. 479–483.

[61] S. Kahrobaee and V. Mehr, "Probabilistic analysis of pv curtailment impact on distribution circuit hosting capacity," in *2020 47th IEEE Photovoltaic Specialists Conference (PVSC)*. IEEE, 2020, pp. 2210–2213.

[62] X. Buqiong and L. Yan, "Study on the impact of pv connection to grid on power flow based on time series output characteristics," in *2018 37th Chinese Control Conference (CCC)*, 2018, pp. 8991–8993.

[63] "Solar power data for integration studies." [Online]. Available: https://www.nrel.gov/grid/solar-power-data.html

[64] A. Hoballah, "Power system dynamic behavior with large scale solar energy integration," in *2015 4th International Conference on Electric Power and Energy Conversion Systems (EPECS)*. IEEE, 2015, pp. 1–6.

[65] P. Mishra, "Pytorch recipes."

[66] A. Paszke, S. Gross, F. Massa, A. Lerer, J. Bradbury, G. Chanan, T. Killeen, Z. Lin, N. Gimelshein, L. Antiga, A. Desmaison, A. Kopf, E. Yang, Z. DeVito, M. Raison, A. Tejani, S. Chilamkurthy, B. Steiner, L. Fang, J. Bai, and S. Chintala, "Pytorch: An imperative style, high-performance deep learning library," in *Advances in Neural Information Processing Systems 32*, H. Wallach, H. Larochelle, A. Beygelzimer, F. d'Alché-Buc, E. Fox, and R. Garnett, Eds. Curran Associates, Inc., 2019, pp. 8024–8035. [Online]. Available: http://papers.neurips.cc/paper/9015-pytorch-an-imperative-style-high-performance-deep-learning-library.pdf

[67] E. Stevens, L. Antiga, and T. Viehmann, *Deep learning with PyTorch.* Manning Publications Company, 2020.